Fall 2016

Development and evaluation of a coaxial cable sensing system for CO_2 sequestration wellbore integrity monitoring

Yurong Li

Department: Geosciences and Geological and Petroleum Engineering

Recommended Citation

Li, Yurong, "Development and evaluation of a coaxial cable sensing system for CO_2 sequestration wellbore integrity monitoring" (2016). *Doctoral Dissertations*. 2540.
https://scholarsmine.mst.edu/doctoral_dissertations/2540

DEVELOPMENT AND EVALUATION OF A COAXIAL CABLE SENSING SYSTEM FOR CO2 SEQUESTRATION WELLBORE INTEGRITY MONITORING

by

YURONG LI

A DISSERTATION

Presented to the Faculty of the Graduate School of the

MISSOURI UNIVERSITY OF SCIENCE AND TECHNOLOGY

In Partial Fulfillment of the Requirements for the Degree

DOCTOR OF PHILOSOPHY

in

PETROLEUM ENGINEERING

2016

Approved by:

Runar Nygaard, Advisor

Baojun Bai

Hai Xiao

Peyman Heidari

Shari Dunn-Norman

PUBLICATION DISSERTATION OPTION

This dissertation is composed of three parts. Part one (Section 1 to Section 3) gives the dissertation outline, problem statement, literature review, and research objectives. Part two (Paper I to Paper III) includes the three published or to-be-published journal papers as the main achievements of the research. Part three (Section 4 and Section 5) summarizes the major conclusions and includes the recommendations for future work.

The first paper "Laboratory Evaluation of Distributed Coaxial Cable Temperature Sensor for Application in CO_2 Sequestration Well Characterization" from page 15 to 36, has been published in the *Greenhouse Gases: Science and Technology*. The second paper "Development and Evaluation of the Coaxial Cable Casing Imager-A Cost-Effective Solution to Real-Time Downhole Monitoring for CO_2 Sequestration Wellbore Integrity" from page 37 to 66, has been submitted to the *Greenhouse Gases: Science and Engineering* and is under review. The third paper "Feasibility of Real-Time Evaluation of the CO_2 Sequestration Wellbore Integrity with the Coaxial Cable Casing Imager" from page 67 to 95, will be submitted to a journal for publication.

ABSTRACT

Downhole monitoring plays a crucial part in geological carbon dioxide (CO_2) sequestration. Various downhole monitoring technologies have been explored and applied, but they are either expensive or have system longevity issues. To address this issue, a robust and cost-effective downhole sensing system based on distributed coaxial cable sensors is developed and evaluated in laboratory, and a numerical simulation with staged finite element model is conducted to study the feasibility of using the coaxial cable sensing system for monitoring and evaluation of wellbore stability during CO_2 injection.

The real-time distributed sensing system is composed of Fabry-Perot interferometer based coaxial cable temperature and strain sensors. A high pressure high temperature (HPHT) sensor testing system is developed to study the temperature sensor accuracy, sensitivity, stability, hysteresis, and crosstalk effect under simulated downhole conditions. A lab-scale prototype of the casing imager based on strain sensors is developed and tested in laboratory to prove its real-time monitoring ability in casing axial compression, radial expansion, bending, and ovalization. A parametric study with staged finite element analysis is conducted to study the feasibility of using the casing imager in wellbore stability monitoring and evaluation during CO_2 injection in the Weyburn field.

The system is proved to perform under 1,000 psia and 110 °C, with real-time monitoring ability in casing axial compression, radial expansion, bending, and ovalization. And the parametric study with finite element model not only proved the feasibility of using the system for wellbore stability monitoring and evaluation during CO_2 injection in the Weyburn field, but also provided insight into the best cementing practice and injection conditions as guidance to avoid leakage risks in a geologic CO_2 sequestration project.

ACKNOWLEDGEMENTS

"Two roads diverged in the yellow woods, and sorry I could not travel both."

–Robert Frost

The road I chose led me to meet all the amazing people, who have been my friends, my mentor, and a forever treasure in my life.

I would have never imagined I could be so lucky to have Dr. Nygaard as my advisor. His constant encouragement drives me to challenge myself when I am faced with an obstacle, and the freedom he gives me on research lets me to explore my interests and live up to my potential. I cannot express how grateful I am for all he has done to encourage me to make it so far. And I would like to thank my committee members, Dr. Baojun Bai, Dr. Hai Xiao, Dr. Peyman Heidari, and Dr. Shari Dunn-Norman for their valuable feedback.

John Tyler and Jeffrey Heniff, the research engineering technicians at the Rock Mechanics and Explosives Research Center, have devoted a lot of time to help on the experimental setup. And the friendship of the research group members has been a constant source of moral support.

My wonderful parents, Jiwen Li and Zongzhen Wang, have cocooned me with their unconditional love as I grew up as the only child in the family. They are always there when I needed them, and I will never do enough to repay the love I received from them.

I appreciate the financial support from the Department of Energy under Award Number DE-FE0009843 and DE-FE0009284.

Finally, I want to thank myself for choosing this journey, for choosing the road less travelled by. The journey has just begun, and I hope I will always have the same courage and confidence on the road lying ahead.

TABLE OF CONTENTS

Page

SECTION

PAPER

SECTION

LIST OF ILLUSTRATIONS

Page

PAPER I

PAPER II

PAPER III

LIST OF TABLES

Page

PAPER I

PAPER II

PAPER III

NOMENCLATURE

Symbol	Description
ANOVA	Analysis of Variance
CCFPI	Coaxial Cable Febry-Perot Interferometer
CCS	Coaxial Cable Sensor
CO_2	Carbon Dioxide
DAS	Distributed Acoustic Sensing
DSS	Distributed Strain Sensing
DTS	Distributed Temperature Sensing
DV	Deterministic Value
EM	Electro Magnetic
HPHT	High Pressure High Temperature
LVDT	Linear Variable Deformation Transformer
OFS	Optical Fiber Sensor
RF	Radio Frequency
RST	Reservoir Saturation Tool
RTCM	Real-Time Compaction Monitoring
RV	Random Value
SG	Strain Gauge
VNA	Vector Network Analyzer

1. INTRODUCTION

A program for monitoring of CO_2 distribution is required once injection begins in order to manage the injection process, delineate and identify leakage risk or actual leakage that may endanger underground source of drinking water, verify and provide input into reservoir models, and provide early warnings of failure. Monitoring of the wells, deep subsurface, shallow subsurface and ground surface is expected to continue for long periods after the injection is terminated for safety and to confirm predictions of storage behavior (US EPA, 2008).

1.1. IMPACT OF CO2 LEAKAGE

Leakage is one of the major concerns on geological carbon sequestration in addition to gravity override and possible viscous fingering due to the density difference between CO_2 and resident formation water (Nordbotten et al., 2004). The benefits of sequestration would be negated if leakage occurs. Adverse health, safety, and environmental consequences may be caused by accumulated high concentration CO_2 if it is leaked into a contained environment. Plant stress and biomass changes are the possible consequences of CO_2 leakage on near-surface ecosystems (Bacon, 2013; Harvey et al., 2012; Pearce & West, 2007; Smith et al., 2013). The safety of drinking water would also be taken into account in the case of injecting fluid into subsurface. Chemical detection of leakage into shallow aquifers from a deep CO_2 geo-sequestration site will be an integral part of a safe carbon capture and sequestration (CCS) system. CO_2 that infiltrates an unconfined freshwater aquifer under oxidizing conditions and atmospheric pressure will have an immediate impact on water chemistry by lowering pH and increasing the concentration of total dissolved solids (Little et al., 2010).

1.2. CO2 LEAKAGE PATHWAYS

The main leakage risk of CO_2 through a thick, low permeable cap rock is identified to be along existing wells or through faults and fractures (Nygaard et al., 2013). Injection takes place in sedimentary basins that often have a history of oil and gas exploration and production, which means that wells other than those used for waste disposal may exist in the vicinity of the injection site. These existing wells provide possible pathways for leakage of waste fluids toward the shallow subsurface and the land surface (Nordbotten et al., 2004). The cement sheath is one of the primary barriers to prevent wellbore leakage and failure. The integrity of the cement sheath begins at the cementing operation and what happens there can greatly affect the long term integrity of the well (Nygaard et al., 2014). Thus, it is of great importance to monitor the downhole activities during the cementing and CO_2 injection process to provide early warnings of leakage risk.

1.3. MONITORING SYSTEM ACCURACY AND ROBUSTNESS

To ensure the public safety as well as obtaining carbon credits in a future cap and trade system, monitoring and modeling of sequestration projects have to reach a high degree of accuracy. The objective is to reach 99% accuracy in a monitoring and verification program (NETL, 2009). However, the predictions based on current methodology are far too uncertain to achieve the goal to account for 99% of the injected CO_2 (NETL, 2012).

Among the various monitoring approaches, in situ downhole monitoring of state parameters (e.g., pressure, temperature, etc.) provides critical and direct data points that can be used to validate the models, optimize the injection scheme, detect leakage and track the CO_2 plume (Benson et al., 2004; European Commission, 2013; Freifeld, 2009;

US EPA, 2008). However, the downhole sensors that can withstand the harsh conditions and operate over decades of the project lifecycle remain unavailable.

1.4. MONITORING SYSTEM COST

Cost is one of the primary concerns when considering if a certain monitoring technique will be adopted in a CO_2 sequestration project. The average cost of monitoring is about 0.1-0.3 USD/tCO_2 in 2002, while the overall storage cost ranged from 0.5 to 8.0 USD/tCO_2 (Rubin et al., 2015). A monitoring unit costs analysis provided by the EPA in 2008 showed that the significant components of potential monitoring costs include the drilling of monitoring wells above and into the injection zone, implementation of the subsurface and surface monitoring, and periodic seismic surveys and reservoir modeling.

Although 4D seismic has been proved successful at the Sleipner project and therefore has emerged as the standard for comparison, this technology requires high cost for implementation. A monitoring cost estimate of the Wabamun Area Sequestration Project (WASP) showed that 4D seismic to be the most expensive monitoring methods when well cost was not included (Nygaard & Lavoie, 2009). And a monitoring cost comparison for different scenarios indicates that seismic survey shares the highest ratio of cost in all stages of operation in enhanced oil recovery and storage in saline formation (Benson et al., 2004).

1.5. RISE OF DISTRIBUTED COAXIAL CABLE SENSORS

The concept of coaxial cable sensors has been put forward as early as 2011 (Huang et al., 2012, 2013; Wei et al., 2011). The concept is based on the Fabry-Perot interferometer theory, which has been successfully used in fiber optic sensors. However, in comparison with optical fibers, coaxial cables are much more robust and easy to be deployed due to its cylindrical sandwich structure. And unlike an optical fiber that has to use high quality fused silica glass, the coaxial cable operating principle allows flexible choices of materials including ceramic, silica and other high temperature tolerant dielectrics for sensor construction. The size of coaxial cables can also be varied without significant influences on signal transmissions. In addition, coaxial cables operate in radio frequency (RF) domain where the matured RF measurement technologies readily provide ample off-the-shelf components and instruments for low-cost sensor interrogation and multiplexing.

1.6. SUMMARY

Given that the widespread of carbon capture and storage will be the necessity and reality in the future, and there are significant challenges and technological gaps in current monitoring technologies, an intelligent well monitoring system based on distributed coaxial cable Fabry-Perot interferometer (CCFPI) temperature/strain sensors will be an ideal solution to a robust and cost-effective monitoring system in geologic CO_2 sequestration.

2. LITERATURE REVIEW

The literature under review include the current monitoring technologies that have been used in the monitoring program in geological CO_2 sequestration, which can be grouped into conventional well-based monitoring technologies and intelligent well monitoring technologies. The goal is to find the gap in current monitoring technologies and to get an insight on a feasible intelligent well monitoring system.

2.1. CONVENTIONAL WELL-BASED MONITORING

Recent CO_2 sequestration pilot projects have implemented novel approaches to well-based subsurface monitoring aimed at increasing the amount and quality of information available from boreholes (Freifeld et al., 2009). Well based-monitoring of oil and gas reservoirs includes a broad array of techniques, using a diverse suite of instruments. During drilling, core is often recovered to permit petro-physical measurements and provide fluid saturation information. Core plugs from the larger core are often extracted to measure permeability and porosity and segments of core can be used to conduct core fluid studies. Wireline logs provide information using non-contact methods (e.g. neutrons, seismic and electrical waves) to periodically interrogate the formation. In addition, permanently deployed sensors and repeated geophysical surveys can assess changes in the subsurface.

2.1.1. Wireline Logging. Wireline logging includes a wide variety of measurement techniques in which a sonde is trolled through a wellbore and data is transmitted from sensors to surface for recording. Commonly used wireline logs include gamma ray density, formation resistivity, acoustic velocity, self-potential, temperature and pressure. New and more sophisticated tools including formation microimagers, neutron cross-section capture, and nuclear magnetic resonance scanners have been developed by the oilfield service providers. Besides, there are wireline tools to collect fluid samples (e.g. the Kuster flow through sampler) and retrieve sidewall cores for later analysis (Freifeld et al., 2009).

The Schlumberger wireline reservoir saturation tool (RST) was used in the Frio Brine Pilot Test conducted in 2004 (Hovorka et al., 2006). The brine saturation as brine was displaced by CO_2 was measured within and immediately outside the wellbore at fine vertical resolution. However, considering the open borehole along the perforated zone, the well-based measurement in predicting CO_2 saturation in deeper formation is not representative.

2.1.2. Geophysical Technique. Near field geophysical technique requires only a single borehole and can be performed at any depth range, and sense the properties of the borehole itself and its immediate vicinity. These is a wide variety of techniques with regard to geophysical monitoring, e.g., borehole televiewer (optical), caliper logs, resistivity logs, electromagnetic induction logs, Gamma logs (passive and active), Neutron logs, sonic logs etc. These techniques can determine the near-borehole structures with a high accuracy.

However, there are several drawbacks of geophysical survey including the high cost. Depending on the relative position of the observation well, the resolution of the microseismic results might be a few meters, which is not sufficient to answer detailed questions regarding points of fracture initiation from the wellbore (Holley et al., 2010). Also, the limitation of using seismic surveys to monitor CO_2 saturation has been identified (Cairns et al., 2010). The smallest detectable amount of CO_2 depends on the fluid distribution. If homogeneously distributed, 1% CO_2 is detectable; however, if patchily distributed, anything below 18% CO_2 is indistinguishable from brine.

2.1.3. Geochemical Sampling. Geochemical sampling is used to assess rock-water interaction in order to better understand the ultimate fate of emplaced CO_2 and assess the integrity of reservoir seals. Abundant amount of methods have been devised to obtain representative downhole samples while maintaining reservoir pressure conditions. Downhole fluid samples can be collected for surface analysis using wireline formation testers (e.g. the Schlumberger Modular Formation Dynamics Tester) and U-Tubes technology which is developed for the DOE Frio Brine project (US EPA, 2008).

However, geochemical sampling requires time-consuming field sample collection work, which loses the time effectiveness of the collected data, and usually high sampling frequencies is required to collect data for a reasonable interpretation and understanding of background processed, which means additional workload. To determine the groundwater contamination risk, a density of about 50-500 wells per km^2 are required for contaminant plume mapping and remediation (Martens et al., 2012; May & Waldmann, 2014; Zimmer et al., 2011).

2.1.4. Integrated Well-Based Monitoring. In integrated well-based monitoring, each tool is sequentially deployed in the wellbore for one purpose, and is later retrieved so that a second activity or operation could be conducted. While the risks are often low for carrying out each data collection effort since they rely on off-the-shelf products, there is considerable cost in each mobilization into and out of a well. Furthermore, data is “lost” as each tool is removed to permit access for the next tool. Several CO_2 demonstration projects have taken an integrated monitoring approach, where several measurements cutting across different disciplines are conducted simultaneously using one completion. Three programs that have taken this integrated approach are the Frio Brine Pilot and CO2SINK project, both conducted in a saline reservoir, and the Otway project, consisting of an injection in a depleted gas reservoir (Freifeld, 2009).

2.2. INTELLIGENT WELL MONITORING

Intelligent well technology has built up several years' experience in the oil and gas field and is gaining more and more attention. The permanent well monitoring system can be divided into deep reservoir monitoring and near wellbore monitoring (Da Silva et al., 2012). The physical quantities measured for near wellbore monitoring include pressure, temperature, flow, acceleration (seismic and acoustic), and strain. Due to the daily matured technology, distributed sensing ability, and successful field application demonstrations, optical fiber sensors (OFS) are more and more often included in the downhole monitoring program during production and hydraulic fracturing process. The following section will focus on the currently available fiber optic sensing technologies.

2.2.1. Fiber Optic Sensing Overview. OFS are able to perform efficient monitoring with their multiplexing ability and reduced size compared with conventional wire-connected downhole sensors. Fiber optic based downhole temperature, pressure, strain, and acoustic sensors for petroleum industry application are currently available (Costello et al., 2012; Koelman et al., 2011; Medina et al., 2012; Molenaar et al., 2012; Tardy et al., 2011). One configuration of fiber optic downhole monitoring is based on multiplexing discrete sensors such as high temperature fiber Bragg gratings and Fabry-Perot interferometers (Pan et al., 2010; Schmidt-Hattenberger et al., 2004). These microsensors passively and linearly transduce the temperature/pressure to optical signals that are transmitted to the interrogation instrumentation on the surface at a speed of light (Lee, 2003). The other popular configuration of fiber optic downhole monitoring is using time-domain technique to realize truly distributed sensing. Continuous temperature profile along the entire length of an optical fiber can be mapped with decent accuracy by several mechanisms including Rayleigh scattering, Raman scattering and Brillouin scattering (Molennar et al., 2012; Tardy et al., 2012; Williams et al., 2000).

2.2.2. Distributed Temperature Sensing (DTS). The application of DTS includes monitoring in SAGD wells, hydraulic fracturing treatments, pipeline leak detection, production optimization in horizontal wells, and ESP pump integrity (Ahmed et al., 2014; Al-Gamber et al., 2013; Carlsen et al., 2013; Kaura & Sierra, 2008; Medina et al., 2012; Molenaar et al., 2012; Thodi et al., 2014). Typical installations of the DTS system include single end straight fiber, single end with downhole temperature gauge, partially returned fiber, and double end fiber (James & Alex, 2003). A known reference temperature bath or oven is required in the surface instrumentation box for temperature offset correction, and a downhole temperature gauge is needed for instrument drift calibration.

A fiber optic DTS system has been deployed in an onshore U.S. Gulf Coast CO_2 injection site from 2009 through 2012 to monitor CO_2 flow within injection zones at the inter-well scale, as well as to detect CO_2 leakage into the overburden (Nuñez-Lopez et al., 2014). The sample rate ranges from 2 to 15 minutes and more than 4 hundred million temperature measurements are recorded. The system is installed at a depth of more than 3,000 meters in two monitoring wells in close vicinity of the injection well, and two downhole gauges are installed at the cap rock and injection interval for comparison with the DTS data. The sensor resolution is claimed to be 0.0045 °F—0.00247 °F for depth shallower than 915 m. However, severe instrument drift was observed after three months since the system installation. The maximum difference between downhole gauge and DTS measured temperature is up to 15 °C. And the temperature front reached the well about three weeks later after the CO_2 plume actually arrived at the well. No reasonable explanation is found.

2.2.3. Distributed Strain Sensing (DSS). Fiber-optic Bragg-grating strain sensors have been used by Shell and Baker Hughes to monitor deformations of well tubulars and casings since 2005, which have recently been extended to monitor sand screens—the SureView real-time compaction monitoring (RTCM) system (Baker Hughes Inc., 2010a&b; Pearce et al., 2009, 2010; Rambow et al., 2010). Optical fibers with distributed strain sensors are contained in a stainless steel tube, which is then imbedded into the pre-cut helical groove on the outer casing. Laboratory scale experiments have demonstrated the system's ability to monitor casing axial strain, buckling, bending, ovalization, and a mixture of the deformation modes. The SureView RTCM system has been deployed successfully in Shell's Pinedale operations in Wyoming during 2008 on 7-in casing.

2.2.4. Distributed Acoustic Sensing (DAS). DAS relies on sensing of vibro-acoustic disturbances in the vicinity of the fiber optic cable, because the interference of back-reflected laser light is affected by acoustic disturbances along the optical fiber (Molenaar et al., 2011). The spatial resolution is usually between 1-10 m. Several DAS & DTS deployments have been carried out in Shell Canada's tight sand and shale gas fields for rea-time monitoring of hydraulic fracturing operations. The DTS measured temperature warm-back is often compared to the DAS data for comparison to determine the fracture location and qualitatively determine the fracture volume (Holley et al., 2014).

2.2.5. Limitations. Compared to conventional electronic transducers, fiber optic sensors have some inherent drawback that need to be addressed in field application (Williams et al., 2000). Robustness and longevity of the system are the major concerns. Hydrogen attenuation, liquid ingress and micro-bending effects are the three factors that will give rise to either intrinsic or extrinsic energy loss. Excessive losses will lead to a gradual degradation in measurement range or complete loss of signal in the extreme case. Although various technologies have been developed to address the hydrogen darkening problem, such as the chemically resistant coating material and dual laser operation developed by Halliburton, this issue still remains a difficult task (Jacobs, 2014).

Downhole erosion is another issue that needs to be solved for application in hydraulic fracturing. A recent study of the 35 wells installed with OFS in North America showed that only 35% of the wells survived to collect data in hydraulic fracture stimulation. Most of the fiber optic cables fail prematurely during, or shortly after, deployment or during the simulation, including failure in downhole, surface and supporting data collection systems (Bateman et al., 2013).

Other issues occurred during field application include poor depth correlation (fiber coiled up in the stainless steel tube) and large data set (5 TB data is generated for a typical hydraulic fracturing job).

Above all, no actual laboratory tests have been done to evaluate the fiber optic sensor accuracy, sensitivity, stability, robustness and the effect of crosstalk under simulated downhole conditions. Without the laboratory verification test, there is no guarantee that the sensor measured downhole data reflects the real in-situ state of the well and reservoir.

2.3. DISCUSSION

The literature review revealed the gaps in the current monitoring technologies related to CO_2 sequestration monitoring, including:

(1) high cost

(2) time-consuming sample collection

(3) low spatial resolution

(4) sensor robustness problem

(5) system longevity issues

A robust and cost-effective well monitoring technology is greatly in need to tackle the problems for a feasible permanent downhole monitoring system in geologic CO_2 sequestration.

Based on the current installation of fiber optic sensing system, a permanently installed behind-casing monitoring system is considered the best option for geologic CO_2 sequestration. A single ended coaxial cable DTS system that doesn’t rely on the surface reference temperature bath or downhole gauge is desired for a truly distributed temperature sensing. A helically wrapped coaxial cable DSS system is required for real-time casing deformation imaging. The sensor needs to be proved to work under simulated downhole conditions, and the casing deformation monitoring system needs to be verified to be able to monitor and evaluate the wellbore stability during CO_2 sequestration.

3. RESEARCH OBJECTIVES

The main objective of this research is to develop a feasible intelligent well monitoring system based on distributed coaxial cable temperature/strain sensors, and to conduct finite element analysis of the wellbore integrity during CO_2 sequestration to detect wellbore leakage risk, which can be further categorized into the following sub tasks.

(1) Set up an experimental apparatus to test the coaxial cable temperature sensor under simulated downhole conditions. The sensor properties under test include accuracy, sensitivity, stability, and pressure crosstalk effect.

(2) Modify and improve the temperature sensor design based on the test data acquired in the first step to improve the sensor performance under simulated downhole conditions.

(3) Develop a feasible distributed temperature/strain sensor downhole deployment strategy for the intelligent well monitoring system.

(4) Create a lab-scale prototype of the intelligent well monitoring system, and conduct tests on the system to verity the real-time monitoring ability of casing deformation, including axial compression, bending, and ovalization.

(5) Rationalize an appropriate finite element model to study the feasibility of using the developed sensing system in wellbore integrity monitoring by conducting a parametric analysis of the effect of CO_2 injection conditions.

The first two objectives are addressed by the first paper “Laboratory Evaluation of Distributed Coaxial Cable Temperature Sensor for Application in CO_2 Sequestration Well Characterization”. The third and fourth objectives are addressed by the second paper “Development and Evaluation of the Coaxial Cable Casing Imager-A Cost-Effective

Solution to Real-Time Downhole Monitoring for CO_2 Sequestration Wellbore Integrity". The last objective is addressed by the third paper "Feasibility of Real-Time Evaluation of the CO_2 Sequestration Wellbore Integrity with the Coaxial Cable Casing Imager".

PAPER

I. LABORATORY EVALUATION OF DISTRIBUTED COAXIAL CABLE TEMPERATURE SENSORS FOR APPLICATION IN CO2 SEQUESTRATION WELL CHARACTERIZATION

Yurong Li[1], Wenge Zhu[2], Baokai Cheng[2], Runar Nygaard[3], Hai Xiao[2]
[1]Missouri University of Science and Technology, [2]Clemson University, [3]Oklahoma State University

Abstract: Downhole monitoring plays a crucial part in a geological carbon dioxide (CO_2) sequestration project, especially in providing early warnings of failure. However, most downhole monitoring technologies are often low in spatial resolution and time-consuming, or expensive and have system longevity issues. To address this issue a robust and cost effective distributed coaxial cable Fabry-Perot interferometer based temperature sensor is proposed for real-time downhole monitoring.

The coaxial cable sensor (CCS) is made in house and tested using a high pressure high temperature (HPHT) testing apparatus to study the sensor accuracy, sensitivity, stability and crosstalk effect in simulated downhole conditions. The laboratory test results indicate that the sensor can work under simulated downhole conditions of pressures up to 1000 psia and temperatures up to 110 °C. At 1 ATM, the sensor has an accuracy of about 1%. At 1000 psia, the hysteresis phenomenon is observed, but it is reduced and tends to stabilize after repeated heating and cooling treatments. The pressure crosstalk effect is observed on the flexible cable sensor and minimized on the rigid cable sensor.

The temperature and pressure range of the distributed CCS allows a long-term in-situ monitoring for a well depth up to 2500 feet, which would prove great value in detecting

temperature change associated with wellbore leakage that may lead to ground water contamination.

Keywords: Geologic carbon sequestration, downhole monitoring, distributed sensing, temperature sensor, coaxial cable sensors.

Introduction

A program for monitoring of CO_2 distribution is required once injection begins in order to manage the injection process, delineate and identify leakage risk or actual leakage that may endanger underground source of drinking water, verify and provide input into reservoir models[1-3], and provide early warnings of failure. Monitoring of the wells, deep subsurface, shallow subsurface and ground surface is expected to continue for a long time after the injection is terminated for safety and to confirm predictions of storage behavior[4]. To ensure the public safety as well as to determine the carbon credits in a future cap and trade system, monitoring and modeling of sequestration have to reach a high degree of accuracy. The objective is to reach 99% accuracy in a monitoring and verification program[5]. However, the predictions based on current methodology are far too uncertain to achieve the goal to account for 99% of the injected CO_2[6]. In addition, no carbon sequestration and storage project completed to date has demonstrated robust commercial monitoring. Work remains to link the regulatory and accreditation requirements to the risk assessment, and then to monitoring tool selection and deployment plan over the project's lifetime and area via a monitoring plan[7].

Various sensing technologies have been explored and applied in the CO_2 sequestration projects ranging from small injection pilots to much larger longer-term commercial operations for characterization and monitoring of subsurface geologic environments[8]. However, the current monitoring technologies have the following limitations: (1) Time-consuming. For example, in incidents of groundwater contamination, a density of about 50-500 wells per km^2 are required for contaminant plume mapping and remediation[9]. The massive field sample collection work and high sampling frequency may lose the time effectiveness of the collected data. (2) High cost. The average monitoring cost consists a large portion of the overall storage cost, especially seismic surveys[10, 11]. A monitoring cost estimate of the Wabamun Area Sequestration Project (WASP) showed that 4D seismic to be the most expensive monitoring methods when well cost was not included[12]. (3) Low sensitivity. When detecting the amount of CO_2 with seismic surveys, if the CO_2 is homogeneously distributed, 1% is detectable. However, if the CO_2 is patchily distributed, anything below 18% is indistinguishable from brine[13]. (4) Low spatial resolution. Depending on the relative position of the observation well, the resolution of the microseismic results might be a few meters, which is not sufficient to answer detailed questions regarding points of fracture initiation from the wellbore[14]. (5) Impact of environmental factors. Detection of CO_2 leakage signals using geochemical parameters is affected by various environmental factors, such as the presence of reactive minerals in the aquifer sediments, initial aquifer chemistry, and groundwater recharge and extraction[15].

Optical fiber sensors (OFS) are being progressively applied for downhole monitoring in oil industry due to their multiplexing ability and reduced size compared with other wire-connected downhole sensors. Fiber optic based downhole temperature, pressure, strain and acoustic sensors for petroleum industry application are currently available[16-20]. However, some of their inherent drawbacks need to be addressed when they are considered as an alternative to conventional electronic transducers. Robustness and longevity of the system are the major concerns. Hydrogen attenuation, liquid ingress and micro-bending effects are the three factors that will give rise to either intrinsic or extrinsic energy loss. Excessive losses will lead to a gradual degradation in measurement range or complete loss of signal in the extreme case[21]. Although technologies have been developed to enhance the fiber performance under a harsh environment, such as the chemically resistant coating and dual-laser technology developed by Halliburton, hydrogen darkening remains a concern[22]. A recent study shows that due to the fragility of the optical fibers, of all the 26 wells completed with the OFS in North America, only 35% survived to collect production data[23]. The high cost of the fiber optic distributed temperature sensing (DTS) system is another issue. The cost of DTS installation can be as much as 20% of the total well cost. Moreover, extra cost is required for the DTS boxes and data analysis service[24].

The current installation of the fiber optic DTS system would cause even more issues. A reference temperature bath or oven is required within or nearby the instrumentation box on surface to provide “offset” correction. If the only tie-in point for measuring accurate temperature is the bath in the instrument box, the temperature log is subjected to an unknown amount of drift with depth, so an additional temperature gauge is needed at the bottom of the well if the system is a single-end deployment. Besides, the pumping process of the fiber lines into the tubing will make them coiled up within the tube, which would result in a wrong depth correlation[24].

To address these concerns this paper studies the potential of using coaxial cable sensors (CCS) for permanent installation in the wellbore.

Coaxial cable Fabry-Perot interferometer (CCFPI) temperature sensor

As Figure 1 shows, the Fabry-Perot interferometer is constructed by two reflectors on a coaxial cable. An electro-magnetic (EM) wave propagating inside the coaxial cable is partially reflected at the first reflector due to the characteristic impedance discontinuity. The remaining wave transmitting through the first reflector is once again partially reflected at the second reflector (Figure 2 (a)). The two reflected waves interfere coherently to generate a constructive or destructive interference signal. When the frequency of EM wave is swept, an interferogram in frequency domain is observed (Figure 2 (b))[25].

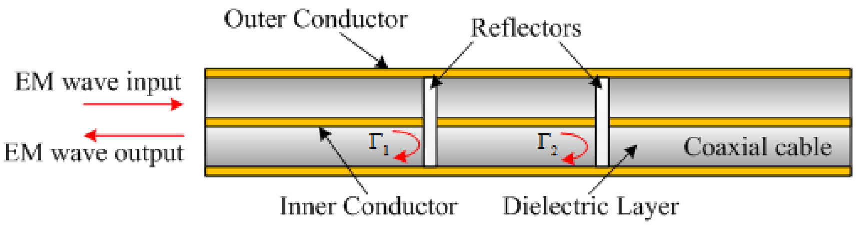

Figure 1. Schematic of the CCFPI temperature sensor.

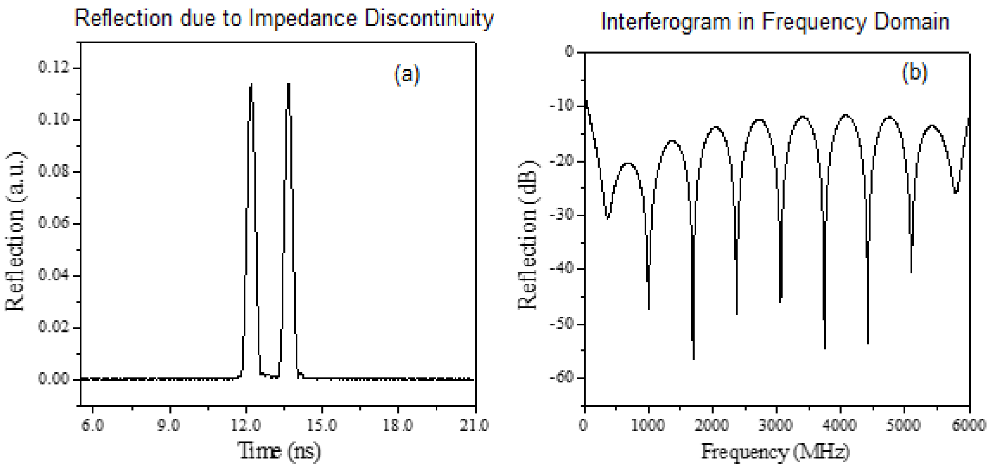

Figure 2. Time domain and frequency domain of the generated interferogram.

Suppose the reflection coefficients of the two reflectors are equal, the two reflected voltages (V_1 and V_2) are expressed as,

$$V_1 = \Gamma\cos(2\pi ft), \text{ and } V_2 = \Gamma\cos\left[2\pi f(t+\Delta t)\right], \text{ where } \Delta t = \frac{2d\sqrt{\varepsilon_r}}{c} \tag{1}$$

where Γ is reflection coefficient of the reflectors; f is the frequency of the wave; Δt denotes time delay between the two reflected waves; d is the spacing between two reflectors; ε_r denotes the dielectric constant of the inner material of the cable; c is the speed of light in vacuum. The time delay (Δt) is related with the spacing (d) and the speed of the wave propagating in the cable ($c/\sqrt{\varepsilon_r}$). The total reflected voltage (V) is the superposition of the two reflected voltages (V_1 and V_2), given by,

$$V = 2\cdot\Gamma\cos\left(\pi f\Delta t\right)\cos\left[2\pi f\left(t+\frac{\Delta t}{2}\right)\right] \tag{2}$$

Equation 2 shows that both the amplitude and phase of the reflected voltage are related to the frequency and the delay. Specifically, the reflected voltage spectrum exhibits sine-wave in amplitude. The frequencies of the interference peaks are given as,

$$f_N = \frac{N}{\Delta t}, N = 1, 2, 3..., \tag{3}$$

In differential form, the relative frequency shift is then,

$$\frac{\Delta f_N}{f_N} = -\frac{\Delta d}{d} - \frac{1}{2}\frac{\Delta\varepsilon_r}{\varepsilon_r} \tag{4}$$

When the ambient temperature around the cable increases by ΔT, both dielectric constant (ε_r) and length (d) would change by $\Delta\varepsilon_r$ and Δd, respectively,

$$\frac{\Delta d}{d} = \alpha_{CTE}\Delta T, \quad \text{and} \quad \frac{\Delta\varepsilon_r}{\varepsilon_r} = \alpha_{TCK}\Delta T \tag{5}$$

whereα_{CTE} and α_{TCK} are the temperature coefficients of thermal expansion and dielectric constant, respectively. Combining these two factors, the relative frequency shift can be rewritten as,

$$\frac{\Delta f_N}{f_N} = -\left(\frac{\alpha_{TCK}}{2} + \alpha_{CTE}\right)\Delta T \qquad (6)$$

The equation above indicates that the relative frequency shift is linear to the temperature change. Further, the temperature dependence of dielectric constant is two times larger than that of thermal expansion.

Experimental setup

A high pressure high temperature (HPHT) sensor testing system is manufactured for sensor testing under various temperature and pressure conditions. A picture of the whole system set up is shown in Figure 3. The HPHT testing cell is made of stainless steel as a container for fluid (water used here), thermocouple and coaxial cable temperature sensor. The cell has a length of 30 cm and an inner diameter of 5 cm with a maximum pressure capability of 5,000 psia. O-rings are used to seal the cable on the end caps of the testing cell. The temperature in the testing cell is controlled in closed-loop form. The thermocouple inside the cell feedbacks the fluid temperature to the controller (Omega CN7523, Stamford, CT, USA), which controls a flexible silicone-rubber heating pad with a nominal maximum temperature of 232 °C that is attached to the outer wall of the testing cell. Flexible fiberglass insulation is wrapped around the testing cell to prevent heat loss. The pressure within the testing cell is controlled by a pump (Teledyne Isco 100DX, Lincoln, NE, USA) which has a maximum pressure rating of 10,000 psia and a resolution of ±1 psia. The reflection spectrum of the cable is monitored by a vector network analyzer (VNA, HP 8753ES, Santa Clara, CA, USA).

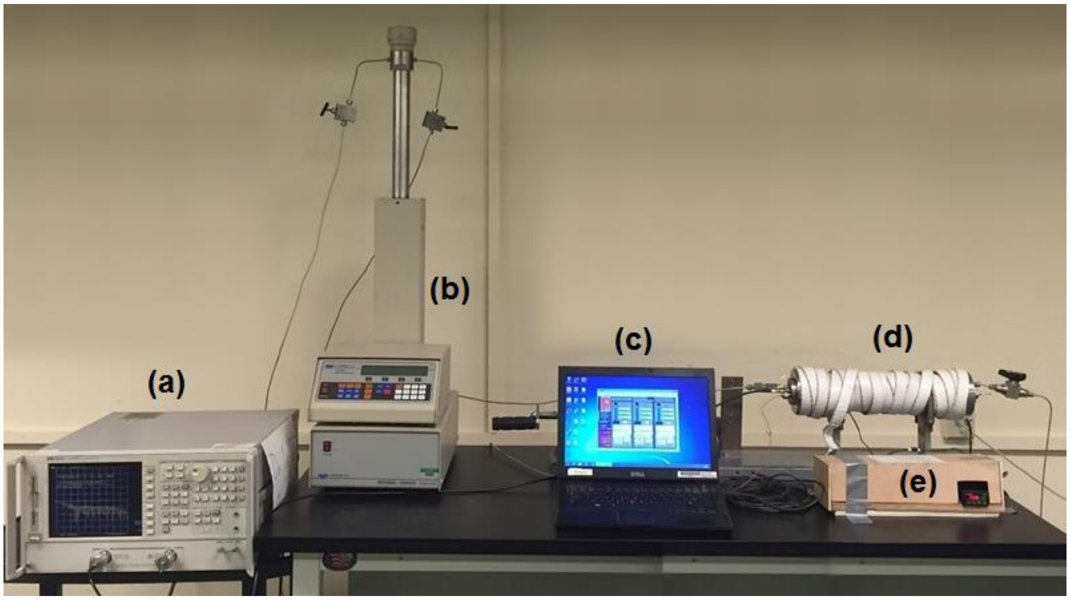

Figure 3. Picture of the HPHT Sensor Testing System.

Results

Flexible CCFPI temperature sensor.

Two structural reflectors are implanted in the coaxial cable (Pasternack RG400, Irvine, CA, USA) to construct a single CCFPI temperature sensor, as shown in Figure 4. Two copper crimp rings are firmly compressed onto the cable with a separation of 4 inch to deform the outer conductor and generate the characteristic impedance discontinuities. The copper crimp rings could survice in harsh environment application. When a radio frequency (RF) waveform is transmitted into the cable, the deformed locations will generate two reflections and form the interference pattern in the frequency domain.

Figure 4. Picture of the flexible CCFPI temperature sensor.

Sensor performance at atmospheric pressure.

The sensor is first tested under 1 ATM with temperature step increasing from room temperature (RMT) to 100 °C then air cooled to room temperature. Figure 5 shows a boxplot comparison between CCS and thermocouple (TC) measured temperature when the testing cell is under a relatively constant temperature condition. The temperature measured by the two methods shows a very good consistency, and during the test the sensor shows an instantaneous response to the temperature change.

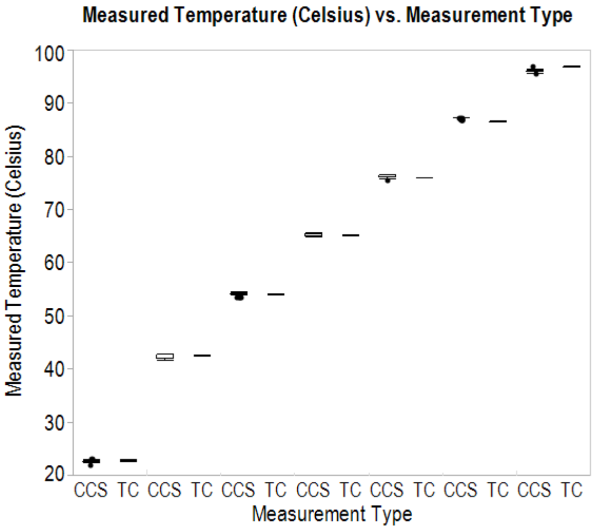

Figure 5. Boxplot comparison between CCS and TC measured temperature at 1 ATM.

Sensor performance at 1000 psia.

To investigate the sensor response under a higher pressure condition, the testing cell is then pressurized to 1,000 psia with temperature step increasing from room temperature to 110 °C and then air cooled to room temperature. The heating and cooling cycle is repeated for 5 times and the boxplot of sensor measurement deviation (sensor measured temperature minus thermocouple measured temperature) for the 5 cycles is shown in Figure 6 (a)-(c). The results indicate that for the 1st cycle, there is a poor consistency between the two measurement methods, and the hysteresis is very large. However, as the cycle number increases, the consistency tends to be better. And further analysis of the sensor sensitivity and hysteresis change shows that the sensor tends to have a stable sensitivity and the hysteresis tends to become close to zero as the cycle number increases.

To verify the test results, the same tests are conducted on a second coaxial cable temperature sensor, and the same conclusion can be made from the results shown in Figure 6 (d)-(f). These two sets of tests indicate that the sensor needs to be pre-treated (multiple heating-cooling cycles) to have a stable performance under a high pressure condition.

Sensor long-term stability.

To test the sensor stability, the testing cell was pressurized to 1000 psia and the temperature hold constant at both 40 °C and 90 °C each for more than 40 hours. Figure 7 shows the boxplot comparison of the pre-treated CCS and TC measured temperature at 40 °C and 90 °C. At 40 °C, the CCS measured temperature is 38 °C ± 0.6 °C, compared to the TC measured temperature of 38.1 °C ± 0.2 °C. While at 90 °C, the CCS measured temperature is 88.2 °C ± 1.3 °C, compared to the TC measured temperature of 86.9 °C ±

0.2 °C. The result shows that the sensor has a more stable performance at lower temperature, with higher accuracy and smaller measurement deviation.

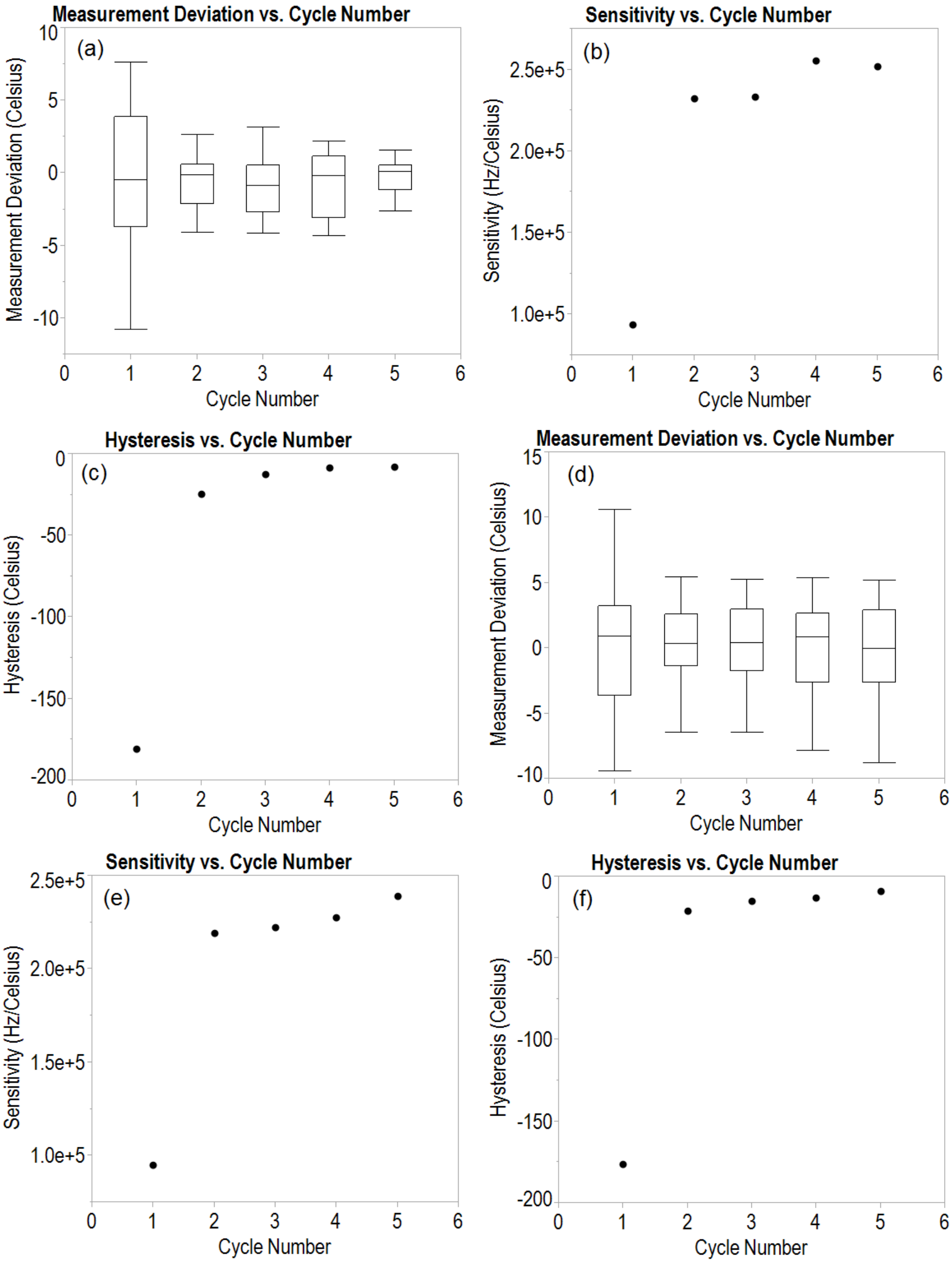

Figure 6. Test results of the sensor at 1000 psia for five cycles where (a) Sensor 1 measurement deviation boxplot (b) Sensor 1 sensitivity change (c) Sensor 1 hysteresis change (d) Sensor 2 measurement deviation boxplot (e) Sensor 2 sensitivity change (f) Sensor 2 hysteresis change.

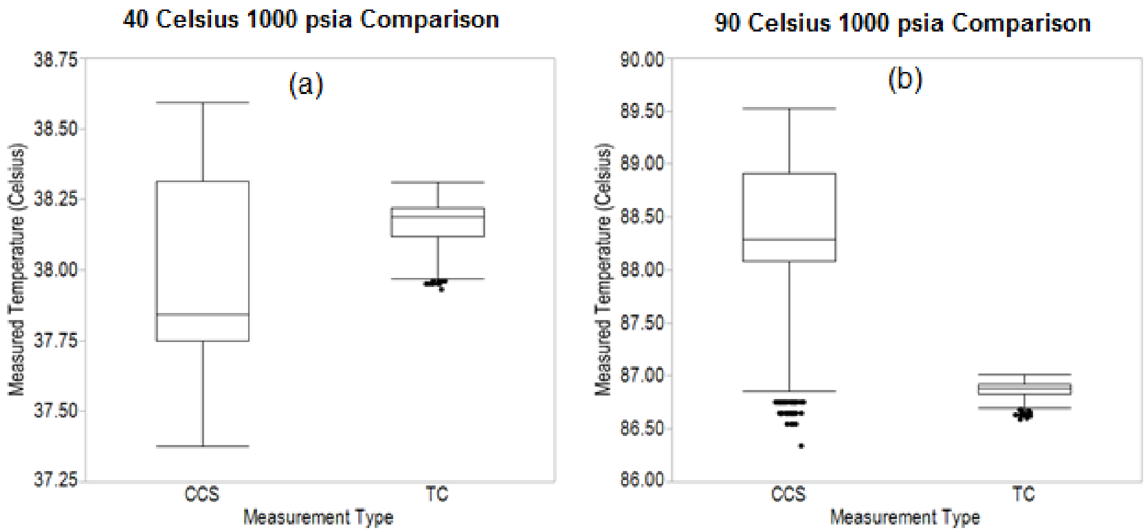

Figure 7. Boxplot comparison of CCS and TC measured temperature at 1000 psia over a long period where (a) at 40 °C (b) at 90 °C.

Sensor pressure crosstalk.

The pressure crosstalk phenomenon has been observed during the test while decreasing the pressure from 1000 psia to 1 ATM at a constant temperature at 90 °C, as shown in Figure 8. To study the influence of pressure on the pre-treated temperature sensor, the pressure is step increased from 1 ATM to 1000 psia and then step decreased back to 1 ATM at both 40 °C and 80 °C. Figure 9 shows the sensor frequency change with respect to changing pressure at 40 °C and 80 °C. It can be observed that the sensor has a constant response ratio to pressure at a constant temperature regardless of increasing or decreasing pressure. However, at different temperatures, the response ratios are different.

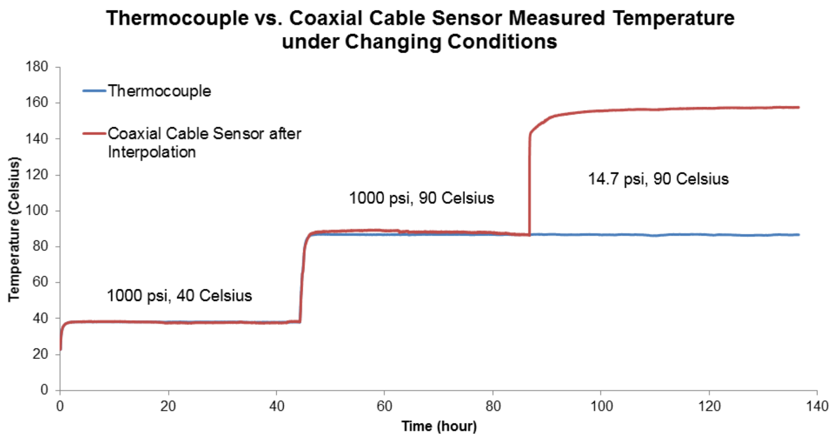

Figure 8. Observation of pressure crosstalk when decreasing pressure from 1000 psia to 1 ATM at 90 °C.

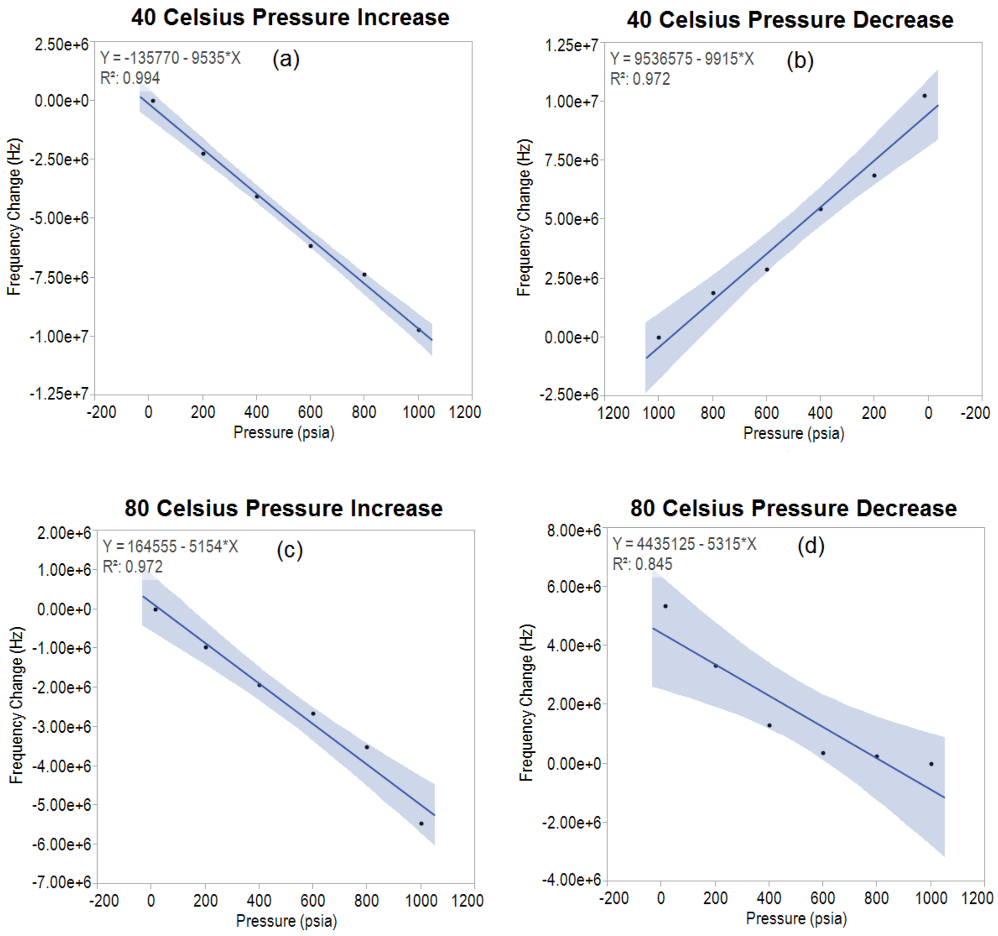

Figure 9. Sensor frequency change with respect to pressure change at 40 °C and 80 °C.

To quantify the pressure crosstalk, a central composite experiment is designed and conducted as shown in Table 1. A pre-treated sensor is tested under the testing scheme with two repetitions. An analysis of variance (ANOVA) and regression analysis is conducted with JMP® for the central composite experiment model. The ANOVA table of the testing results shows that temperature multiplied with pressure has a P-value smaller than the significance level of 0.05, as shown in Table 2, which means that temperature and pressure interaction exists.

Table 1. Central composite experiment for flexible CCFPI temperature sensor.

Reference Parameters

Temperature (°C)	Pressure (psia)	Frequency 1 (Hz)	Frequency 2 (Hz)
25.00	14.70	3680.5012e+6	3679.0315e+6

Testing Parameters

Temperature (°C)	Pressure (psia)	Frequency Change 1 (Hz)	Frequency Change 2 (Hz)
37.45	158.99	-1.8543e+6	-1.8898e+6
37.45	855.71	-8.3041e+6	-8.0382e+6
97.55	158.99	15.4262e+6	16.1941e+6
97.55	855.71	4.1171e+6	5.1149e+6
25.00	507.35	-7.8006e+6	-7.1049e+6
110.00	507.35	12.2747e+6	13.1683e+6
67.50	14.70	8.5368e+6	8.8525e+6
67.50	1000.00	-4.2483e+6	-3.5246e+6
67.50	507.35	1.6835e+6	1.6329e+6
67.50	507.35	-0.3518e+6	0.3053e+6

The regression analysis gives a predictive model as,

$$\Delta F = 817 \times 10^3 + 10.43 \times 10^6 \times \left(\frac{T-67.5}{42.5}\right) - 6.24 \times 10^6 \times \left(\frac{P-507.35}{492.65}\right) - 2.45 \times 10^6 \times \left(\frac{T-67.5}{42.5}\right) \times \left(\frac{P-507.4}{492.7}\right) + 1.86 \times 10^6 \times \left(\frac{T-67.5}{42.5}\right) \times \left(\frac{T-67.5}{42.5}\right) + 1.62 \times 10^6 \times \left(\frac{P-507.4}{492.7}\right) \times \left(\frac{P-507.4}{492.7}\right) \tag{7}$$

where ΔF is sensor frequency change, *Hz*; T is temperature, °*C*; P is pressure, psia.

Table 2. ANOVA table for flexible CCFPI temperature sensor.

Analysis of Variance

Source	**DF**	**S.S.**	**M.S.**	**F Ratio**
Model	5	1.2035e+15	2.4070e+14	580.8188
Error	14	5.8019e+12	4.1440e+11	**Prob>F**
C. Total	19	1.2093e+15		<0.001*

Effect Tests

Source	**Nparm**	**DF**	**S.S.**	**F Ratio**	**Prob>F**
Temp	1	1	8.7025e+14	2099.9250	<0.0001*
Pres	1	1	3.1150e+14	751.6453	<0.0001*
Temp*Pres	1	1	1.1981e+13	28.9098	<0.0001*
Temp*Temp	1	1	7.8759e+12	19.0047	<0.0007*
Pres*Pres	1	1	6.0097e+12	14.5015	<0.0019*

With the predictive equation, for a known pressure and sensor frequency change, the sensor measured temperature can be calculated. Two verification tests are performed to compare the sensor measured temperature based on the predictive equation and the actual temperature. Table 3 shows the test results for the verification tests. As it indicates, the sensor measured temperature is around 10 °C lower than the actual temperature with the predictive equation.

Table 3. Comparison of sensor measured temperature and actual temperature based on the predictive equation.

Actual temperature (°C)	**Actual pressure (psia)**	**Measured temperature (°C)**
40	200	30.91
80	800	69.31

Rigid CCFPI temperature sensor.

The main reason of the pressure crosstalk is the pressure induced elongation of the flexible coaxial cable. Both the jacket and the dielectric material of the flexible cables are polymers, which have small Young’s modulus thus large Poisson’s ratio. To minimize the pressure crosstalk effect, a rigid coaxial cable with stainless steel jacket and ceramic dielectric was used because of their smaller Poisson’s ratio. The two reflectors are created by making two separated ring grooves on the ceramic dielectric, as shown in Figure 10.

Figure 10. Picture of the semi-rigid CCFPI temperature sensor.

Table 4. Central composite experiment for rigid CCFPI temperature sensor.

Reference Parameters

Temperature (°C)	Pressure (psia)	Frequency 1(Hz)	Frequency 2(Hz)
25.00	14.70	3374.9788e+6	3371.2429e+6

Testing Parameters

Temperature (°C)	Pressure (psia)	Frequency Change 1 (Hz)	Frequency Change 2 (Hz)
25.00	507.35	-0.2309e+6	-0.2734e+6
37.45	158.99	-1.8997e+6	-1.4715e+6
37.45	855.71	-2.4159e+6	-2.0138e+6
67.50	14.70	-6.5933e+6	-4.6783e+6
67.50	507.35	-6.7790e+6	-4.9442e+6
67.50	1000.00	-7.0758e+6	-5.3165e+6
67.50	507.35	-6.8216e+6	-4.9662e+6
97.55	158.99	-12.2603e+6	-8.8203e+6
97.55	855.71	-13.0297e+6	-9.7322e+6
110.00	507.35	-14.7636e+6	-11.1504e+6

The same central composite experiment with two repetitions was conducted on the sensor, as shown in Table 4. The ANOVA table (Table 5) shows that the only influencing parameter is temperature. The P-value for pressure is larger than a significance level of 0.05, which means that pressure has no effect on the sensor frequency change.

The regression analysis gives a predictive model as,

$$\Delta F = -6.262 \times 10^{6} - 6.362 \times 10^{6} \times \left(\frac{T-67.5}{42.5}\right) \tag{8}$$

Table 5. ANOVA table for rigid CCFPI temperature sensor.

Analysis of Variance

Source	**DF**	**S.S.**	**M.S.**	**F Ratio**
Model	5	3.2627e+14	6.5250e+13	35.8282
Error	14	2.5498e+13	1.8210e+12	**Prob>F**
C. Total	19	3.5177e+14		<0.001*

Effect Tests

Source	**Nparm**	**DF**	**S.S.**	**F Ratio**	**Prob>F**
Temp	1	1	3.2379e+14	177.7777	<0.0001*
Pres	1	1	7.5255e+11	0.4132	0.5307
Temp*Pres	1	1	4.8519e+10	0.0266	0.8727
Temp*Temp	1	1	1.1556e+12	0.6345	0.4390
Pres*Pres	1	1	3.7849e+10	0.0208	0.8874

To verify the accuracy of the regression model, the sensor frequency change was measured at a constant temperature of 25 °C while pressure is increased from 1 ATM to 1000 psia. The equivalent temperature change is 2.9 °C according to the predictive equation.

Hysteresis phenomenon is also observed on the rigid CCFPI temperature sensor, as shown in Figure 11. Similar to the flexible CCFPI temperature sensor, the hysteresis drops down after one cycle, but compared to the flexible CCFPI temperature sensor, the hysteresis immediately drops down to zero and remains at zero, instead of gradually decreasing.

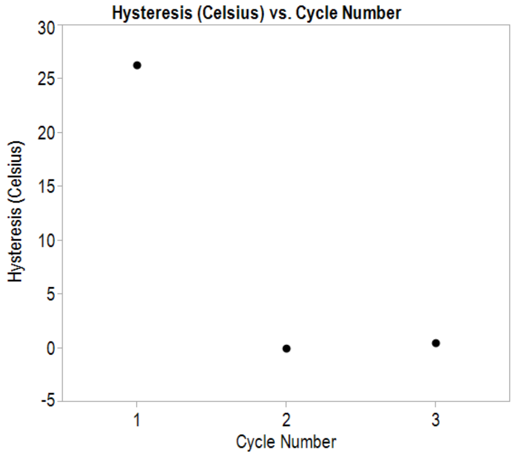

Figure 11. Hysteresis vs. cycle number.

Discussion

The flexible CCFPI temperature sensor exhibits an accuracy of more than 1% at atmospheric pressure (Figure 5). At 1000 psia, the sensitivity tends to stabilize and the hysteresis is reduced almost to zero after repeated treatment cycles (Figure 6), and the sensor is more stable at low temperature than at high temperature (Figure 7). Pressure crosstalk has a very large influence on the sensor measurement (Figure 8). Compared to the flexible sensor, the pressure crosstalk and hysteresis are both greatly reduced on the rigid sensor. The hysteresis is reduced to 0 after one treatment cycle at 1000 psia (Figure 11), and the analysis of variance of the central composite experiment showed that pressure has no effect on the sensor measurement (Table 5). However, the equivalent temperature change is 2.9 °C when pressure is increased from 1 ATM to 1000 psia at 25 °C. This might be due to the limited number of test repetition. More test repetition is required for a more accurate predictive model.

Several factors can cause the reduction of sensor accuracy. The VNA used in the tests has a resolution of 1601 points for a frequency up to 6 GHz, while VNA with much higher resolution is available in the market. Although interpolation is applied on the VNA frequency reading, a higher VNA resolution is still required for a more accurate frequency change detection. Besides, the pressure and temperature maintaining of the testing cell is controlled by the pump and temperature controller. Pump pulsation and thermal conduction between the testing cell and the environment may reduce the system stability during the test.

The testing of the distributed CCFPI temperature sensor under simulated downhole conditions fills in the gap where the fiber optic sensors are only manufactured and tested under surface conditions, which is crucial since pressure could affect the sensor accuracy. And compared to the OFS, the system installation would be simplified due to the fact that no reference temperature bath at surface or downhole temperature gauge is needed for temperature calibration.

The testing results under simulated downhole conditions proved that the sensor can be deployed downhole permanently for a well depth up to 2500 ft, which would prove great value in detecting wellbore leakage that will contaminate the ground water. As a novel downhole sensing technology, the low cost and robustness of the distributed coaxial cable sensors will not only lower the downhole monitoring cost, but will also enhance the monitoring system stability and longevity, which will provide continuous monitoring during each stage of well operation and throughout the lifetime of the well to provide input to reservoir characterization, wellbore stability analysis, fracture operation evaluation and production appraisal.

Conclusions

In this work, a novel idea of distributed coaxial cable temperature sensor is put forward and the sensor is fabricated and tested with a HPHT testing apparatus in water to study the sensor accuracy, sensitivity, long-term stability and crosstalk effect in simulated downhole conditions. A response surface method (central composite experimental design) is used to study the individual and combined effect of temperature and pressure on the sensor measurement. A regression analysis is conducted and a prediction equation is developed to quantify the temperature and pressure effect.

Acknowledgements

The authors thank the research engineering technicians Jeffrey Heniff and John Tyler from the Rock Mechanics and Explosives Research Center of Missouri University of Science and Technology for the help on the experimental setup. The material presented is from the work supported by the Department of Energy under Award Number DE-FE0009843.

References

1. Zhang R, Winterfeld PH, Yin X, Xiong Y, Wu YS. Sequentially coupled THMC model for CO_2 geological sequestration into a 2D heterogeneous saline aquifer. *Journal of Natural Gas Science and Engineering*. 2015 Nov 30; 27: 579-615.

2. Zhang R, Xiong Y, Winterfeld PH, Yin X, Wu YS. A novel computational framework for thermal-hydrological-mechanical-chemical processes of CO_2 geological sequestration into a layered saline aquifer and a naturally fractured enhanced geothermal system. *Greenhouse Gases: Science and Technology*. 2015 Dec 1.

3. Zhang R, Yin X, Winterfeld PH, Wu YS. A fully coupled thermal-hydrological-mechanical-chemical model for CO_2 geological sequestration. *Journal of Natural Gas Science and Engineering*. 2016 Jan 31; 28: 280-304.

4. U.S. EPA. *Geologic CO_2 sequestration technology and cost analysis*. http://water.epa.gov/type/groundwater/uic/class6/upload/[accessed 21 March 2014]

5. NETL. Project solicitation: innovative and advanced technologies and protocol for monitoring/verification/accounting (MVA), simulation, and risk assessment of carbon dioxide (CO_2) sequestration in geologic formations. http://www.netl.doe.gov/business /solicitations/fy09[accessed 17 November 2013]

6. NETL. Project solicitation: technologies to ensure permanent geologic carbon storage. http://www.netl.doe.gov/business/solicitations/fy12[accessed 17 November 2013]

7. Hovorka SD. In quest of robust and commercial CO_2 monitoring. *Greenhouse Gases: Science and Technology*. **2(3)**:145-7 (2012).

8. Jenkins C, Chadwick A, Hovorka SD. The state of the art in monitoring and verification—Ten years on. *International Journal of Greenhouse Gas Control*. **40**:312-49 (2015).

9. May F, Waldmann S. Tasks and challenges of geochemical monitoring. *Greenhouse Gases: Science and Technology*. **4(2)**:176-90 (2014).

10. Rubin ES, Davison JE, Herzog HJ. The cost of CO_2 capture and storage. *International Journal of Greenhouse Gas Control*. **40**: 378-400 (2015).

11. Benson SM, Gasperikova E, Hoversten GM. Monitoring protocols and life-cycle costs for geologic storage of carbon dioxide. In Proceedings of the 7th International Conference on Greenhouse Gas Control Technologies (GHGT-7) 2004 Sep 5 (pp. 1259-1266).

12. Nygaard, R. and Lavoie, R. *Project cost estimate-Wabamun area CO_2 sequestration project (WASP)*. https://www.ucalgary.ca/wasp/Economic%\20and%20Cost%20 Analysis.pdf[accessed 12 February 2014]

13. Cairns G, Jakubowicz H, Lonergan L, Muggeridge A. Issues regarding the use of time-lapse seismic surveys to monitor CO_2 sequestration. In SEG Technical Program Expanded Abstracts 2010 Jan 1 (pp. 1236-1240).

14. Holley EH, Zimmer U, Mayerhofer MJ, Samson E. Integrated analysis combining microseismic mapping and fiber-optic distributed temperature sensing (DTS). In Canadian Unconventional Resources and International Petroleum Conference 2010 Jan 1. Society of Petroleum Engineers.

15. Yang C, Hovorka SD, Young MH, Trevino R. Geochemical sensitivity to CO_2 leakage: detection in potable aquifers at carbon sequestration sites. *Greenhouse Gases: Science and Technology*. **4(3)**:384-99 (2014).

16. Costello C, Sordyl P, Hughes CT, Figueroa MR, Balster EP, Brown G. Permanent Distributed Temperature Sensing (DTS) Technology Applied in Mature Fields-A Forties Field Case Study. In SPE Intelligent Energy International 2012 Jan 1. Society of Petroleum Engineers.

17. Koelman JV, Lopez JL, Potters H. Fiber optic technology for reservoir surveillance. In International petroleum technology conference 2011 Jan 1. International Petroleum Technology Conference.

18. Molenaar MM, Fidan E, Hill DJ. Real-time downhole monitoring of hydraulic fracturing treatments using fibre optic distributed temperature and acoustic sensing. In SPE/EAGE European Unconventional Resources Conference & Exhibition-From Potential to Production 2012 Mar 20.

19. Tardy PM, Chang FF, Qiu X. Determining Matrix Treatment Performance from Downhole Pressure and Temperature Distribution: A Model. In International Petroleum Technology Conference 2011 Jan 1. International Petroleum Technology Conference.

20. Medina M, Torres CE, Sanchez J, Boida L, Leon AJ, Jones JA, Yicon C. Real-Time downhole monitoring of electrical submersible pumps rated to 250 degree C using fiber optic sensors: case study and data value in the Leismer SAGD project. In SPE Western Regional Meeting 2012 Jan 1. Society of Petroleum Engineers.

21. Williams GR, Brown G, Hawthorne W, Hartog AH, Waite PC. Distributed temperature sensing (DTS) to characterize the performance of producing oil wells. In Environmental and Industrial Sensing 2000 Dec 29 (pp. 39-54). International Society for Optics and Photonics.

22. Jacobs T. Downhole Fiber-Optic Monitoring: An Evolving Technology. *SPE Journal of Petroleum Technology*. **66(8)**:44-53 (2014).

23. Bateman K, Molenaar MM, Brown MD. Lessons Learned from Shell's History of Casing Conveyed Fiber Optic Deployment. In SPE Unconventional Resources Conference Canada 2013 Nov 5. Society of Petroleum Engineers.

24. Smolen JJ, van der Spek A. Distributed Temperature Sensing. A primer for Oil and Gas Production. 2003 May.

25. Huang J, Wang T, Hua L, Fan J, Xiao H, Luo M. A coaxial cable Fabry-Perot interferometer for sensing applications. *Sensors*. **13(11)**:15252-60 (2013).

II. DEVELOPMENT AND EVALUATION OF THE COAXIAL CABLE CASING IMAGER—A COST-EFFECTIVE SOLUTION TO REAL-TIME DOWNHOLE MONITORING FOR CO2 SEQUESTRATION WELLBORE INTEGRITY

Yurong Li[1], Baokai Cheng[2], Wenge Zhu[2], Runar Nygaard[3], Hai Xiao[2]

[1]Missouri University of Science and Technology, [2]Clemson University, [3]Oklahoma State University

Abstract: CO_2 leakage is a major concern in a geological carbon sequestration project due to the adverse environmental consequences, where the main leakage risk is identified to be along existing wells through a thick, low permeable cap rock. To pursue a robust and cost effective real-time downhole monitoring technology for CO_2 sequestration wellbore integrity, a permanently deployed coaxial cable casing imager is developed and evaluated in laboratory in this paper.

The prototype of the casing imager consists of evenly distributed coaxial cable strain sensors helically wrapped around the pipe. The system is deployed on both PVC pipe and steel pipe to test its performance in casing deformation monitoring, including axial compression, radial expansion, bending, and ovalization. The strain sensors are pre-stressed and then helically wrapped onto the pipe with high strength epoxy. Multiple LVDTs or strain gauges are used as independent measurement of the pipe actual deformation in comparison to the casing imager measured pipe deformation.

The test results demonstrated the ability of the lab-scale casing imager prototype in real-time casing deformation monitoring including axial compression, radial expansion, bending, and ovalization, which would prove great value in evaluating wellbore integrity state and providing early warnings of leakage risk that will contaminate the ground water during CO_2 injection. And the low cost and high robustness of the distributed coaxial cable sensors will greatly lower the downhole monitoring cost and increase the system longevity.

Keywords: Permanent Downhole Monitoring; CO_2 leakage; Distributed Coaxial Cable Sensor; Casing Deformation; Casing Imager

Introduction

CO_2 leakage induced problems such as groundwater contamination, plant stress, and biomass changes are the primary concerns in a geological carbon sequestration project[1-5]. Each CO_2 sequestration project will have its unique leakage risk assessment, but in sedimentary basins that have a history of oil and gas exploration and production, the main leakage risk is commonly identified to be along existing wells[6-9]. Since cement sheath is one of the primary barriers to prevent wellbore leakage and failure, and what happens during the cementing operation and thereafter can greatly affect the long term wellbore integrity[10], it is of great importance to monitor the downhole activities during the cementing and CO_2 injection process to provide early warnings of wellbore leakage.

Various sensing technologies have been explored and applied in the CO_2 sequestration projects ranging from small injection pilots to much larger longer-term commercial operations for monitoring of subsurface activities[11]. The conventional well-based monitoring technologies have been proved to have some limitations in field applications, including high cost[12-14], time-consuming sample collection[15], low spatial resolution[16], low sensitivity in CO_2 saturation monitoring[17], and easily affected by environmental factors such as the presence of reactive minerals[18]. And although a series of optical fiber sensors (OFS) are commercially available and have been widely used in the oilfield for the past twenty years[19], the fiber based downhole monitoring system is limited by its intrinsic drawbacks, such as hydrogen darkening, liquid ingress and micro-bending effects, which will give rise to either intrinsic or extrinsic energy loss[20].

The SureView^{TM} real-time compaction monitoring (RTCM) system—a fiber-optic Bragg-grating strain sensor based well tubular and sand screen deformation monitoring system, has been developed by Shell and Baker Hughes in 2005[21-25]. The system consists of distributed fiber optic strain sensors which are imbedded into the pre-cut helical groove on the outer casing. Laboratory scale experiments have demonstrated the system's ability to monitor and identify casing axial deformation, buckling, bending, ovalization, and a mixture of the deformation modes. However, the results also show that the system gives a vague estimation when determining the casing strain magnitude in each of the deformation modes[23].

The Febry-Perot interferometer based coaxial cable sensors have been developed in 2011[26-28], and a recent study proved that the sensors can perform with high accuracy under 110 °C and 1,000 psi[29]. Due to the low cost and high robustness of the coaxial cable sensors, and inspired by the SureView^{TM} RTCM system, a permanent downhole casing imaging system based on coaxial cable Fabry-Perot interferometer (CCFPI) strain sensors is developed and evaluated as a solution to real-time downhole monitoring for CO_2 sequestration wellbore integrity in this paper.

Methodology

Figure 1 (a) is the in-house made CCFPI strain sensor. As Figure 1 (b) shows, the Fabry-Perot interferometer is constructed by two reflectors on a coaxial cable. An electromagnetic (EM) wave propagating inside the coaxial cable is partially reflected at the first reflector due to the characteristic impedance discontinuity. The remaining wave transmitting through the first reflector is once again partially reflected at the second reflector (Figure 2 (a)). The two reflected waves interfere coherently to generate a constructive or destructive interference signal. When the frequency of EM wave is swept, an interferogram in frequency domain is observed (Figure 2 (b)). And when the ambient temperature remains constant, the relative frequency shift of the interferogram equals the change of distance between the two reflectors, which is the strain measured along the sensor length. For more details on the coaxial cable sensor working mechanism, please refer to Li et al.[29].

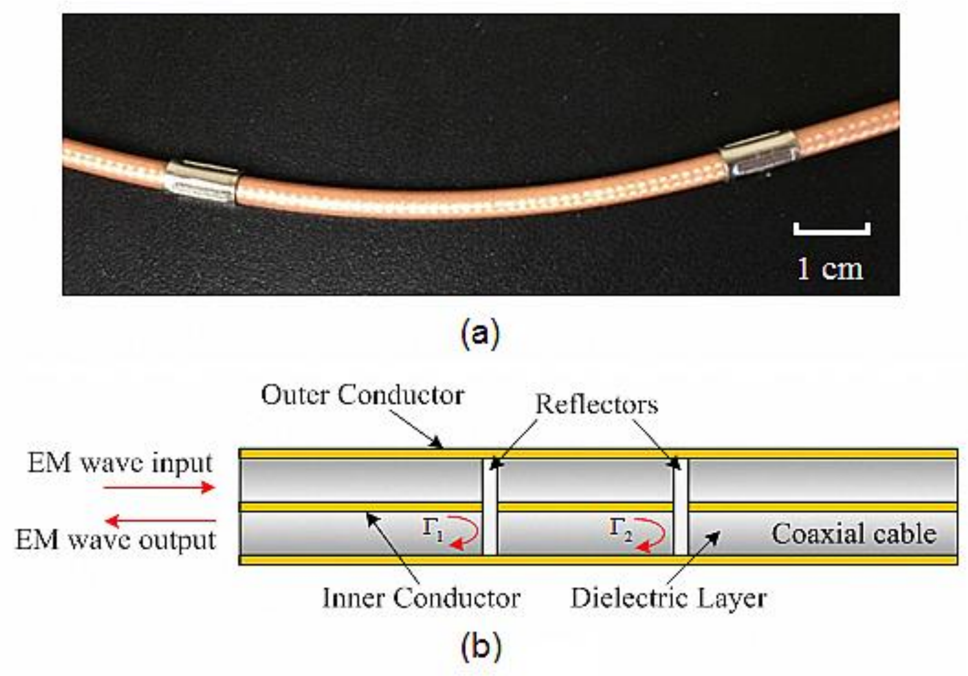

Figure 1. Schematic and picture of the in-house made CCFPI strain sensor.

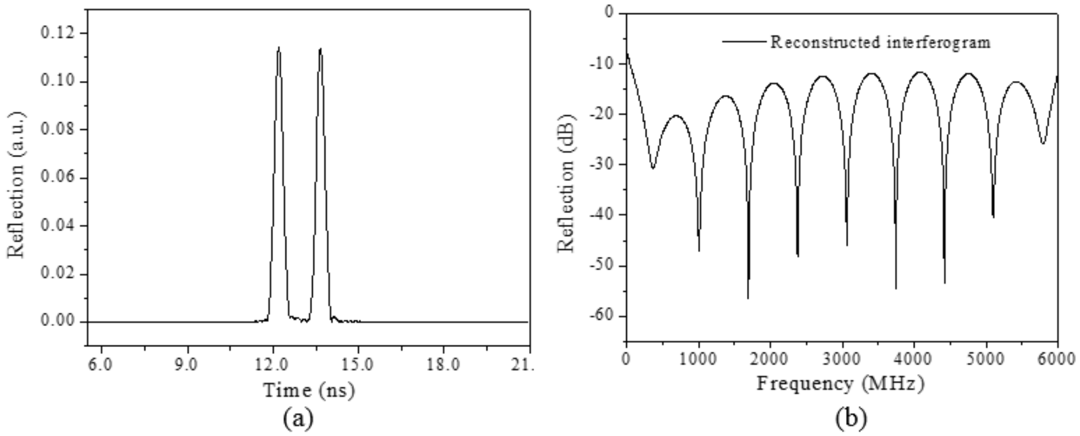

Figure 2. Time domain and frequency domain of the generated interferogram.

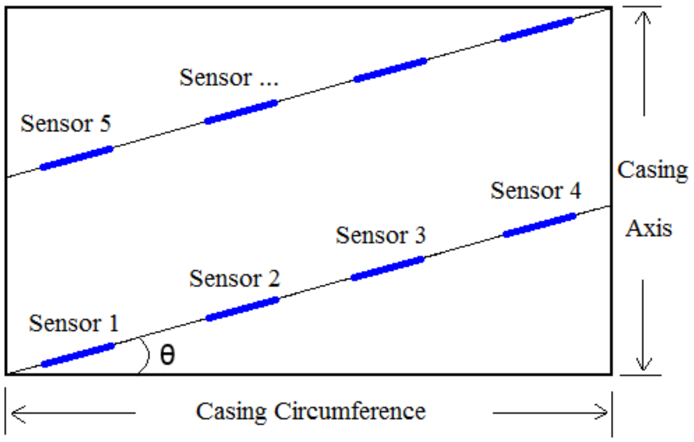

Figure 3. Schematic of helical attachment of cable to the casing.

Rambow et al.[25] introduced the helical wrapping of fiber-optic sensors on the casing to increase the measurable casing axial strain for limited sensor measurement ability. For a helically wrapped cable at θ degree (Figure 3), the strain on the sensor ε can be analytically related to the casing strain when the casing is subjected to axial compression (Equation 1), radial expansion (Equation 2), bending (Equation 3&4), and ovalization (Equation 5).

$$\varepsilon = K\left(1 - \sqrt{sin^2\theta(1-\varepsilon_a)^2 + cos^2\theta(1+\nu\varepsilon_a)^2}\right) \tag{1}$$

$$\varepsilon = K\left(1 - \sqrt{sin^2\theta(1-\nu\varepsilon_t)^2 + cos^2\theta(1+\varepsilon_t)^2}\right) \tag{2}$$

$$\varepsilon = K\left(1 - \sqrt{sin^2\theta\left(1-(\varepsilon_a - \frac{r\cos\varphi}{R})\right)^2 + cos^2\theta\left(1+\nu(\varepsilon_a - \frac{r\cos\varphi}{R})\right)^2}\right) \tag{3}$$

$$\varphi = \frac{z}{r\cdot\tan\theta} + \alpha(z) \tag{4}$$

$$\varepsilon = K\left(1 - \sqrt{sin^2\theta\left(1-\nu\frac{d}{r}\cos 2\varphi\right)^2 + cos^2\theta\left(1+\frac{d}{r}\cos 2\,\varphi\right)^2}\right) \tag{5}$$

Where ε_a is the casing axial strain (compression is noted positive); ν is the Poisson's ratio of the casing material; *K* is the bonding factor between the casing and cable, which represents how well the casing strain is reflected on strain sensors; ε_t is the casing tangential strain; *r* is the radius of the casing; *R* is the bending radius; $\varphi$is the azimuth angle of the sensor on the casing, which can be expressed as a function of the cable length along the casing z and bending orientation $\alpha(z)$ (Equation 4); *d* is the radial deflection in the major or minor axis of the ellipse (radial deflections are assumed the same in both directions for small ovalization deformation).

The representative sensor strain curves for axial compression, bending, and ovalization were presented by Pearce et al.[24] (Figure 4), where zero degree in phasing starts from the outer side of the casing in bending, and from the major axis of the ellipse in ovalization.

The appropriate wrapping angle is affected by the sensor size and pipe diameter. A larger sensor length would result in a larger wrapping angle and thus lower spatial resolution, and on contrary, a larger pipe diameter would be able to accommodate more sensors and smaller wrapping angle, which means higher spatial resolution. Different wrapping angles, sensor size and number of sensors are used for different deformation modes and pipe sizes (Table 1).

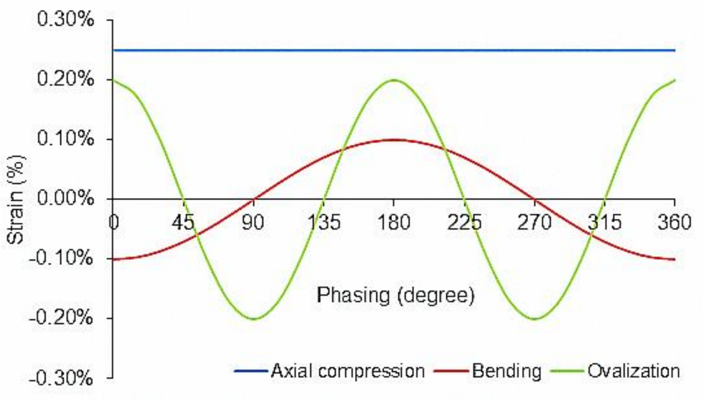

Figure 4. Representative curve of the sensor strain for different deformation modes.

Table 1. Wrapping angle, sensor size and number of sensors for each deformation mode.

Deformation Mode	**Pipe OD (inch)**	**Sensor Length (inch)**	**Sensor Number (per wrap)**	**Wrapping Angle (degree)**
Axial Compression	4.5 (PVC)	4	3	23
Radial Expansion	4.5 (PVC, LVDT) 4.5 (PVC, SG)	4 3	3 5	23 35
Bending	4 (PVC) 6 (Steel)	3 3	8 17	55 35
Ovalization	6 (PVC) 6 (Steel)	3 3	8 8	35 35

Experimental setup and procedure

A number of evenly distributed CCFPI strain sensors are fabricated according to desired length. The cable trajectory is marked on the pipe based on the pre-determined wrapping angle. A load of around 200 newton is applied on the cable (Figure 5 (a)) to pre-stress the sensor to its linear range. A high strength epoxy is used to attach the cable to the pipe.

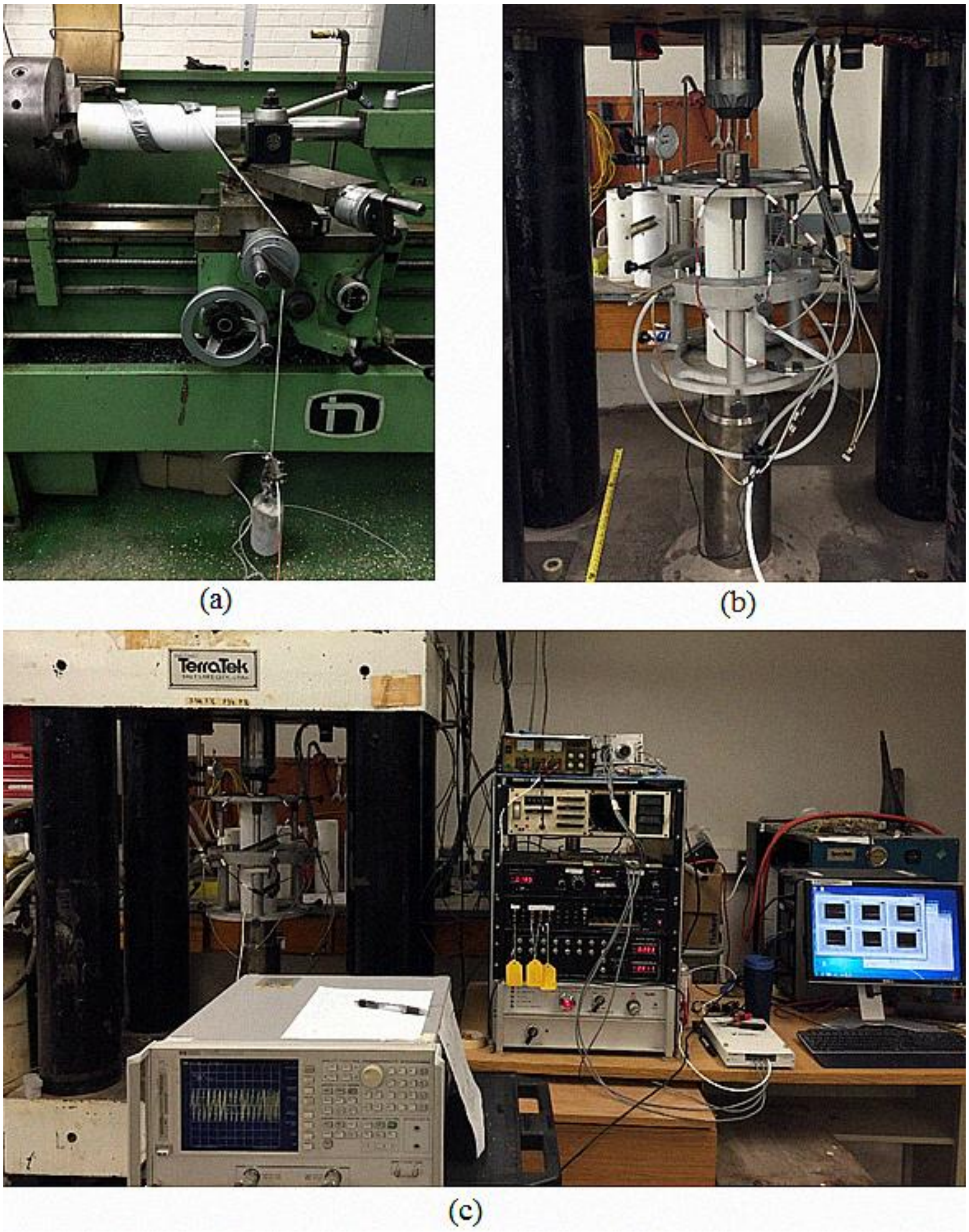

(a) (b)

(c)

Figure 5. Pipe preparation and experimental setup for the PVC pipe unconfined uniaxial compression test.

Axial compression test.

An 8 inch long PVC sewer pipe with an OD of 4.5 inch and wall thickness of 0.25 inch is used for the axial compression test. Three CCFPI strain sensors with a length of 4 inch are attached to the pipe at a 23° wrapping angle. Three vertical LVDTs are used to measure the actual pipe deformation in axial direction (Figure 5 (b)) in comparison to the casing imager measured pipe deformation. The PVC pipe is placed in a loading frame for an unconfined uniaxial compression test (Figure 5 (c)). Both the LVDTs and coaxial cable strain sensors are recorded every 10 seconds for comparison. The pipe axial strain is increased about every 0.1% up until 1% and at each step the load is held constant for 3 minutes.

Radial expansion test.

The same experimental setup is used for the radial expansion test, except the three vertical LVDTs are replaced by three horizontal LVDTs to measure the actual pipe radial deformation (Figure 5 (b)). Three vacuum cups and a vacuum pump are used to hold the middle ring (where the three horizontal LVDTs are mounted) in place to make sure that the radial deformation is always measured from the middle of the pipe. A leveler is used to make sure the rings are level.

To measure the actual pipe radial deformation from different sections of the pipe, a modified experimental setup is designed with strain gauges (SG) (Figure 6 (a)). Five CCFPI strain sensors are deployed at a 35° wrapping angle, and a temperature-compensated bridge circuit with strain gauges and resistors is designed to measure the average pipe radial deformation from the top and bottom (Figure 6 (b)). The gauge measured strain can be calculated as,

$$\varepsilon = -\frac{\Delta U/10G}{10+\Delta U/10G} \tag{6}$$

Where ε is gauge measured strain; ΔU is voltage difference between OP_1 and OP_2; G is gauge factor.

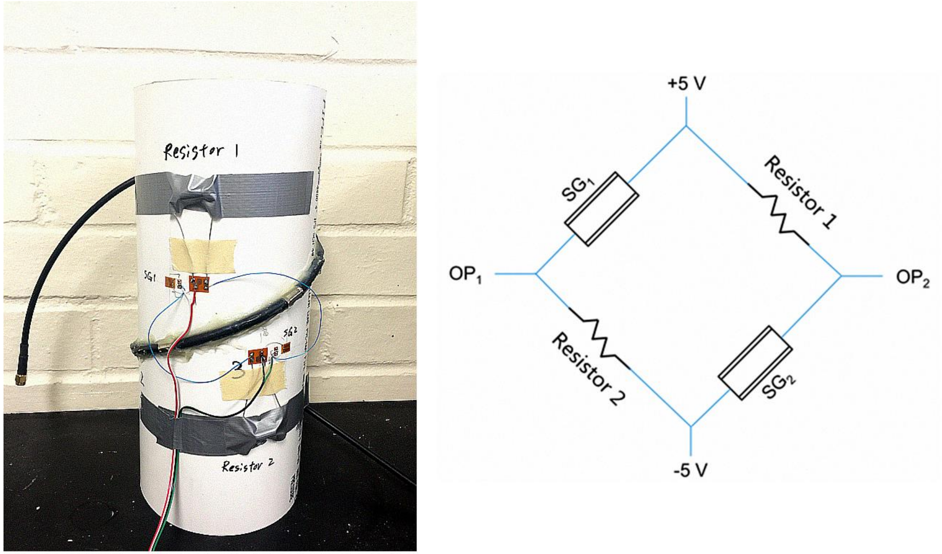

(a) (b)

Figure 6. Picture and schematic of strain gauge deployment for PVC pipe radial expansion test.

Bending test.

A 5 foot long PVC sewer pipe with an OD of 4 inch and wall thickness of 0.1 inch is placed on a bench with flat surface for the bending test. Eight CCFPI strain sensors with a length of 3 inch are attached to the middle section of the pipe at a 55° wrapping angle. Half rounds with six different sizes (Table 2) are used to rise up the ends of the pipe, and a V block load is placed in the middle to bend the pipe until the pipe bottom touches the bench top surface (Figure 7 and Figure 8). Two steel round disks are inserted into the pipe to prevent the occurrence of ovalization when the pipe is bent. Assuming a uniform bending angle along the whole length of the pipe, the theoretical bending radius of the pipe R is expressed as,

$$R = \frac{L^2}{8b} - \frac{OD}{2} - \frac{b}{2} \tag{7}$$

where L is the length of the pipe, b is the radius of the half round, and OD is the outer diameter of the pipe. The theoretical bending radius and half bending angle *α/2* for the six different sizes of half round is included in Table 2.

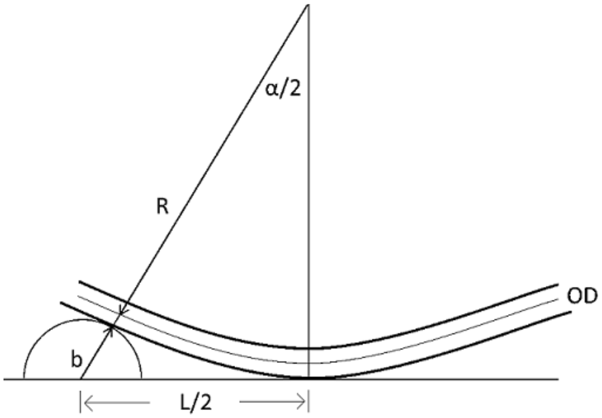

Figure 7. Schematic of pipe bending test.

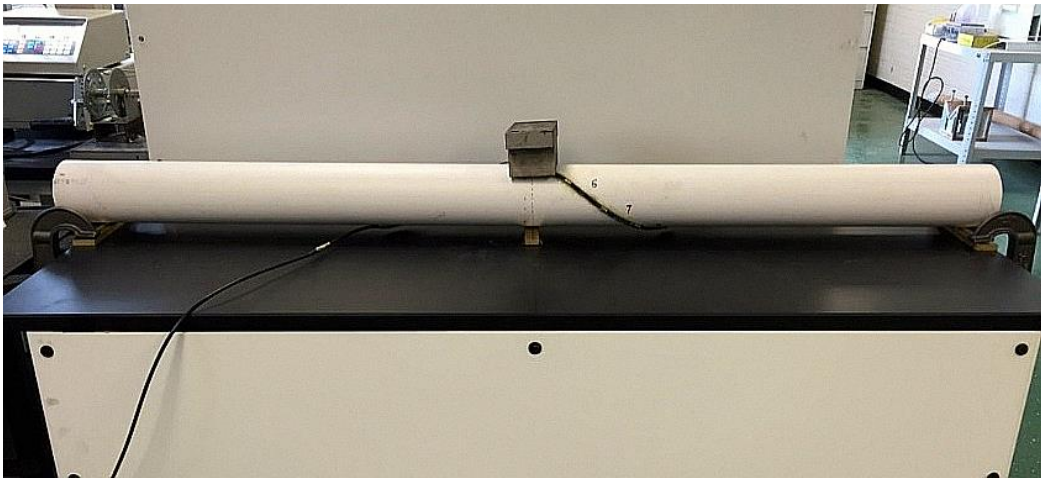

Figure 8. Picture of the PVC pipe bending test.

Table 2. Theoretical bending radius and half bending angle for different half round size.

Half Round Diameter (inch)	Bending Radius (inch)	Half Bending Angle (degree)
0.25	3434.38	0.4887
0.375	2288.84	0.7330
0.5	1716.05	0.9774
0.625	1372.36	1.2217
0.75	1143.28	1.4660
1	856.79	1.9546

To simulate the system performance on real casing, a 5 foot long steel pipe with an OD of 6 inch and wall thickness of 0.083 inch is also used for the bending test (Figure 9). Half rounds of 0.25 inch in diameter are used, and the pipe is placed in the loading frame to be bent. 17 strain sensors and a 35° wrapping angle are used for this test.

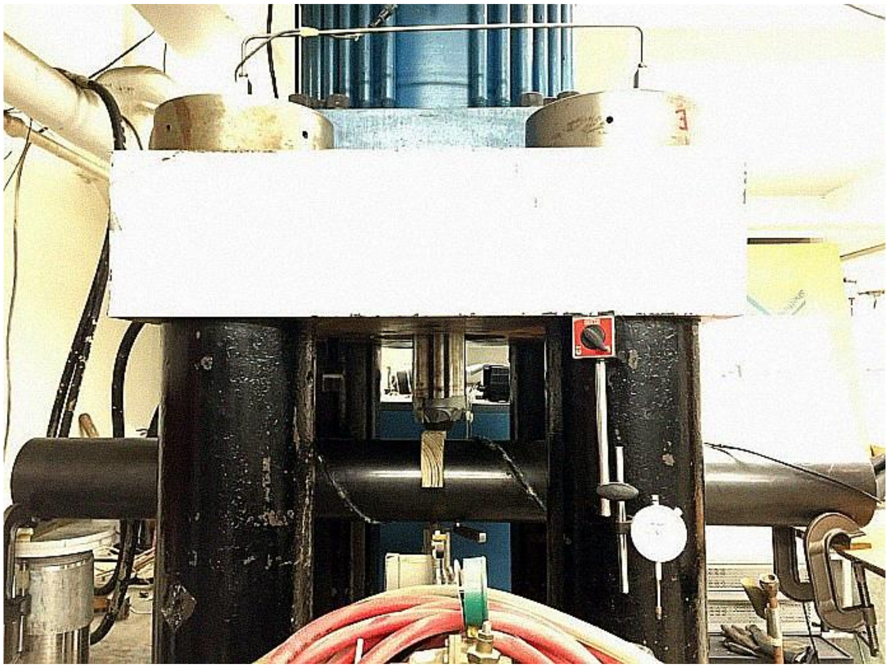

Figure 9. Picture of the steel pipe bending test.

Ovalization test.

A 15 inch long PVC sewer pipe with an OD of 6 inch and wall thickness of 0.2 inch is used for the ovalization test. Eight CCFPI strain sensors with a length of 3 inch are attached to the pipe at a 35° wrapping angle. A scissor jack with two steel half rounds welded to the top and bottom is placed inside the pipe to stretch it to different ovalities (Ovality = (Max OD – Min OD)/Nominal OD). Three LVDTs are used to measure the actual pipe deformation in the major and minor axis directions of the ellipse (Figure 10). To simulate the system performance on real casing, the same test is conducted on a 15 inch long steel pipe with an OD of 6 inch and wall thickness of 0.083 inch with the same number of sensors and wrapping angle.

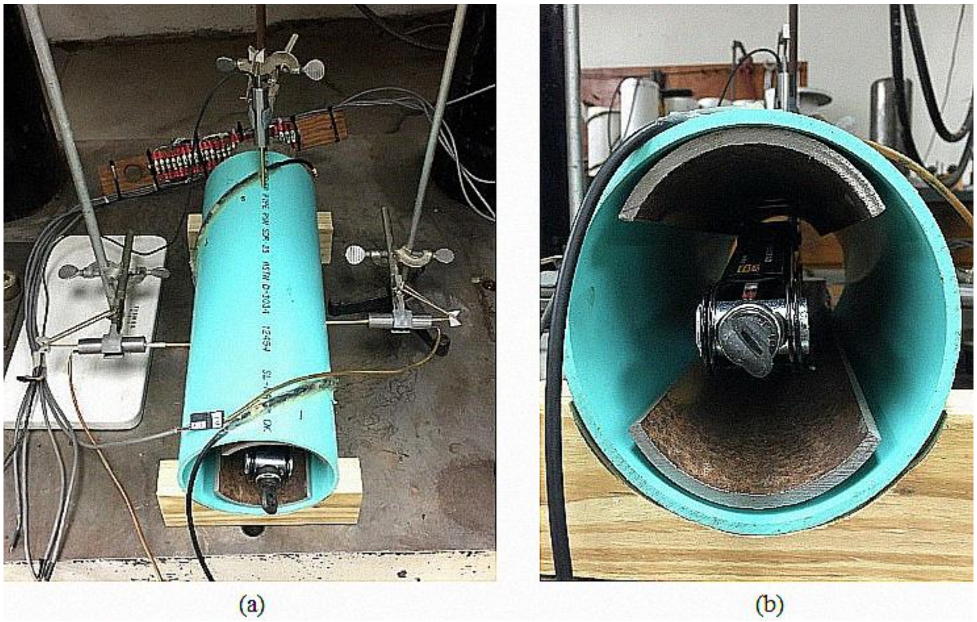

Figure 10. Picture of the ovalization test.

Results

Axial compression test.

Figure 11 shows the comparison between LVDT and casing imager measured pipe axial strain when assuming a bonding factor of 1 (casing strain is fully reflected on the strain sensors). The LVDT measured pipe axial deformation is the average of the three vertical LVDT measurements, and the sensor measured pipe axial deformation is the average of the three sensor measurements calculated based on Equation 1. The two data series almost overlie on each other, indicating that for a pipe axial strain up to 1%, the casing imager is measuring the true pipe axial deformation in real-time. It proves the real-time monitoring capability of the system in casing axial compression. However, it also shows that as the stress was released, the casing imager measured pipe axial strain didn’t go back to 0%, but went negative, which is possibly due to the undermined epoxy strength during the compression and thus changed bonding factor.

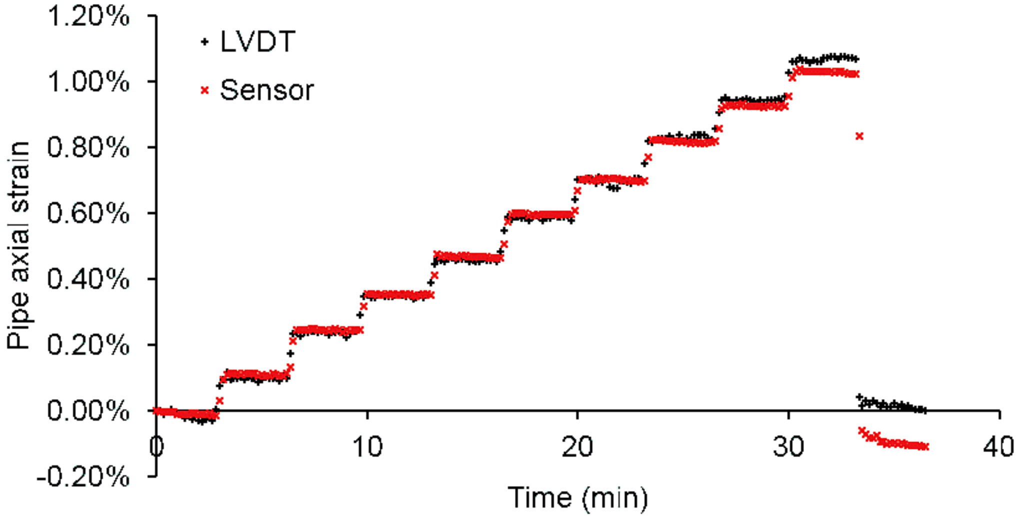

Figure 11. LVDT vs. casing imager measured PVC pipe axial strain.

To study the measurement accuracy of the system at different measurement ranges, the measurement error is defined as (LVDT measurement-casing imager measurement) / (LVDT measurement). Figure 12 is the measurement error for each individual data point, and Figure 13 is the average measurement error for different ranges. As the figures indicate, the measurement error is extremely large (above 30%) when the pipe axial strain is below 0.1%, but the error is reduced greatly when the pipe is under larger strain. For pipe strain above 0.3%, the measurement error is only 1.79% full scale. The smaller measurement error at larger pipe axial strain suggests that the casing imager is best suited for measuring casing axial strain larger than 0.3%.

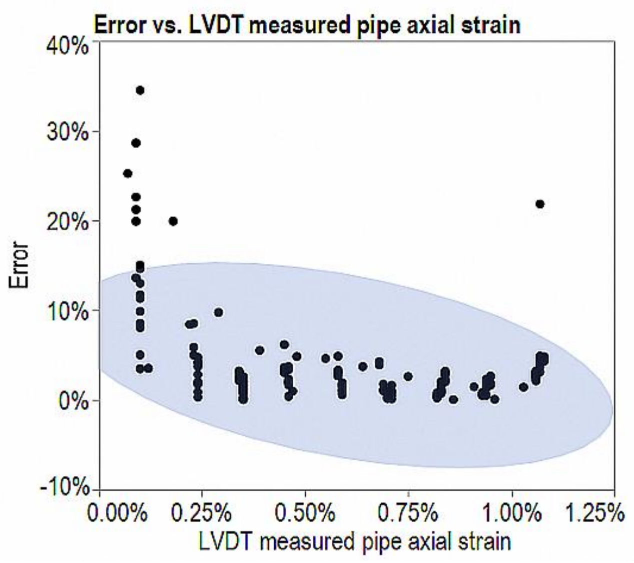

Figure 12. Measurement error vs. LVDT measured pipe axial strain.

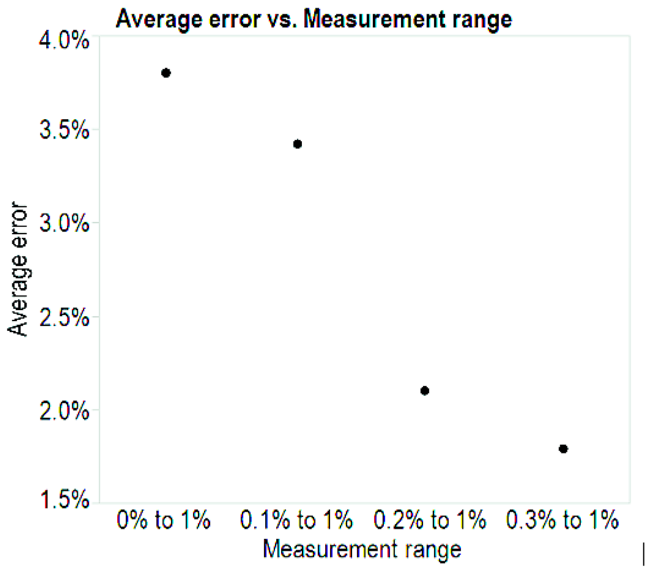

Figure 13. Average error vs. measurement range.

Radial expansion test.

Figure 14 shows the comparison between LVDT and casing imager measured pipe radial deformation when assuming a bonding factor of 1. The LVDT measured pipe radial deformation is the average of the three horizontal LVDT measurements, and the sensor measured pipe radial deformation is calculated for each of the three sensors based on Equation 2. As indicated in the figure, the three strain sensors measured different pipe radial deformation, which suggests that the radial expansion is not uniform along the whole length of the pipe when the pipe is compressed. Similar results could be observed in the modified test with strain gauges (Figure 15). All five strain sensors exhibit different strain measurements.

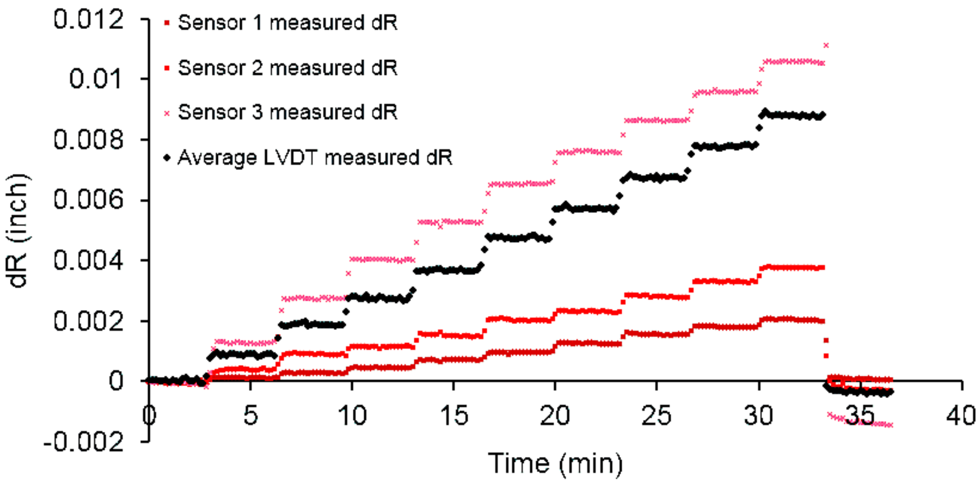

Figure 14. LVDT vs. casing imager measured PVC pipe radial deformation.

Despite the different measurements of the strain sensors, the average of the three strain sensor measurements shows a simultaneous response to the pipe deformation at each test increment (Figure 16). The measurement difference between strain sensor and LVDT gets larger as the pipe deformation increases, indicating the non-uniformity in radial deformation gets larger.

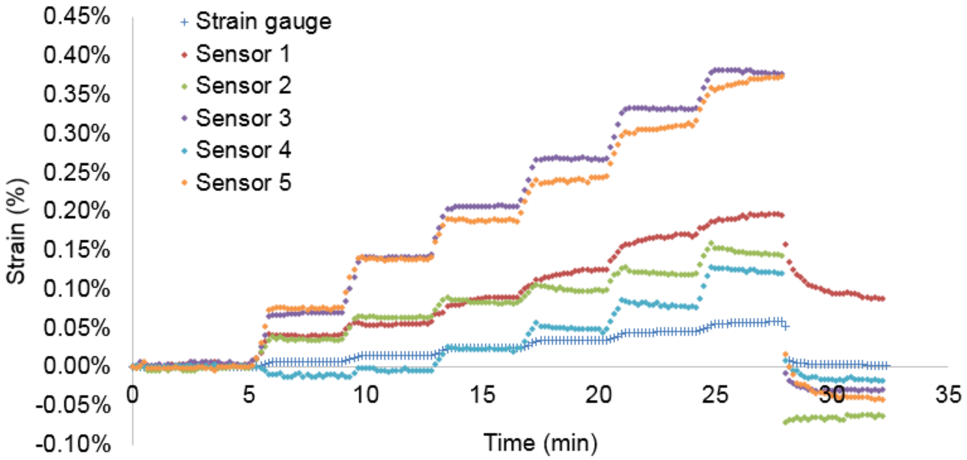

Figure 15. Strain gauge vs. casing imager measured PVC pipe radial deformation.

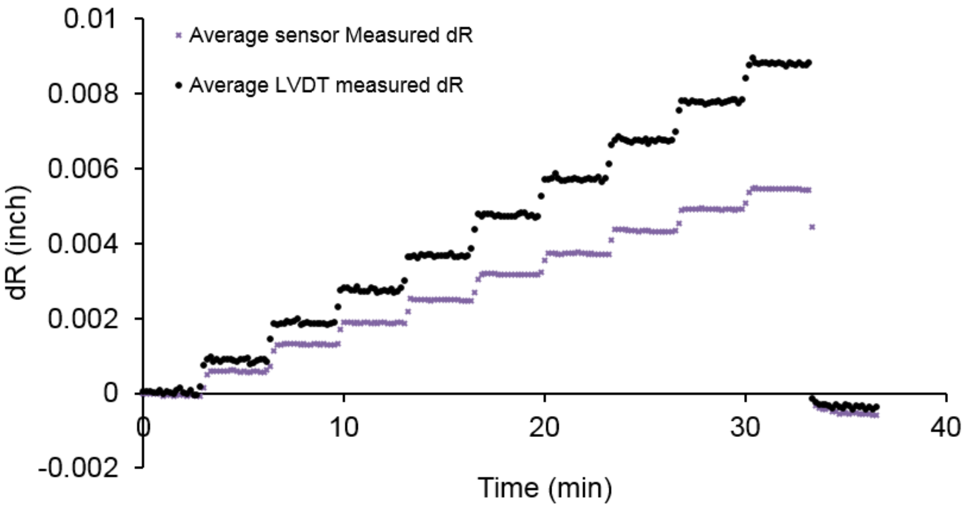

Figure 16. Average LVDT vs. average casing imager measured PVC pipe radial deformation.

Bending test.

Figure 17 (a)-(f) shows the sensor measured strain compared to the representative curve of the PVC pipe bending test for the six different bending angles when assuming a bonding factor of 1. The representative curve is acquired based on the theoretical bending radius from Equation 7 and the sensor strain—bending radius correlation found in Equation 3. Although some of the sensor measurements are out of phase on the plots, especially for the one indicated by a red arrow, it doesn’t affect the general pattern of the data points, where the sensor measurements are distributed evenly on two sides of the representative curve.

After fitting a cosine curve to the sensor measurements with a Matlab® fit curve function, the sensor measured half bending angle can be calculated based on Equation 3. Figure 18 shows the comparison between the sensor measured half bending angle and the theoretical half bending angle. It is indicated that the measurement error is below 0.1 degree when the pipe half bending angle is below 1.5 degrees. The high measurement accuracy shows that the casing imager measurement accuracy is not affected by a singled extremely out-of-phase data point, because the measured bending angle is represented by a cosine curved fitted to a scattered plot.

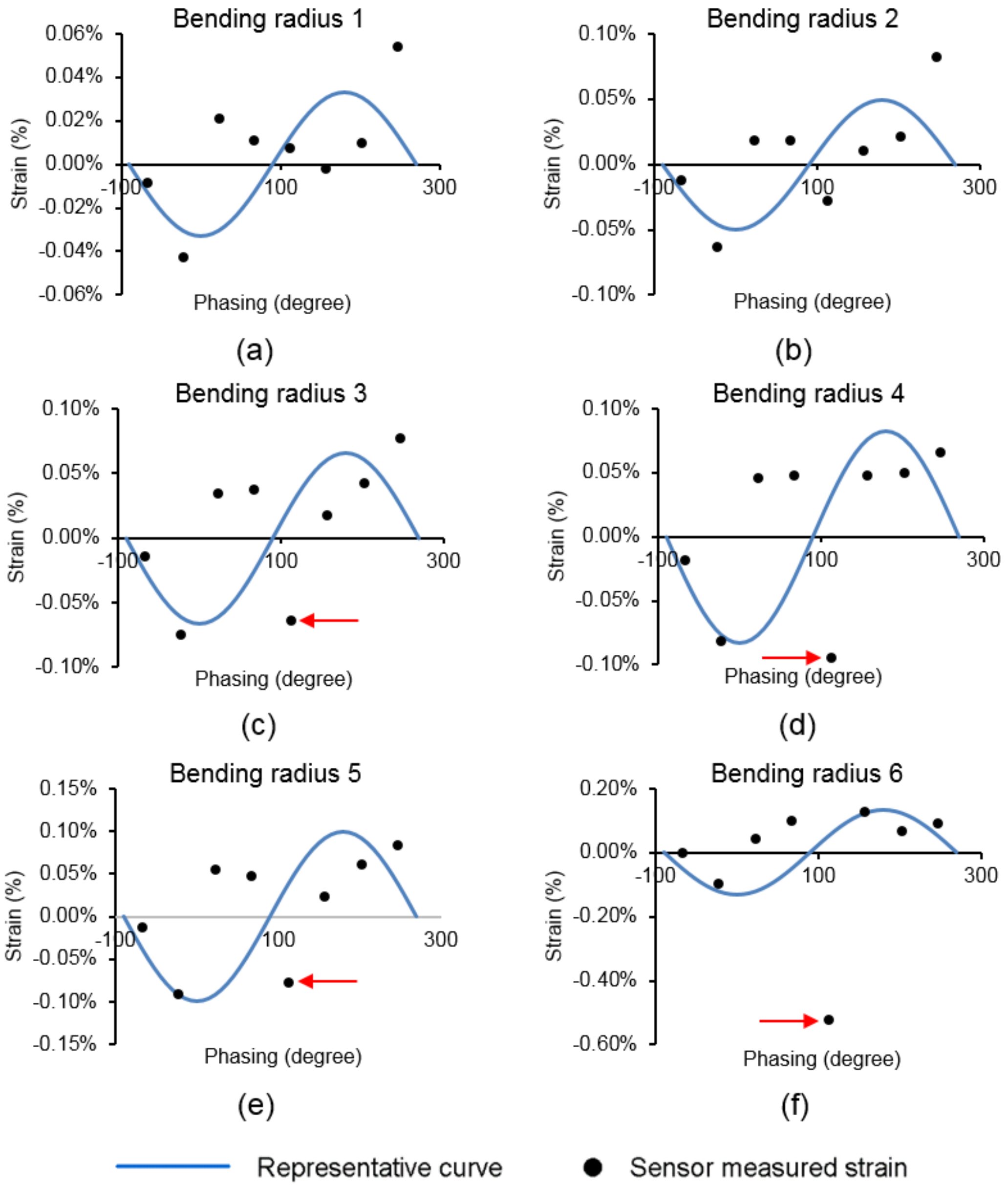

Figure 17. Sensor measured strain vs. representative curve for PVC pipe bending test.

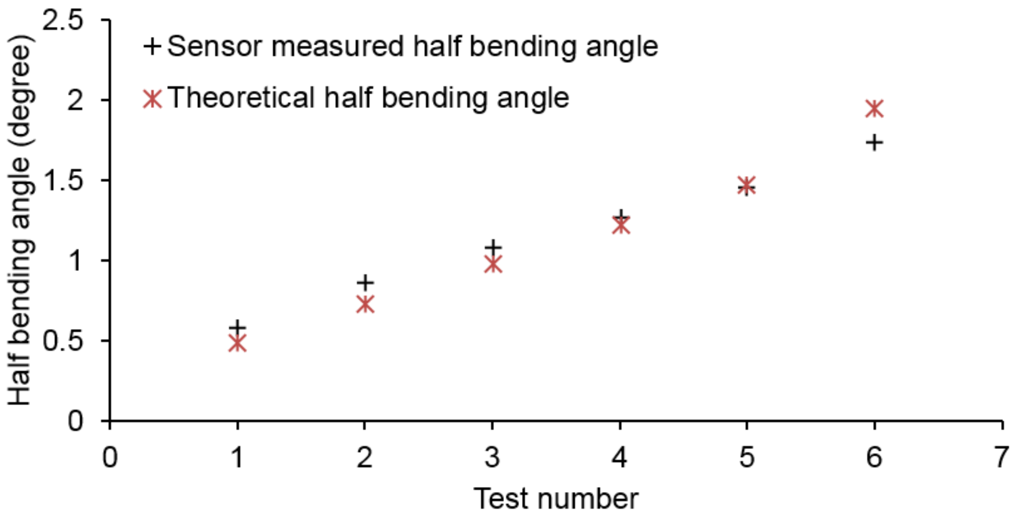

Figure 18. Sensor measured half bending angle vs. theoretical half bending angle for PVC pipe bending test.

To study the effect of bonding factor on the bending measurement accuracy, a bonding factor of 1 and 0.5 are assumed respectively in the steel pipe bending test, and the sensor measurements are compared to the representative curve accordingly in Figure 19 (a) and (b). As can be observed, the match between the sensor measurements and the representative curve is better when assuming a bonding factor of 0.5. And when the half bending angle is calculated based on each individual sensor measurement (Figure 20), the data points are more closely distributed on two sides of the theoretical half bending angle when a bonding factor of 0.5 is assumed. The results suggest that in this specific test, a bonding factor of 0.5 enables the casing imager to have a more accurate measurement in bending angle measurement.

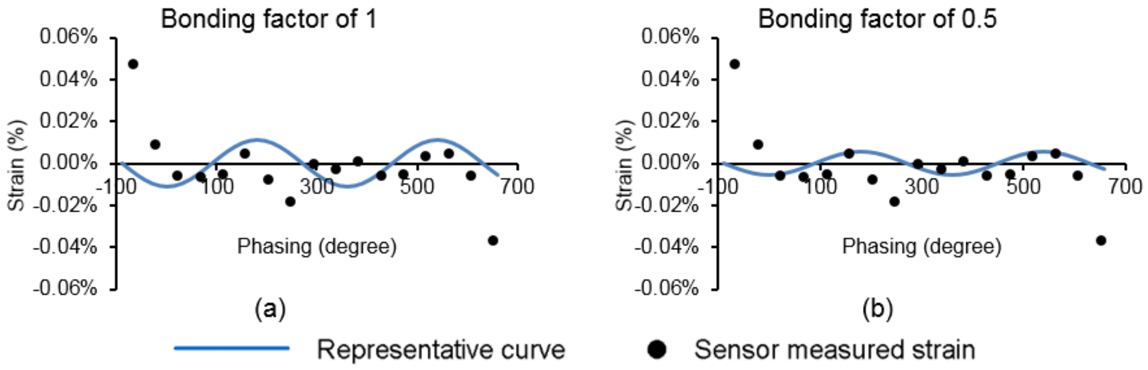

Figure 19. Sensor measured strain vs. representative curve for steel pipe bending test.

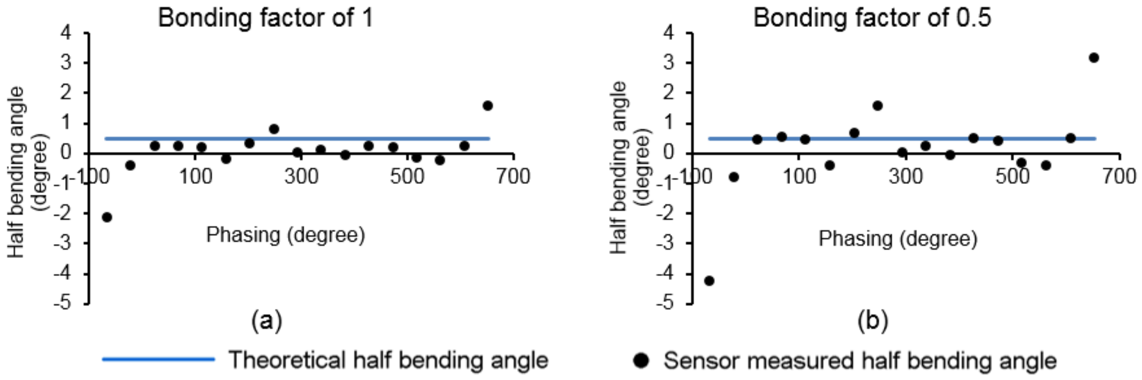

Figure 20. Sensor measured half bending angle vs. theoretical half bending angle for steel pipe bending test when assuming different bonding factors.

Ovalization test.

The comparison between sensor measurements and the representative curve of the PVC pipe ovalization test is plotted in Figure 21 for four ovalities (Table 3). The representative curve is acquired based on the three LVDT measurements and Equation 5. Compared to the representative curve, the sensor measurements distribute evenly on two sides of the curve, but the magnitude is much smaller, which means the system is not very responsive to the deformation.

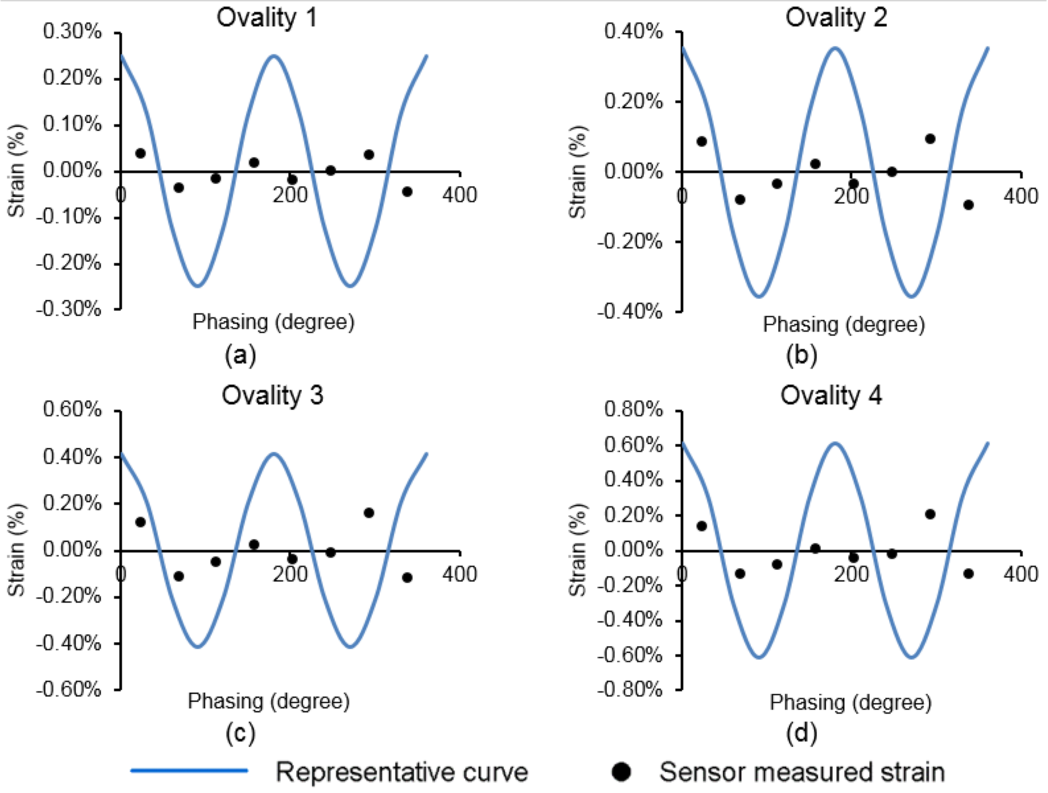

Figure 21. Sensor measured strain vs. representative curve for PVC pipe ovalization test.

One possible reason could be the sensor size limit. To maintain a high sensor strain resolution, a sensor length of 3 inch is used in the test, which results in only eight sensors deployed per 360° helical wrap. Each sensor has a spatial resolution of 45° azimuth angle, resulting in the reduction of the system sensitivity.

Another possible cause could be the original pipe roundness. A measurement of the pipe OD shows that the pipe used in the test has an OD tolerance of 0.07 inch, which is equivalent to 1.19% in ovality, while the maximum ovality measured by the LVDTs in the test is only 3.15% (Table 3). Compared to the largest pipe ovality tested, the original pipe ovality is extremely large, which could cause the offset of the sensor strain curve.

Table 3. LVDT measured pipe ovality for PVC and steel pipe ovalization test.

Test Number	PVC Pipe	Steel Pipe
Ovality 1	0.81%	0.41%
Ovality 2	1.65%	0.94%
Ovality 3	2.34%	1.14%
Ovality 4	3.15%	1.66%

To investigate the effect of the original pipe roundness on the casing imager performance in ovalization deformation measurement, the same test is conducted on a steel pipe which has a smaller OD tolerance (0.02 inch as opposed to 0.07 inch). The comparison between sensor measurements and the representative curve (Figure 22) for four ovalities (Table 3) still shows that the casing imager is not sensitive to the pipe ovalization deformation. As a matter of fact, it is not even as good as the PVC pipe test, which is possibly due to the reduced bonding factor on the steel pipe as in the steel pipe bending test. The results lead to the conclusion that the primary limitation of the system in ovalization deformation measurement lies in the sensor length. A small sensor size is desired in order to enhance the spatial resolution of the system and thus the sensitivity in ovalization deformation measurement.

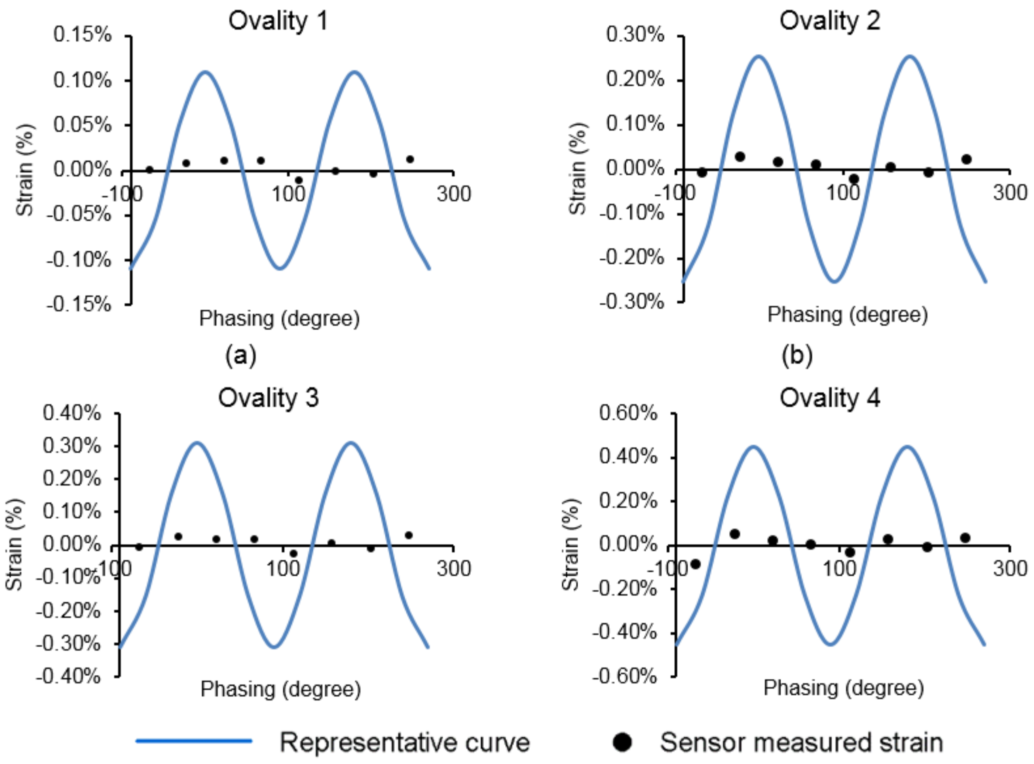

Figure 22. Sensor measured strain vs. representative curve for steel pipe ovalization test.

Discussion

The higher measurement error at low pipe axial strain (Figure 12&13) is likely caused by the insufficient pre-stress applied on the sensor, so that the sensors were not in their linear range. A higher load is required to fully stress the sensors so that to achieve a more accurate measurement at lower pipe axial strain range.

The pipe radial deformation generated during the pipe compression is not uniform along the whole length of the pipe (Figure 14&15). The test setup needs to be improved to be able to generate uniform radial deformation on the pipe to characterize the casing imager performance in radial expansion deformation.

The original pipe straightness and occurrence of ovalization along with bending could be an effect on the pipe bending measurement accuracy. The PVC sewer pipe is bent during the manufacture and shipping process, which means the pipe is not bent from an initial straight state, while both the theoretical and sensor measured bending angle are calculated assuming an initial straight pipe. And the occurrence of ovalization along with bending will cause the shift of the curve. In addition, assuming a uniform bending angle along the whole length of the pipe may not be realistic. Since the pipe is only 5 foot long and a single point load is applied at the center, symmetric but variant bending angles along the pipe would be anticipated.

The casing imager has limited capability in ovalization deformation monitoring. In addition to the effect of pipe original roundness, the sensor size also limits the system performance. To maintain a good strain resolution, the current technology would only allow a sensor size no smaller than 2 inch, which means only eight sensors could be deployed per helical wrapping.

The bonding factor of the system needs to be carefully evaluated before field application. Different cable materials, casing materials, and epoxy properties could change the system bonding factor, and thus the final measurement accuracy. Also, the bonding factor could change along with time and casing deformation (Figure 11). When the casing is deformed, the epoxy strength is degraded so the bonding factor between the cable and the pipe will be changed. A changing bonding factor should be taken into consideration when the system is in field application.

Overall, the coaxial cable casing imaging system has been proved to be able to measure various casing deformation modes in real-time, including axial compression, radial expansion, bending, and ovalization. Compared to the previous test on the SureView^{TM} RTCM system[23], the coaxial cable casing imaging system has an improved measurement accuracy in each of the deformation modes.

In addition, the coaxial cable sensors are free of the threat of hydrogen darkening, which could be fatal to fiber-optic sensors however. The temperature and pressure rating of the coaxial cable sensors (110 °C and 1,000 psi) would allow a downhole deployment of 2,500 ft[29], and coaxial cables that use ceramic, silica or other high temperature tolerant dielectrics could survive pressures of 10,000 psi and temperatures of 1,000 °C[30], promising the technology to be applicable for deeper downhole deployment.

More importantly, with the low cost and high robustness, the coaxial cable imaging system has the full potential to serve as a solution to long-term wellbore integrity monitoring. When the casing deformation is analyzed in numerical simulations and associated with the wellbore integrity state and the corresponding leakage risk, the real-time casing deformation monitoring ability of the system would enable the real-time visualization of the wellbore leakage risk. Continuous work on the minimization of the temperature crosstalk would greatly enhance the sensor measurement accuracy, and the development of filters in data analysis would enable the measurement of a mixed deformation mode of the casing, such as casing buckling, which would prove great value in resolving reservoir compaction and surface subsidence related wellbore integrity problems.

Conclusions

A real-time coaxial cable casing imaging system has been developed and evaluated in laboratory for casing deformation monitoring in CO_2 sequestration wellbore integrity analysis. This system enables continuous visualization of casing deformation with high sensitivity, accuracy, and spatial resolution without requiring entry into the casing. The laboratory experiment of the system prototype deployed on PVC sewer pipe and steel pipe demonstrated the system's ability of real-time monitoring of casing axial compression, radial expansion, bending, and ovalization. This system would prove great value in real-time monitoring of casing deformation and provide insight into potential wellbore leakage that may contaminate the ground water. And the low cost and high robustness of the distributed coaxial cable sensors will greatly lower the downhole monitoring cost and increase the system longevity.

Acknowledgements

This material is based upon work supported by the Department of Energy under Award Number DE-FE0009843. The authors would like to thank the research engineering technicians Jeffrey Heniff and John Tyler from the Rock Mechanics and Explosives Research Center of Missouri University of Science and Technology for the help on the experimental setup.

References

1. Bacon DH. Reduced-Order Model for the Geochemical Impacts of Carbon Dioxide, Brine and Trace Metal Leakage into an Unconfined, Oxidizing Carbonate Aquifer, Version 2.1. Pacific Northwest National Laboratory (PNNL), Richland, WA (US); 2013 Mar 31.

2. Little MG, Jackson RB. Potential impacts of leakage from deep CO2 geosequestration on overlying freshwater aquifers. *Environmental science & technology*. 2010 Oct 26; 44(23):9225-32.

3. Smith KL, Steven MD, Jones DG, West JM, Coombs P, Green KA, Barlow TS, Breward N, Gwosdz S, Krüger M, Beaubien SE. Environmental impacts of CO2 leakage: recent results from the ASGARD facility, UK. *Energy Procedia*. 2013 Dec 31; 37:791-9.

4. Pearce JM, West JM. Study of potential impacts of leaks from onshore CO2 storage projects on terrestrial ecosystems. IEA Greenhouse Gas R&D Programme Technical Study. 2007; 3.

5. Harvey OR, Cantrell KJ, Qafoku NP, Brown CF. Geochemical Implications of CO2 Leakage Associated with Geologic Storage: A Review. Report prepared for the US Department of Energy under Contract DE-AC05-76RL01830. 2012 Jul 9.

6. Cook P. Geologically storing carbon: Learning from the Otway Project experience. CSIRO PUBLISHING; 2014 Aug 18.

7. Edlmann K, Bensabat J, Niemi A, Haszeldine RS, McDermott CI. Lessons learned from using expert elicitation to identify, assess and rank the potential leakage scenarios at the Heletz pilot CO2 injection site. *International Journal of Greenhouse Gas Control*. 2016 Jun 30; 49:473-87.

8. Metz B, editor. Carbon dioxide capture and storage: special report of the intergovernmental panel on climate change. Cambridge University Press; 2005 Dec 19.

9. Moreno FJ, Chalaturnyk R, Jimenez J. Methodology for assessing integrity of bounding seals (Wells and Caprock) for geological storage of CO2. In Proceedings of the 7. International Conference on Greenhouse Gas Control Technologies 2005.

10. Weideman B, Nygaard R. How cement operations affect your cement sheath short and long term integrity. In American Association of Drilling Engineers Fluids Technical Conference and Exhibition 2014.

11. Jenkins C, Chadwick A, Hovorka SD. The state of the art in monitoring and verification—ten years on. *International Journal of Greenhouse Gas Control*. 2015 Sep 30; 40:312-49.

12. Benson SM, Gasperikova E, Hoversten GM. Monitoring protocols and life-cycle costs for geologic storage of carbon dioxide. In Proceedings of the 7th International Conference on Greenhouse Gas Control Technologies (GHGT-7) 2004 Sep 5 (pp. 1259-1266).

13. Nygaard R, Lavoie R. Project cost estimate-Wabamun area CO2 sequestration project (WASP). University of Calgary. 2009.

14. Rubin ES, Davison JE, Herzog HJ. The cost of CO2 capture and storage. *International Journal of Greenhouse Gas Control*. 2015; 40: 378-400.

15. May F, Waldmann S. Tasks and challenges of geochemical monitoring. *Greenhouse Gases: Science and Technology*. 2014 Apr 1; 4(2):176-90.

16. Holley EH, Zimmer U, Mayerhofer MJ, Samson E. Integrated analysis combining microseismic mapping and fiber-optic distributed temperature sensing (dts). In Canadian Unconventional Resources and International Petroleum Conference 2010 Jan 1. Society of Petroleum Engineers.

17. Cairns G, Jakubowicz H, Lonergan L, Muggeridge A. Issues regarding the use of time-lapse seismic surveys to monitor CO2 sequestration. In SEG Technical Program Expanded Abstracts 2010 Jan 1 (pp. 1236-1240).

18. Yang C, Hovorka SD, Young MH, Trevino R. Geochemical sensitivity to CO2 leakage: detection in potable aquifers at carbon sequestration sites. *Greenhouse Gases: Science and Technology*. 2014 Jun 1; 4(3):384-99.

19. Koelman JV, Lopez JL, Potters H. Fiber optic technology for reservoir surveillance. In International Petroleum Technology Conference 2011 Jan 1. International Petroleum Technology Conference.

20. Williams GR, Brown G, Hawthorne W, Hartog AH, Waite PC. Distributed temperature sensing (DTS) to characterize the performance of producing oil wells. In Environmental and Industrial Sensing 2000 Dec 29 (pp. 39-54). International Society for Optics and Photonics.

21. Baker Hughes Incorporated. SureView real-time fiber-optic compaction monitoring system [Internet]. 2010 [cited 2013 July 11]. Available from http://c14503045.r45.cf2.rackcdn.com/v1/6d9595dc1c7754cdc039ba0ad7cd32e5/30643-real-time-fiber-optic-casing-imaging-system_brochure-0910.pdf

22. Baker Hughes Incorporated. Optical reality: fiber-optic technology monitors sand screen deformation in real time. *Connexus.* 2010; *1*(1), 20-23.

23. Pearce J, Legrand P, Dominique T, Childers B, Rambow F, Dria D. Real-time compaction monitoring with fiber-optic distributed strain sensing (DSS). In SPWLA 50th Annual Logging Symposium 2009 Jan 1. Society of Petrophysicists and Well-Log Analysts.

24. Pearce J, Rambow F, de Jongh H, Dria D, Hall T, Stoesz C, Childers B, Dominique T. Applications And Deployments Of The Real-Time Compaction Monitoring System. In SPWLA 51st Annual Logging Symposium 2010 Jun 19. Society of Petrophysicists and Well-Log Analysts.

25. Rambow FH, Dria DE, Childers BA, Appel M, Freeman JJ, Shuck M, Poland SH, Dominique T. Real-Time Fiber-Optic Casing Imager. *SPE Journal*. 2010 Dec 1; 15(04):1-089.

26. Huang J, Wang T, Hua L, Fan J, Xiao H, Luo M. A coaxial cable Fabry-Perot interferometer for sensing applications. *Sensors*. 2013 Nov 7; 13(11):15252-60.

27. Huang J, Wei T, Lan X, Fan J, Xiao H. Coaxial cable Bragg grating sensors for large strain measurement with high accuracy. In SPIE Smart Structures and Materials+ Nondestructive Evaluation and Health Monitoring 2012 Apr 26 (pp. 83452Z-83452Z). International Society for Optics and Photonics.

28. Wei T, Wu S, Huang J, Xiao H, Fan J. Coaxial cable Bragg grating. *Applied Physics Letters*. 2011 Sep 12; 99(11):113517.

29. Li Y, Zhu W, Cheng B, Nygaard R, Xiao H. Laboratory evaluation of distributed coaxial cable temperature sensors for application in CO2 sequestration well characterization. *Greenhouse Gases: Science and Technology*. 2016 Jul 1.

30. Thermocoax Incorporated. Mineral insulated signal transmission cable [Internet]. 2012 [cited 2013 May 10]. Available from http://www.thermocoax-nuclear.com/nuclear---transmission-cable-application.html

III. FEASIBILITY OF REAL-TIME EVALUATION OF THE CO2 SEQUESTRATION WELLBORE INTEGRITY WITH THE COAXIAL CABLE CASING IMAGER

Yurong Li[1], Runar Nygaard[2]
[1]Missouri University of Science and Technology, [2]Oklahoma State University

Abstract: To avoid and minimize the environmental impact of CO_2 leakage into groundwater and surface, evaluating and maintaining the wellbore integrity is of great significance throughout the CO_2 sequestration project. An innovative coaxial cable casing imager has been developed and proposed as a solution to real-time wellbore integrity monitoring in CO_2 sequestration. To study the feasibility of using the proposed system for wellbore integrity monitoring, a staged finite element model is established and analyzed in this paper.

The staged finite element model is based on a well in the Weyburn field. The casing strain caused by CO_2 injection is analyzed for both the surface casing and the production casing to study the appropriate installation depth of the system. A sensitivity study is conducted on the in-situ stress regime, interface bonding condition, cement shrinkage, injection temperature, and operation time of year. The radial and hoop stress change across the casing, cement, and formation composite is studied to investigate the cement failure risk under various conditions. The gap distance between the casing-cement and cement-formation interface is analyzed as indication of the interface leakage risk.

The result of the simulation shows that the production casing is at greater risk, thus the system is more beneficial if installed on the production casing. The casing strain in all simulations is below the system's optimum performance range, the system needs to be

improved to have more accurate measurement at smaller casing strain, or the wrapping angle of the sensors needs to be reduced to increase the system's sensitivity.

Keywords: CO_2 Sequestration; Wellbore Integrity Monitoring; Coaxial Cable Casing Imager; Staged Finite Element Analysis

Introduction

Evaluating and maintaining the wellbore integrity is required before, during, and after the CO_2 injection process in a geologic CO_2 sequestration project. CO_2 leakage can cause severe environmental issues, such as groundwater contamination, plant stress, and biomass change[1-5]. However, wellbore leakage is a reoccurring problem for cased wells[6], and leakage paths can occur both due to events and conditions during the primary cementing job and after the primary cementing is completed[7]. Although remediation job can be conducted, it cannot always fix the problem, and sometimes the remedial cementing operation runs the risk of equipment damage, blowout, or spill[8].

Destructive and non-destructive tools have been used extensively to investigate the integrity of the casing, the cement, the casing-cement and cement-formation interface[9]. Non-destructive tools (logging tools) include multifinger caliper tools, sonic bond tools, and ultrasonic logging tools. Destructive tools (sampling and testing tools) include cased-hole mobility and fluid analysis tools, and sidewall coring tools. Destructive tools require a hole to be drilled in the casing or all the way into the formation to retrieve a composite sample, which damages the integrity of the wellbore during the measurement. Non-destructive tools leave the wellbore intact, but each of them is limited by the casing and fluid condition. For example, the ultrasonic logging tools are widely used due to its ability of specifying leakage pathways in 360 degrees, but it can only be used in wells where the fluid is clean and consistent in order to estimate the acoustic impedance of the fluid. Most importantly, all these tools can only be used after the cementing job has been completed, and the data provided is not time continuous.

An innovative real-time well tubular deformation monitoring system based on distributed coaxial cable sensors has recently been developed and evaluated in laboratory[10]. The laboratory experiment results proved the system's ability in real-time casing deformation monitoring, including axial compression, radial expansion, bending, and ovalization. In particular, the system demonstrated very accurate measurement results for axial compression in the range of 0.1%-1% strain. The system has full capability to be deployed for a well depth up to 2,500 ft, and with coaxial cables that could survive pressures of 10,000 psi and temperatures of 1,000 °C[11], the system is applicable for deeper downhole deployment.

To study the feasibility of using the coaxial cable casing imager for real-time wellbore integrity monitoring during CO_2 sequestration, a staged finite element model is constructed based on a well in the Weyburn field. The casing strain is analyzed both for the surface casing model and the production casing model in order to study the appropriate installation depth of the system. A sensitivity study is conducted on the casing strain under various conditions to investigate the possibility of detecting the change with the system. Radial and hoop stress change across the casing, cement, and formation composite as well as the interface gap distance change after CO_2 is injected is studied as indication of the wellbore leakage risk.

Methodology

A staged finite element model is established to study the long-term integrity and corresponding casing strain of a cased wellbore by including all loading steps occurring throughout the well's life. The thermal-mechanical finite element model simulates the initial conditions of the well, the drilling conditions, cementing conditions, and the injection conditions. Pore pressure is not taken into account in this model. Figure 1 shows the schematic of the constructed finite element model. The three dimensional model has a length of five meters in x and y directions and 0.1 meter in z direction, and the model is composed of first order C3D8RT elements (3-dimensioanl linear 8-nodes reduced thermal analysis elements). The model geometry is based on preventing unintentional boundary effects as a result of the temperature distribution reaching the boundary of the model. The model also assumes homogeneity material properties in all components of the well. Nodes on the front and back surfaces are constrained in the y direction, nodes on the left and right surfaces are constrained in the x direction, and nodes on the bottom surface is constrained in the z direction. The top surface is a free surface. The meshed geometry is created with HyperMesh^{TM} and the model analysis is conducted with Abaqus^{TM}. Stress and strain are calculated for the element centroid instead of the element nodes for higher accuracy.

The model is based on Well 101/6-30-5-13w2 in the Weyburn field[12]. Figure 2 shows the schematic of the well design. The well consists of two sections. The surface casing section is from surface to 89.33 m, and the production casing section is from surface to 1485.29 m. Both sections are cemented with the class G cement with a density of 1901 kg/m^3. The surface casing is cemented to top, and the cement top in the annular space between the production casing and formation is expected to be in the 1100 to 1200 meter range. 1100 m is chosen as the cement top in the production casing annulus in the model.

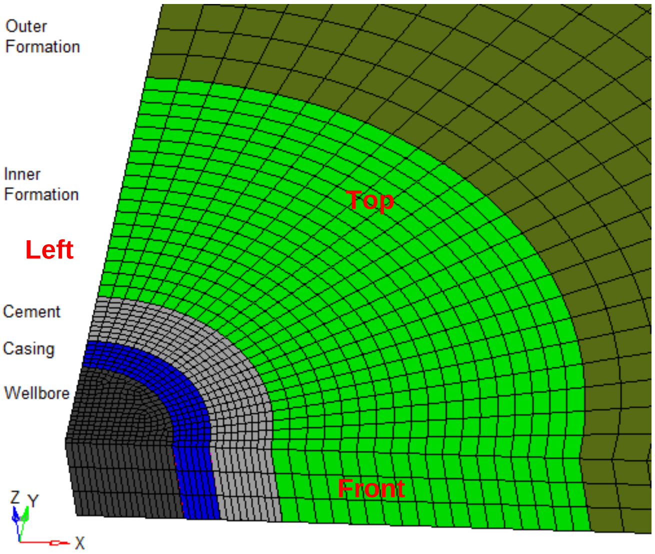

Figure 1. Schematic of the finite element model.

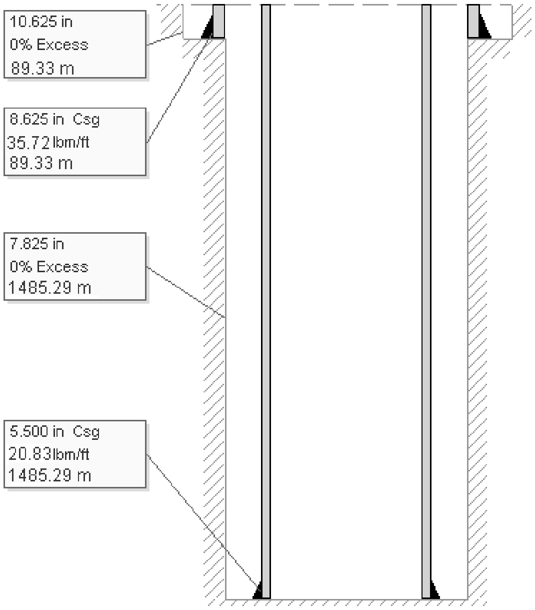

Figure 2. Schematic of well design of Well 101/6-30-5-13w2.

The material properties for each component of the wellbore are listed in Table 1[7], and the deterministic values (DV, values that remain unchanged in all simulation conditions) of the model for both surface casing and production casing are listed in Table 2. The formation temperature is calculated based on a geothermal gradient of 0.035°C/m[13]. The mud hydrostatic pressure is calculated on a fresh water density of 1000 kg/m^3. And the interface gap thermal conductance is based on the experimental and analytical results of a composite structural elements under simulated fire conditions[14] (Table 3).

Table 1. Thermal and mechanical properties of each component of the wellbore.

Wellbore component	Thermal properties			Mechanical properties		
	Thermal conductivity λ W/(m·K)	Specific heat c J/(g·°C)	Linear thermal expansion α m/(m·°C)	Density ρ Kg/m^3	Young's modulus E Pa	Poisson's ratio v
Wellbore (Formation)	0.29	900	1.0 E-5	2590	3.3E+10	0.23
Casing	43	490	1.1433E-05	7800	2.0E+11	0.3
Cement	0.29	900	9.71 E-6	1901	9.67 E+9	0.214

Table 2. Deterministic values for simulation conditions in surface and production casing.

Deterministic value	Surface casing	Production casing
Formation temperature °C	6.63	55.49
Injection wellhead pressure MPa	19.99	
Gap conductance W/(m^2·K)	See Table 6-3	
Mud hydrostatic pressure MPa	0.88	14.56
Cement hydrostatic pressure MPa	1.66	17.96

Table 3. Gap thermal conductance for the casing-cement and cement-formation interface.

Conductance $W/(m^2 \cdot K)$	Clearance m
160.122	0
123.272	1e-6
108.48	2e-6
103.671	3e-6
101.449	4e-6
100.211	5e-6
99.437	6e-6
98.9151	7e-6
98.5429	8e-6
98.2662	9e-6
98.0537	1e-5
97.8862	1.1e-5

The random values (RV, values that are different in each simulation condition) that are studied in the model include in-situ stress regime, interface bonding condition, cement shrinkage, injection temperature, and operation time of year.

In-situ stress.

Since there are no direct measurements of in-situ stresses for the Weyburn field, the in-situ stress regime is not clear. But according to Bell and Babcock[15], the field is located near the boundary between strike-slip and normal fault stress regimes. To account for the existing uncertainty in the in-situ stress data, different in-situ stress scenarios is considered, and the values of the in-situ stresses in these scenarios are based on the assumption of Jimenez[16]. Pore pressure (assume equals fresh water hydrostatic pressure) is subtracted from the total stress, and the most probable strike-slip scenario will be treated as the base-case scenario. The effective stress for each in-situ stress regime is listed in Table 4.

Table 4. Effective stress for each in-situ stress regime.

In-situ stress regime	Effective stress (MPa)					
	Surface casing			Production casing		
Strike-slip*	1.62	0.73	1.26	27.03	12.18	21.09
Normal	1.26	0.73	1.26	21.09	12.18	21.09
Isotropic	1.26	1.26	1.26	21.09	21.09	21.09
Thrust	2.07	2.07	1.26	34.45	34.45	21.09
* Base-case scenario.						

Table 5. Interface stiffness for different bonding conditions.

Bonding condition	Interface stiffness *k* (N/m)
Fully bonded*	2.5E+13
Small micro-annulus	4.03E+11
Large micro-annulus	8.55E+10
* Base-case scenario	

Interface bonding condition.

The micro-annuli formed on the casing-cement or cement-formation interface serve as potential leakage risk during CO_2 injection. Gomez[17] studied the compressibility and permeability of wellbore micro-annuli at the cement-casing interface. The study shows that even an increase of a few microns of the micro-annuli could increase the permeability a few times. The interface stiffness can be calculated based on the fitted curve from the experimental data for small and large micro-annuli (Table 5). Cohesive surfaces are used on the casing-cement and cement-formation interfaces to study the interface gap distance change caused by CO_2 injection. The interface friction factor is 2.76, which is calculated based on the push-out test of the cement-rock composite[18].

Cement shrinkage.

Cement shrinkage as a result of hydration or cement expansion as a result of expanding agents added to the cement slurry may cause cement failure[19-21]. The parameters of shrinkage used in the model are 0% (based-case scenario), 0.1% shrinkage, 0.5% shrinkage, -0.1% shrinkage (0.1% expansion), and -0.5% shrinkage (0.5% expansion).

Injection temperature.

CO_2 is transported to the Weyburn field via a 320 km long pipeline from the power plant in North Dakota, and by the time it is transported to the site, the temperature should get close the ambient temperature. To maintain the CO_2 at liquid condition in the wellbore, it should be heated up to 35 °C before injection[22]. However, it is not economically realistic for an industrial sized CO_2 storage setting. To study the effect of injection temperature on wellbore integrity, both injecting at ambient temperature (base-case scenario) and 35 °C are studied in the model.

Operation time of year.

The ambient temperature in the Weyburn field varies significantly throughout the year. The maximum temperature difference in a year could be as much as 47.3 °C[23]. When injecting the CO_2 at ambient temperature, the operation time of the year should be considered to account for the effect of injection temperature difference. Four typical ambient temperatures are selected in the model (Table 6).

Table 6. Selected operation time of year.

Operation time of year	January*	March	July	October
Ambient temperature (°C)	-14.9 °C	-4.9 °C	19.7 °C	6.3 °C
* Base-case scenario				

Results

The radial and hoop stress change across the casing, cement, and formation caused by CO_2 injection are studied, and the interface gap distance change are calculated as indication of wellbore leakage risk. The corresponding casing strain under each simulation condition is analyzed to investigate whether the coaxial cable casing imager could be applied in these situations.

Surface casing model.

The radial and hoop stress change for the base-case scenario is shown in Figure 3. The casing, cement, and formation are represented by the blue, grey, and green areas, respectively. The result shows no risk of radial de-bonding of the cement from the casing or formation, but indicates risk of tensile failure of the cement. The interface gap distance change and casing strain under each simulation condition are listed in Table 7 and Table 8. The interface gaps are reduced greatly after CO_2 injection, and the negative interface distance after injection means the nodes on the interface are contacted, which means the interface leakage risk is reduced. The casing hoop strain is increased after injection, and the casing axial strain changed from tension to compression after injection.

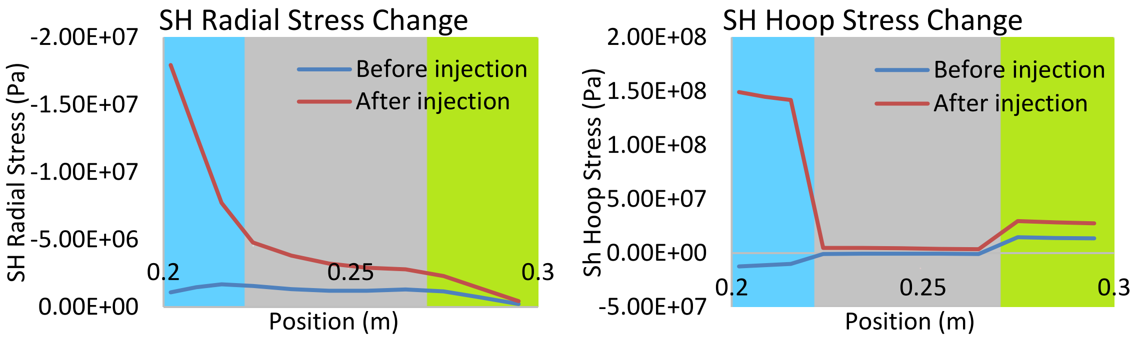

Figure 3. Radial and hoop stress change for the base-case scenario of surface casing model.

Table 7. Interface gap distance change under each simulation condition for surface casing model.

Simulation conditions		Casing-cement interface gap (m)		Cement-formation interface gap (m)	
		Before	After	Before	After
Base-case scenario		1.60E-09	-4.27E-18	4.14E-09	-5.79E-19
In-situ stress regime	Normal	1.55E-09	1.15E-18	4.50E-09	9.40E-20
	Isotropic	1.62E-09	-1.83E-18	3.97E-09	-1.39E-18
	Thrust	1.82E-09	-8.04E-18	2.36E-09	4.80E-18
Interface bonding	Small micro-annulus	6.21E-08	8.29E-19	2.23E-07	-1.61E-18
	Large micro-annulus	8.72E-08	9.57E-18	7.24E-07	9.00E-19
Cement shrinkage	-0.50%	**1.60E-09**	**1.68E-08**	4.14E-09	2.16E-09
	-0.10%	1.60E-09	-9.95E-19	4.14E-09	-6.28E-18
	0.10%	1.60E-09	2.84E-18	4.14E-09	9.64E-18
	0.50%	1.60E-09	1.52E-19	**4.14E-09**	**4.91E-08**
Injection temperature	35 °C	1.60E-09	4.67E-18	4.14E-09	4.67E-18
Operation time of year	March	1.60E-09	3.50E-18	4.14E-09	1.06E-17
	July	1.60E-09	1.77E-18	4.14E-09	9.67E-20
	October	1.60E-09	1.88E-18	4.14E-09	-1.59E-18

Table 8. Casing strain change under each simulation condition for surface casing model.

Simulation conditions		Casing hoop strain (%)		Casing axial strain (%)	
		Before	After	Before	After
Base-case scenario		-0.01%	0.05%	0.05%	-0.04%
In-situ stress regime	Normal	-0.01%	0.05%	0.00%	-0.04%
	Isotropic	-0.01%	0.05%	0.00%	-0.04%
	Thrust	0.00%	0.05%	0.00%	-0.04%
Interface bonding	Small micro-annulus	-0.01%	0.05%	0.00%	-0.04%
	Large micro-annulus	0.00%	0.05%	0.00%	-0.04%
Cement shrinkage	-0.50%	-0.01%	0.05%	0.00%	-0.03%
	-0.10%	-0.01%	0.05%	0.00%	-0.04%
	0.10%	-0.01%	0.05%	0.00%	-0.04%
	0.50%	-0.01%	0.05%	0.00%	-0.05%
Injection temperature	35 °C	-0.01%	**0.10%**	0.00%	0.01%
Operation time of year	March	-0.01%	0.06%	0.00%	-0.03%
	July	-0.01%	**0.09%**	0.00%	0.00%
	October	-0.01%	0.07%	0.00%	-0.02%

The surface casing model radial and hoop stress difference between casing, cement, and formation after injection are calculated for all simulation conditions and are normalized against the base-case scenario, as shown in Table 9 and Table 10. The stress data is taken from the middle of the wellbore component.

Table 9. Surface casing model normalized radial stress difference in wellbore components after injection.

Simulation conditions		Casing-Cement difference MPa	Normalized value	Cement-Formation difference MPa	Normalized value
Base-case scenario		-4.5	1.0	-1.85	1.0
In-situ stress regime	Normal	-4.83	1.07	-1.51	0.82
	Isotropic	-4.75	1.06	-1.52	0.82
	Thrust	-4.61	1.02	-1.58	0.85
Interface bonding	Small micro-annulus	-4.66	1.04	-1.61	0.87
	Large micro-annulus	-4.34	0.96	-1.78	0.96
Cement shrinkage	-0.50%	-10.3	**2.29**	5.49	**-2.97**
	-0.10%	-5.66	**1.26**	-0.39	**0.21**
	0.10%	-3.88	0.86	-3.647	1.97
	0.50%	-0.12	**0.03**	-7.763	**4.20**
Injection temperature	35 °C	-4.33	0.96	-1.87	1.01
Operation time of year	March	-4.72	1.05	-1.6	0.86
	July	-4.47	0.99	-1.77	0.96
	October	-4.61	1.02	-1.67	0.90

The results under different in-situ stress regimes and interface bonding conditions are similar to the base-case scenario, with risk of cement tensile failure (Table 10) and reduced leakage risk at interfaces (Table 7). However, the cement shrinkage/expansion has significant influence on the interface de-bonding and leakage risk. -0.5% cement shrinkage (0.5% expansion) increased both the radial and hoop stress difference between wellbore components with increased casing-cement interface gap. 0.5% cement shrinkage increased the radial stress difference between cement and formation with increased cement-formation interface gap, but the radial stress difference between casing and cement is greatly reduced, as well as the hoop stress difference for all three components. -0.1% cement shrinkage (0.1% expansion) greatly reduced the radial stress difference between cement and formation, which means the cement tensile failure risk is reduced. The radial and hoop stress change under -0.5%, -0.1%, and 0.5% cement shrinkage are shown in Figure 4, Figure 5, and Figure 6, respectively.

Table 10. Surface casing model normalized hoop stress difference in wellbore components after injection.

Simulation conditions		Casing-Cement difference MPa	Normalized value	Cement-Formation difference MPa	Normalized value
Base-case scenario		137.97	1.0	-24.47	1.0
In-situ stress regime	Normal	138.02	1.00	-24.62	1.01
	Isotropic	138.43	1.00	-25.43	1.04
	Thrust	139.95	1.01	-26.45	1.08
Interface bonding	Small micro-annulus	137.98	1.00	-24.58	1.00
	Large micro-annulus	139.01	1.01	-24.61	1.01
Cement shrinkage	-0.50%	160.45	**1.16**	-52.65	**2.15**
	-0.10%	142.37	1.03	-30.07	1.23
	0.10%	133.57	0.97	-18.97	0.78
	0.50%	114.8	**0.83**	4.3	**-0.18**
Injection temperature	35 °C	132.85	0.96	-27.55	1.13
Operation time of year	March	136.75	0.99	-25.15	1.03
	July	134.2	0.97	-26.6	1.09
	October	135.5	0.98	-25.8	1.05

The stress change under 35 °C injection temperature is similar to the base-case scenario, but the casing hoop strain under this condition is the largest among all the simulation conditions (0.1% casing hoop strain, Table 8), which is caused by the thermal expansion of the casing due to higher injection temperature. And similarly, the stress change under different operation times of the is similar to the based-case scenario, but the casing hoop strain for the simulation in July is very close to the strain generated when injecting at 35 °C (0.09% casing hoop strain, Table 8).

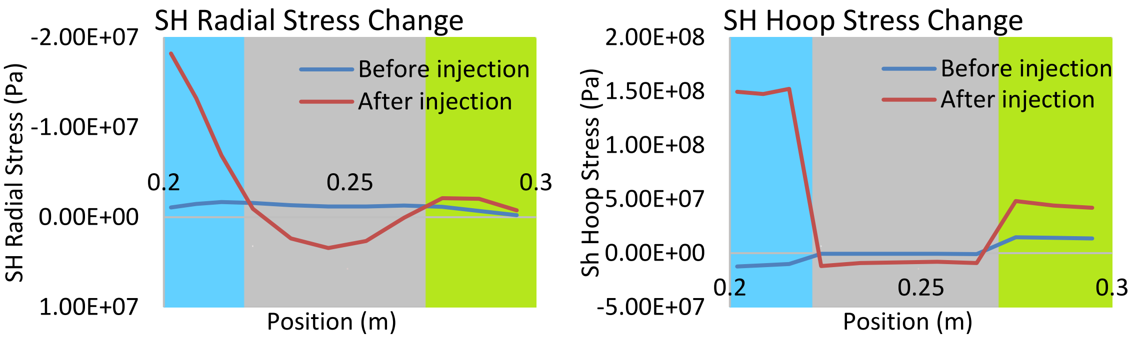

Figure 4. Radial and hoop stress change under -0.5% cement shrinkage for surface casing model.

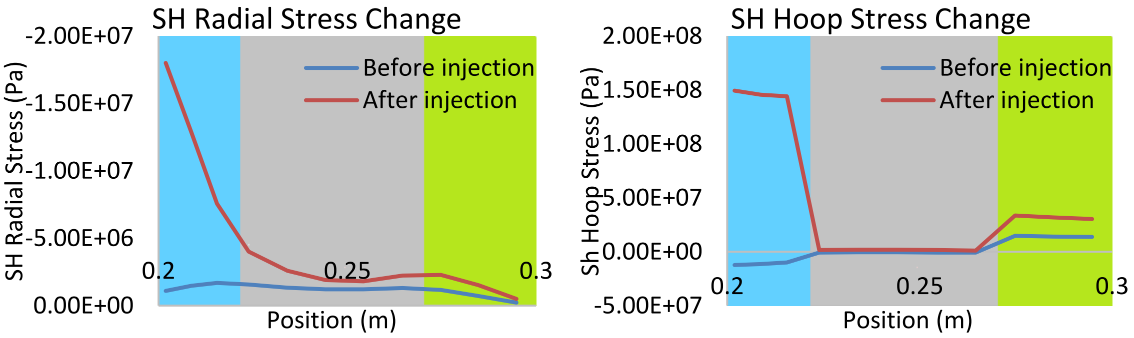

Figure 5. Radial and hoop stress change under -0.1% cement shrinkage for surface casing model.

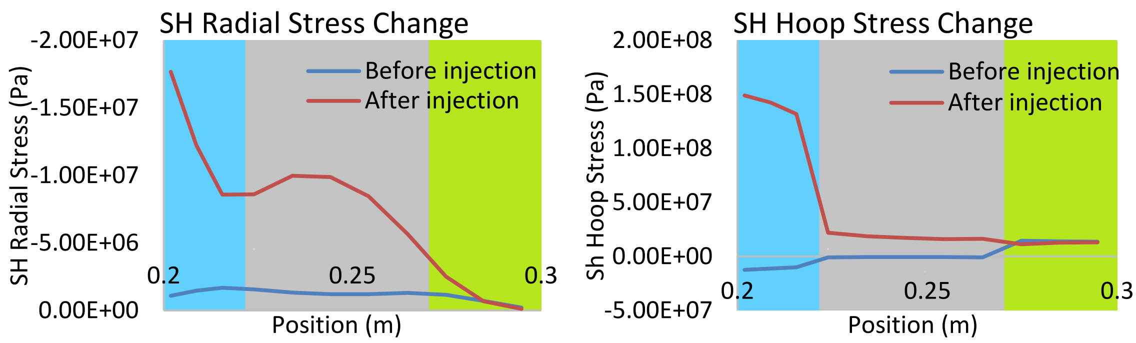

Figure 6. Radial and hoop stress change under 0.5% cement shrinkage for surface casing model.

Production casing model.

The radial and hoop stress change for the base-case scenario is shown in Figure 7. The result shows the risk of radial de-bonding of the cement from the casing or formation, and the risk of tensile failure of the cement. This is also consistent with the increase gap distance both on the casing-cement and cement-formation interfaces (Table 11). And compared to the surface casing base-case scenario, the casing hoop strain and axial strain are larger in the production casing based-case scenario (Table 12), which is caused by the larger in-situ stress and hydrostatic pressure at larger well depth.

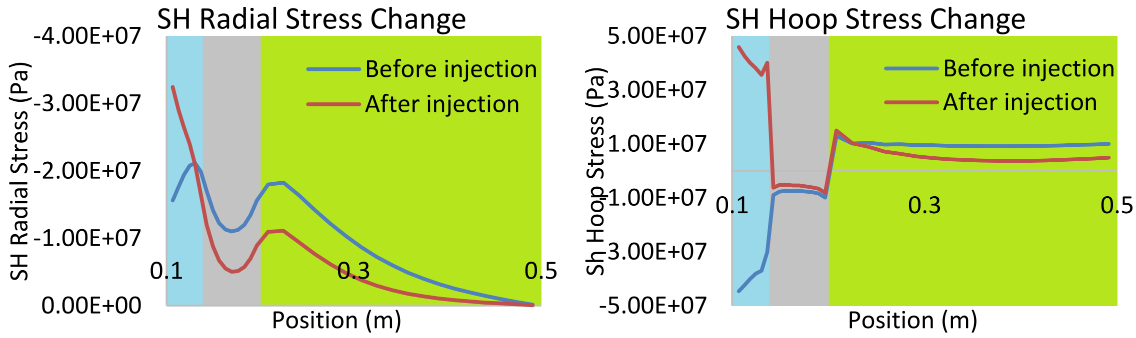

Figure 7. Radial and hoop stress change for the base-case scenario of production casing model.

Table 11. Interface gap distance change under each simulation condition for production casing model.

Simulation conditions		Casing-cement interface gap (m)		Cement-formation interface gap (m)	
		Before	After	Before	After
Base-case scenario		4.73E-08	2.55E-07	3.02E-08	2.35E-07
In-situ stress regime	Normal	6.55E-08	2.88E-07	6.22E-08	2.87E-07
	Isotropic	3.82E-08	2.38E-07	1.84E-08	2.10E-07
	Thrust	**1.18E-15**	**1.16E-07**	**1.69E-14**	**1.64E-08**
Interface bonding	Small micro-annulus	1.81E-06	1.41E-05	1.53E-06	1.20E-05
	Large micro-annulus	2.41E-06	3.09E-05	4.58E-06	2.14E-05
Cement shrinkage	-0.50%	4.73E-08	2.55E-07	3.02E-08	2.35E-07
	-0.10%	4.73E-08	2.55E-07	3.02E-08	2.35E-07
	0.10%	4.73E-08	3.18E-07	3.02E-08	3.26E-07
	0.50%	4.73E-08	5.73E-07	3.02E-08	6.89E-07
Injection temperature	35 °C	**4.73E-08**	**5.16E-08**	**3.02E-08**	**3.87E-08**
Operation time of year	March	4.73E-08	1.99E-07	3.02E-08	1.90E-07
	July	**4.73E-08**	**9.78E-08**	**3.02E-08**	**8.82E-08**
	October	4.73E-08	1.46E-07	3.02E-08	1.40E-07

Table 12. Casing strain change under each simulation condition for production casing model.

Simulation conditions		Casing hoop strain (%)		Casing axial strain (%)	
		Before	After	Before	After
Base-case scenario		-0.02%	-0.06%	0.02%	-0.07%
In-situ stress regime	Normal	-0.02%	-0.06%	0.02%	-0.07%
	Isotropic	-0.02%	-0.06%	0.02%	-0.07%
	Thrust	-0.02%	-0.07%	0.02%	-0.07%
Interface bonding	Small micro-annulus	-0.02%	-0.07%	0.02%	-0.07%
	Large micro-annulus	-0.02%	-0.07%	0.01%	-0.07%
Cement shrinkage	-0.50%	-0.02%	**-0.08%**	0.02%	-0.05%
	-0.10%	-0.02%	-0.07%	0.02%	-0.07%
	0.10%	-0.02%	-0.06%	0.02%	-0.07%
	0.50%	-0.02%	-0.04%	0.02%	**-0.09%**
Injection temperature	35 °C	-0.02%	**-0.02%**	0.02%	**-0.01%**
Operation time of year	March	-0.02%	-0.05%	0.02%	-0.06%
	July	-0.02%	**-0.03%**	0.02%	**-0.03%**
	October	-0.02%	-0.04%	0.02%	-0.04%

The production casing model radial and hoop stress difference between casing, cement, and formation after injection are calculated for all simulation conditions and are normalized against the base-case scenario, as shown in Table 13 and Table 14. The stress data is taken from the middle of the wellbore component.

Table 13. Production casing model normalized radial stress difference in wellbore components after injection.

Simulation conditions		Casing-Cement difference MPa	Normalized value	Cement-Formation difference MPa	Normalized value
Base-case scenario		-18.88	1.0	-3.36	1.0
In-situ stress regime	Normal	-19.91	1.05	-2.904	0.86
	Isotropic	-18.86	1.00	-5.44	1.62
	Thrust	-16.5	0.87	-10.59	**3.15**
Interface bonding	Small micro-annulus	-16.8	0.89	-3.6	1.07
	Large micro-annulus	-15.2	0.81	-6.94	**2.07**
Cement shrinkage	-0.50%	-18.88	1.00	-3.36	1.00
	-0.10%	-20.15	1.07	-3.52	1.05
	0.10%	-17.51	0.93	-3.2	0.95
	0.50%	-12.35	**0.65**	-2.526	**0.75**
Injection temperature	35 °C	-16.9	0.90	-6.67	1.99
Operation time of year	March	-20.73	1.10	-4.01	1.19
	July	-17.5	0.93	-5.63	1.68
	October	-20.14	1.07	-4.75	1.41

The stress change under thrust in-situ stress regime and large micro-annulus interface bonding condition both show increased radial and hoop stress difference between cement and formation, indicating increased risk of interface de-bonding. And the interface gap distance increase is the largest compared to before injection under thrust in-situ stress regime. The radial and hoop stress change for these two simulation conditions are shown in Figure 8 and Figure 9.

Table 14. Production casing model normalized hoop stress difference in wellbore components after injection.

Simulation conditions		Casing-Cement difference MPa	Normalized value	Cement-Formation difference MPa	Normalized value
Base-case scenario		43.59	1.0	-9.31	1.0
In-situ stress regime	Normal	45.57	1.05	-9.27	1.00
	Isotropic	46.9	1.08	-17.97	1.93
	Thrust	45.2	1.04	-30.96	**3.33**
Interface bonding	Small micro-annulus	38.53	0.88	-13.39	1.44
	Large micro-annulus	40.7	0.93	-20.19	**2.17**
Cement shrinkage	-0.50%	43.59	1.00	-9.31	1.00
	-0.10%	38.24	0.88	-13.58	1.46
	0.10%	49.21	1.13	-5.41	**0.58**
	0.50%	70.75	**1.62**	11.42	**-1.23**
Injection temperature	35 °C	21.49	**0.49**	-15.18	**1.63**
Operation time of year	March	39.39	0.90	-10.72	1.15
	July	27.98	0.64	-13.16	1.41
	October	34.32	0.79	-11.87	1.27

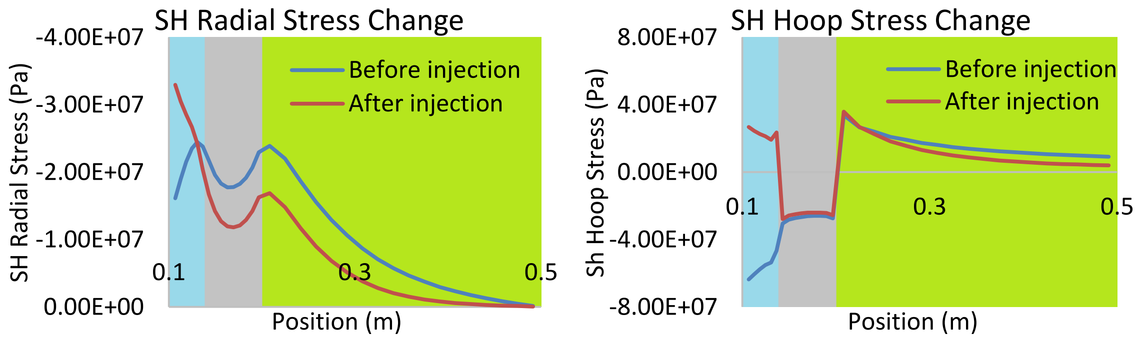

Figure 8. Radial and hoop stress change under thrust in-situ stress regime for production casing model.

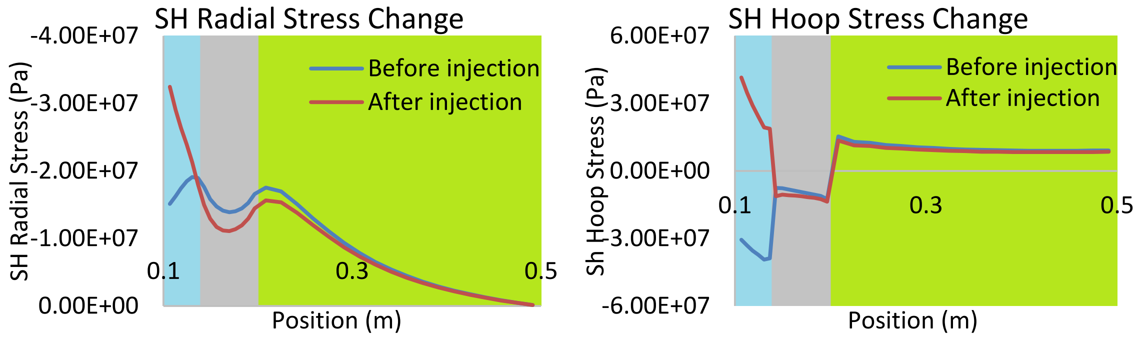

Figure 9. Radial and hoop stress change under large micro-annulus interface bonding condition for production casing model.

The cement shrinkage/expansion also has significant influence on the interface debonding and leakage risk for the production casing model. 0.5% cement shrinkage causes reduced radial stress difference and increased hoop stress difference between wellbore components, with the largest casing axial strain (0.09% casing axial strain, Table 12). 0.1% cement shrinkage greatly reduced the hoop stress difference between the cement and formation, indicating reduced cement failure risk. -0.5% cement shrinkage (0.5% expansion) did not cause any change in the radial and hoop stress difference between wellbore components (normalized values are 1.0, Table 13 and Table 14), but the casing hoop strain is the largest among all simulation conditions (0.08% casing hoop strain, Table 12). The radial and hoop stress change under 0.1% and 0.5% cement shrinkage are shown in Figure 10 and Figure 11, respectively.

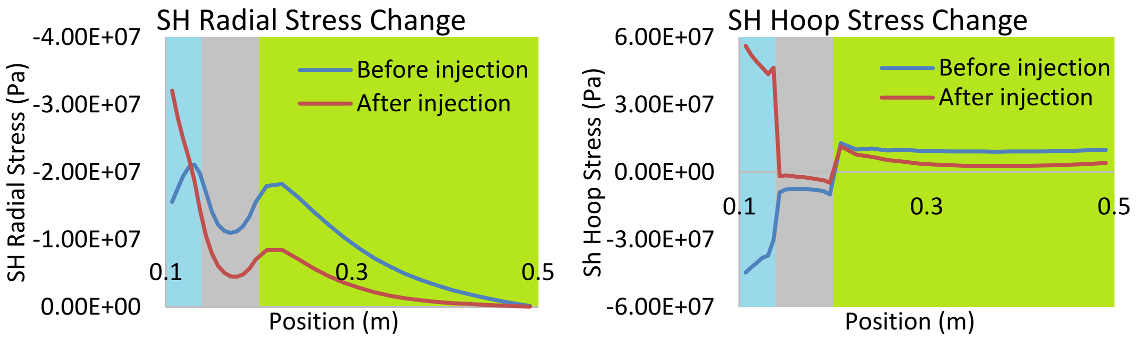

Figure 10. Radial and hoop stress change under 0.1% cement shrinkage for production casing model.

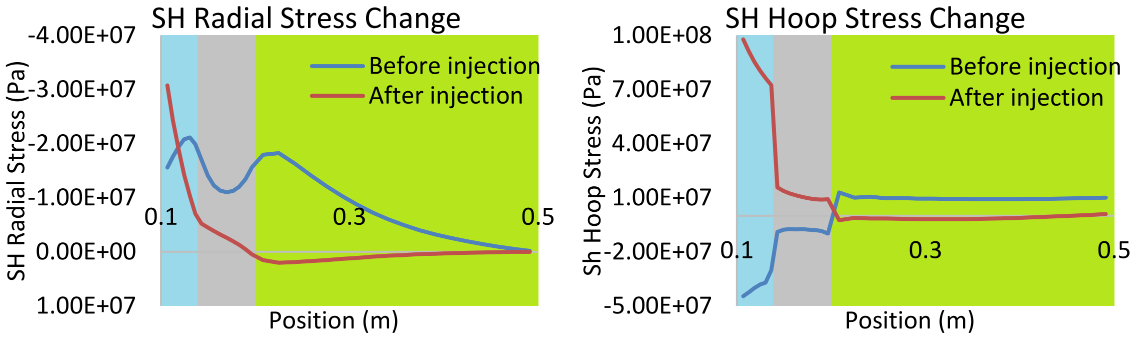

Figure 11. Radial and hoop stress change under 0.5% cement shrinkage for production casing model.

The stress change under 35 °C injection temperature shows no risk of cement radial de-bonding after injection, but shows risk of cement tensile failure. The interface gap distance did not change after injection (Table 11), which means the leakage risk at the interfaces remains constant. And the casing hoop strain and radial strain are the smallest in all the simulations (Table 12). Similarly, the result of operating in July shows very small interface gap change and casing strain. The radial and hoop stress change for simulations under 35 °C injection temperature and operating time in July are shown in Figure 12 and Figure 13, respectively.

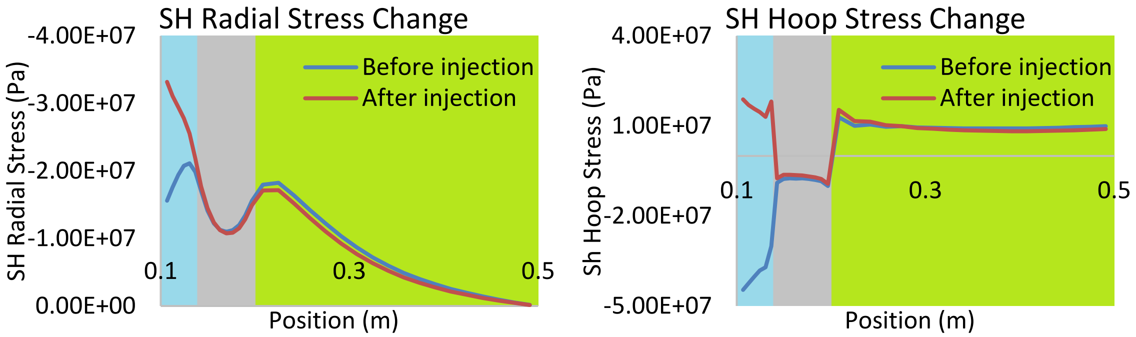

Figure 12. Radial and hoop stress change under elevated injection temperature for production casing model.

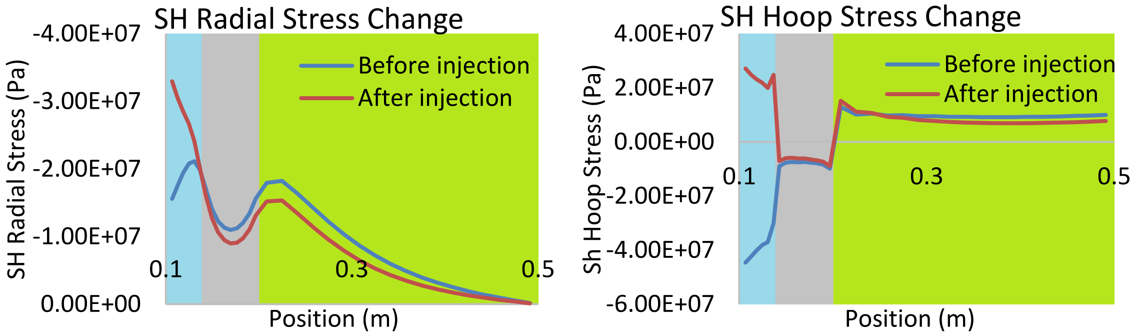

Figure 13. Radial and hoop stress change under operating time of July for production casing model.

Discussion

In all the simulation conditions in the production casing model, the casing-cement and cement-formation interface gaps are increased, which means the leakage risk at the interfaces are increased. The simulation result shows that the production casing is at greater leakage risk. And compared to the surface casing model, the production casing model generally creates larger casing strain in the simulation conditions due to the larger in-situ stress and hydrostatic pressure at larger depth. Since the coaxial cable casing imager has higher measurement accuracy under larger casing strain within the range of 0.1% to 1.0% strain when the system is deployed at 23 degree wrapping angle[10], the system would have better performance if it is installed on the production casing.

In-situ stress regimes have no significant influence on the wellbore integrity in the surface casing model, but the thrust in-situ stress regime caused increased stress difference between cement and formation for the production casing model, and the gap distance increase is the largest compared to the distance before injection. The interface bonding condition has no effect in the surface casing model either, but in the production casing model, the existence of small and large micro-annulus makes the interface gaps much larger than the other simulation conditions, and the large micro-annulus on the interface increased the hoop stress difference between cement and formation, which puts more risk on the interface leakage.

Cement shrinkage has a significant influence on the wellbore integrity. In the surface casing model, -0.5% shrinkage increased the casing-cement interface gap and 0.5% shrinkage increased cement-formation interface gap. In the production casing model, both interface gaps are increased at -0.5% shrinkage and 0.5% shrinkage. The increased interface gap indicates increased leakage risk at the interface.

Increasing the injection temperature to 35 °C generates the largest casing strain in the surface casing model, but no significant benefits or damage are observed on the wellbore integrity. On contrary, in the production casing model the 35 °C injection temperature generates the smallest casing strain, and the cement radial de-bonding risk is reduced. Although injecting CO_2 at elevated temperature has benefit on wellbore integrity in the production casing section, whether it is economically realistic for an industrial sized CO_2 storage setting remains questionable.

When injecting at ambient temperature, the operation time of year has no significant effect on the wellbore integrity in the surface casing model, but it generates the largest casing strain. However, in the production casing model, injecting in July generates the smallest interface gap change and very small casing strain, which reduces the leakage risk compared to other injection times of the year.

For the majority of the simulation conditions, the casing strain is smaller than 0.1%, which is within the range of large measurement error of the coaxial cable casing imager. To be able to deploy the system for CO_2 sequestration wellbore integrity monitoring in the Weyburn field, the system needs to be improved to have more accurate measurement for casing strain smaller than 0.1%.

Another solution is to increase the system's sensitivity by reducing the wrapping angle so that larger strain would be generated on the sensor. The casing strain and sensor strain correlation is represented by Equation 1,

$$\varepsilon = K\left(1 - \sqrt{sin^2\theta(1-\varepsilon_a)^2 + cos^2\theta(1+\nu\varepsilon_a)^2}\right) \tag{1}$$

Where ε is the sensor measured strain; ε_a is the casing axial strain; ν is the Poisson's ratio of the casing material; θ is the wrapping angle; K is the bonding factor between the casing and cable, which represents how well the casing strain is reflected on strain sensors.

When the system is deployed at 23 degree, to maintain the high measurement accuracy, the casing axial strain needs to be larger than 0.1%, which will translate into 0.02% sensor strain based on Equation 1. This means that the sensor strain needs to be larger than 0.02% to be able to provide accurate measurement. By changing the wrapping angle of the system, smaller casing axial strain could be measured with higher accuracy. Examples of the casing axial strain that could be measured at different wrapping angles are listed in Table 15.

Table 15. Casing axial strain that could be measured with higher accuracy at different wrapping angles.

Wrapping angle degree	Min. casing axial strain that could be measured %
20	0.07%
15	0.05%
7	0.04%

Conclusions

A staged finite element model based on a well in the Weyburn field is established to study the feasibility of using the coaxial cable casing imager for real-time CO_2 sequestration wellbore integrity monitoring and evaluation. The simulation result shows that the production casing is at greater leakage risk compared to the surface casing, thus the system is more beneficial to be installed on the production casing.

The casing strain in all simulations is analyzed and found to be smaller than 0.1%, which is below the system's optimum performance range. The system needs to be improved to have higher measurement accuracy at smaller casing strain, or the wrapping angle needs to be reduced to increase the system's sensitivity in order to measure smaller casing strain.

The sensitivity study shows that in-situ stress regime and interface bonding condition have negligible effect on the wellbore integrity in the surface casing model, but the existence of small and large micro-annulus could increase the interface leakage risk in the production casing model. Cement shrinkage has a significant influence on the wellbore integrity both in the surface and production casing model. Injecting at elevated temperature has no effect on the surface casing model, but could reduce the cement radial de-bonding risk in the production casing model. And when injecting at ambient temperature in the production casing model, operating in July could reduce the interface leakage risk compared to operating at other times of the year.

Acknowledgements

The authors would like to thank the financial support from the Department of Energy under Award Number DE-FE0009284.

References

1. Bacon, D. H. (2013). *Reduced-Order Model for the Geochemical Impacts of Carbon Dioxide, Brine and Trace Metal Leakage into an Unconfined, Oxidizing Carbonate Aquifer, Version 2.1* (No. PNNL-22285). Pacific Northwest National Laboratory (PNNL), Richland, WA (US).

2. Harvey, O. R., Cantrell, K. J., Qafoku, N. P., & Brown, C. F. (2012). Geochemical Implications of CO2 Leakage Associated with Geologic Storage: A Review. *Report prepared for the US Department of Energy under Contract DE-AC05-76RL01830.*

3. Little, M. G., & Jackson, R. B. (2010). Potential impacts of leakage from deep CO2 geosequestration on overlying freshwater aquifers. *Environmental science & technology*, *44*(23), 9225-9232.

4. Pearce, J. M., & West, J. M. (2007). Study of potential impacts of leaks from onshore CO2 storage projects on terrestrial ecosystems. *IEA Greenhouse Gas R&D Programme Technical Study*, *3*.

5. Smith, K. L., Steven, M. D., Jones, D. G., West, J. M., Coombs, P., Green, K. A., ... & Beaubien, S. E. (2013). Environmental impacts of CO 2 leakage: recent results from the ASGARD facility, UK. *Energy Procedia*, *37*, 791-799.

6. Watson, T. L., & Bachu, S. (2007, January). Evaluation of the potential for gas and CO2 leakage along wellbores. In *E&P Environmental and Safety Conference*. Society of Petroleum Engineers.

7. Weideman, B. L. (2014). *Investigation of cased wellbore integrity in the Wabamun area sequestration project* (Master's Thesis). Retrieved from http://scholarsmine.mst.edu/masters_theses/7284/

8. Rusch, D. W., Sabins, F., & Aslakson, J. (2004, January). Microannulus leaks repaired with pressure-activated sealant. In *SPE Eastern Regional Meeting*. Society of Petroleum Engineers.

9. Duguid, A., & Tombari, J. (2007, May). Technologies for measuring well integrity in a CO2 field. In *Sixth Annual Conference on Carbon Capture and Sequestration—DOE/NETL, May* (pp. 7-10).

10. Li, Y., Cheng, B., Zhu, W., Nygaard, R., & Xiao, H. (2016). Laboratory Evaluation of a Real-Time Coaxial Cable Casing Imager for Wellbore Integrity Monitoring. Unconventional Resources Technology Conference, Aug. 1-3, San Antonio, TX, US.

11. Thermocoax Incorporated (2012). Mineral insulated signal transmission cable. Retrieved from http://www.thermocoax-nuclear.com/nuclear---transmission-cable-application.html

12. Cenovus Energy Inc. (2011). Infrastructure and well integrity assessment of SW 30-5-13w2. Retrieved from http://www.cenovus.com/operations/docs/Cenovus-infrastructure.pdf

13. Nabih, A., & Chalaturnyk, R. J. (2014, June). Stochastic Life Cycle Approach to Assess Wellbore Integrity for CO2 Geological Storage. In *SPE Heavy Oil Conference-Canada*. Society of Petroleum Engineers.

14. Mago, N., Hicks, S., & Simms, W. (2016). Sequentially coupled thermal-stress analysis of a new steel concrete composite slab under fire. *SESOC Journal*, *29*(1), 37.

15. Bell, J. S., & Babcock, E. A. (1986). The stress regime of the Western Canadian Basin and implications for hydrocarbon production. *Bulletin of Canadian Petroleum Geology*, *34*(3), 364-378.

16. Jimenez, J. (2006). *Geomechanical performance assessment of CO2-EOR Geological Storage Project* (Doctoral dissertation, Ph. D. thesis, University of Alberta).

17. Gomez, S. (2015). *Wellbore Microannulus Characterization and Seal Repair: Computational and Lab Scale Modeling* (Doctoral dissertation). Retrieved from http://repository.unm.edu/handle/1928/30336

18. Tepnarong, P. (2012, January). Bond strength of cement sealing in Maha Sarakham salt. In ISRM Regional Symposium-7th Asian Rock Mechanics Symposium. International Society for Rock Mechanics.

19. Bois, A. P., Garnier, A., Galdiolo, G., & Laudet, J. B. (2012). Use of a mechanistic model to forecast cement-sheath integrity. *SPE Drilling & Completion*, *27*(02), 303-314.

20. Bois, A. P., Garnier, A., Rodot, F., Sain-Marc, J., & Aimard, N. (2011). How to prevent loss of zonal isolation through a comprehensive analysis of microannulus formation. *SPE Drilling & Completion*, *26*(01), 13-31.

21. Bosma, M., Ravi, K., Van Driel, W., & Schreppers, G. J. (1999, January). Design approach to sealant selection for the life of the well. In *SPE Annual Technical Conference and Exhibition*. Society of Petroleum Engineers.

22. Möller, F., Liebscher, A., Martens, S., Schmidt-Hattenberger, C., & Streibel, M. (2014). Injection of CO2 at Ambient Temperature Conditions–Pressure and Temperature Results of the "cold injection" Experiment at the Ketzin Pilot Site. *Energy Procedia*, *63*, 6289-6297.

23. Climate-data (2016). Historical weather data: Weyburn. Retrieved from http://en.climate-data.org/location/11916/

SECTION

4. CONCLUSIONS

The coaxial cable temperature sensor is tested under simulated downhole conditions with water for sensor accuracy, sensitivity, stability, hysteresis, and crosstalk effect. A lab-scale prototype of the coaxial cable casing imager is developed and tested for real-time monitoring ability of casing axial compression, radial expansion, bending, and ovalization. A staged finite element model is constructed based on a well in the Weyburn field to study the feasibility of using the developed sensing system for wellbore stability monitoring by conducting a parametric study of the CO_2 injection conditions.

Based on the work in this dissertation the following conclusions can be drawn.

(1) The coaxial cable temperature sensor is proved to have an accuracy of 1% at atmospheric pressure.

(2) The coaxial cable temperature sensor is proved to perform under 1,000 psia and 110 °C in water.

(3) At 1,000 psia, the sensor sensitivity tends to stabilize and the hysteresis is reduced almost to zero after repeated heating/cooling cycles.

(4) The temperature sensor is more stable at low temperature than at high temperature.

(5) Pressure crosstalk has a very large influence on the temperature sensor measurement. Compared to the flexible sensor, the pressure crosstalk and hysteresis are both greatly reduced on the rigid sensor.

(6) The coaxial cable casing imager has been proved to have real-time casing deformation monitoring ability in axial compression, radial expansion, bending, and ovalization.

(7) The casing imager has higher accuracy for casing axial strain between 0.1% and 1.0%, and lower accuracy for axial strain below 0.1%.

(8) The radial expansion test setup needs to be improved to be able to generate uniform radial deformation on the pipe to characterize the casing imager performance in radial expansion deformation.

(9) The casing imager is proved to measure bending angle below 4 degrees.

(10) Pipe original roundness and sensor size limit the system's performance in casing ovalization measurement.

(11) The bonding factor of the system needs to be carefully evaluated before it is subjected to field application.

(12) The finite element analysis result shows that the production casing is at greater leakage risk compared to the surface casing, thus the system is more beneficial to be installed on the production casing.

(13) The casing strain in all simulations is found to be smaller than 0.1%, which is below the system's optimum performance range.

(14) In-situ stress regime and interface bonding condition have negligible effect on the wellbore integrity in the surface casing model, but the existence of small and large micro-annulus in the production casing model could increase the interface leakage risk.

(15) Cement shrinkage has a significant influence on the wellbore integrity both in the surface and production casing model.

(16) Injecting at elevated temperature has no effect on the surface casing model, but could reduce the cement radial de-bonding risk in the production casing model.

(17) When injecting at ambient temperature in the production casing model, operating in July could reduce the interface leakage risk compared to operating at other times of the year.

Overall, the testing of the distributed CCFPI temperature sensor under simulated downhole conditions fills in the gap where the fiber optic sensors are only manufactured and tested under surface conditions, which is crucial since pressure could affect the sensor accuracy. And compared to the OFS, the system installation would be simplified due to the fact that no reference temperature bath at surface or downhole temperature gauge is needed for temperature calibration.

A real-time coaxial cable casing imager has been developed to monitor the casing deformation (axial compression, radial expansion, bending, and ovalization) which could provide early warnings of CO_2 leakage risk. This system enables continuous visualization of casing deformation with great sensitivity and a very high spatial resolution without requiring entry into the casing.

The finite element analysis proved the feasibility of using the coaxial cable casing imager for real-time wellbore stability monitoring in the Weyburn field. The parametric study of various injection conditions provides insight into the best cementing practice to avoid potential leakage risk.

This intelligent well monitoring system would prove great value in real-time monitoring of casing temperature profile and deformation to detect early wellbore leakage risk that will contaminate the ground water. As a novel downhole sensing technology, the low cost and robustness of the distributed coaxial cable sensors will not only lower the downhole monitoring cost, but will also enhance the monitoring system stability and longevity, which will provide continuous monitoring during each stage of well operation and throughout the lifetime of the well to provide input to reservoir characterization, wellbore stability analysis, fracture operation evaluation and production appraisal.

5. FUTURE WORK

The results of the coaxial cable sensing system in this work have demonstrated full capability to be applied in field for CO_2 sequestration wellbore integrity monitoring. More work can be done to enhance the system's performance and extend its application in other areas through numerical simulations.

5.1. TEMPERATURE SENSOR IMPROVEMENT

In this work, the temperature sensor has only been characterized with water under simulated downhole conditions. More experiments can be done to characterize the sensor performance with fluid CO_2 and oil, which is closer to downhole conditions when the system is in field application.

The highest pressure and temperature rating in the experiments is 1,000 psia and 110 °C. The testing apparatus design can be improved to test the sensor performance under higher pressure and temperature rating to simulate sensor application in deeper well section.

Pressure crosstalk has been reduced in the rigid sensor design, but it remains a problem. The sensor design needs to be improved to minimize the pressure crosstalk effect.

5.2. CASING IMAGER IMPROVEMENT

The radial expansion test setup needs to be improved to be able to generate uniform radial deformation on the pipe to characterize the casing imager performance in radial expansion deformation.

The strain sensor design needs to be improved to reduce the sensor size so that to accommodate more sensors in one helical wrap for casing ovalization measurement.

Since the casing axial strain is found to be smaller than 0.1% in all the finite element simulations, the system accuracy needs to be improved for casing strain measurement below 0.1%.

A full scale laboratory test of the casing imager deployed on a real-size casing is desired to study the system's performance, and a field pilot test is required before the system could be applied in the field.

5.3. PRESSURE SENSOR DEVELOPMENT

The distributed coaxial cable temperature and strain sensors have been developed and characterized for CO_2 sequestration application, with the development of coaxial cable pressure sensor, the system could monitor the wellbore temperature profile, casing deformation, and reservoir pressure simultaneously. The measured reservoir pressure could provide input for the reservoir numerical simulation models for CO_2 saturation and plume movement estimation.

5.4. ANALYTICAL AND NUMERICAL MODELS

The finite element analysis conducted in this research did not consider the pore pressure change during CO_2 injection. Numerical models that consider the pore pressure change caused by CO_2 injection needs to be developed.

The casing imager can be used for hydraulic stimulation fracture volume estimation or reservoir compaction caused surface subsidence calculation if appropriate analytical or numerical model is developed.

A numerical model for wellbore temperature profile caused by CO_2 injection, CO_2 leakage, or hydraulic stimulation operation is desired to use the distributed temperature sensor measurement as input for these applications.

APPENDIX

PUBLICATIONS FROM THIS DISSERTATION

PUBLISHED PAPERS

Li, Y., Cheng, B., Zhu, W., Nygaard, R., & Xiao, H. (2016). Laboratory Evaluation of a Real-Time Coaxial Cable Casing Imager for Wellbore Integrity Monitoring. Unconventional Resources Technology Conference, Aug. 1-3, San Antonio, TX, US.

Li, Y., Zhu, W., Cheng, B., Nygaard, R., & Xiao, H. (2016). Laboratory Evaluation of Distributed Coaxial Cable Temperature Sensor for Application in CO_2 Sequestration Well Characterization. *Greenhouse Gas Sci Technol*. DOI: 10.1002/ghg.

Li, Y., Zhu, W., Nygaard, R., & Xiao, H. (2015). Robust and Cost Effective Distributed Coaxial Cable Sensors Verified as Real-Time Permanent Downhole Monitoring for Groundwater Safety in Geological CO_2 Storage. Carbon Management Technology Conference, Nov. 17-19, Sugarland, TX, US.

PAPERS IN REVIEW

Li, Y., Nygaard, R. (2016). Feasibility of Real-Time Evaluation of the CO_2 Sequestration Wellbore Integrity with the Coaxial Cable Casing Imager. Ready to be submitted.

Li, Y., Cheng, B., Zhu, W., Nygaard, R., & Xiao, H. (2016). Development and Evaluation of the Coaxial Cable Casing Imager-A Cost-Effective Solution to Real-Time Downhole Monitoring for CO_2 Sequestration Wellbore Integrity. Submitted to *Greenhouse Gas Sci Technol*.

BIBLIOGRAPHY

Ahmed, D., Haryanto, E., Soendoro, F. H., Baez, F., Bolanos, N., & Zhou, W. (2014, February). An Innovative Approach to Forecasting Matrix Stimulation Treatment Results: A Case Study. In SPE International Symposium and Exhibition on Formation Damage Control. Society of Petroleum Engineers.

Al-Gamber, S. D., Mehmood, S., Aramco, S., Ahmed, D., Burov, A., Brown, G., ... & Shrake, G. (2013, October). Tangible Values for Running Distributed Temperature Survey as Part of Stimulating Multi-Lateral Injection Wells. InSPE Middle East Intelligent Energy Conference and Exhibition. Society of Petroleum Engineers.

Bacon, D. H. (2013). Reduced-Order Model for the Geochemical Impacts of Carbon Dioxide, Brine and Trace Metal Leakage into an Unconfined, Oxidizing Carbonate Aquifer, Version 2.1 (No. PNNL-22285). Pacific Northwest National Laboratory (PNNL), Richland, WA (US).

Baker Hughes Incorporated. (2010a). SureView real-time fiber-optic compaction monitoring system [Brochure]. Retrieved July 11, 2013 from http://c14503045.r45.cf2.rackcdn.com/v1/6d9595dc1c7754cdc039ba0ad7cd32e5/30643-real-time-fiber-optic-casing-imaging-system_brochure-0910.pdf.

Baker Hughes Incorporated. (2010b). Optical reality: fiber-optic technology monitors sand screen deformation in real time. Connexus, 1(1), 20-23.

Bateman, K., Molenaar, M. M., & Brown, M. D. (2013, November). Lessons Learned from Shell's History of Casing Conveyed Fiber Optic Deployment. InSPE Unconventional Resources Conference Canada. Society of Petroleum Engineers.

Bell, J. S., & Babcock, E. A. (1986). The stress regime of the Western Canadian Basin and implications for hydrocarbon production. *Bulletin of Canadian Petroleum Geology*, 34(3), 364-378.

Benson, S. M., Gasperikova, E., & Hoversten, G. M. (2004, September). Monitoring protocols and life-cycle costs for geologic storage of carbon dioxide. In Proceedings of the 7th International Conference on Greenhouse Gas Control Technologies (GHGT-7) (pp. 1259-1266).

Bois, A. P., Garnier, A., Galdiolo, G., & Laudet, J. B. (2012). Use of a mechanistic model to forecast cement-sheath integrity. *SPE Drilling & Completion*, 27(02), 303-314.

Bois, A. P., Garnier, A., Rodot, F., Sain-Marc, J., & Aimard, N. (2011). How to prevent loss of zonal isolation through a comprehensive analysis of microannulus formation. *SPE Drilling & Completion*, 26(01), 13-31.

Bosma, M., Ravi, K., Van Driel, W., & Schreppers, G. J. (1999, January). Design approach to sealant selection for the life of the well. In SPE Annual Technical Conference and Exhibition. Society of Petroleum Engineers.

Cairns, G., Jakubowicz, H., Lonergan, L., & Muggeridge, A. (2010, January). Issues regarding the use of time-lapse seismic surveys to monitor CO2 sequestration. Society of Exploration Geophysicists.

Carlsen, M., Kofoed, S. S., Rijkels, L., & Marketz, F. (2013, October). Production Optimisation of a Long Horizontal Well Using Permanent Down-hole Distributed Temperature and Pressure Monitoring and Surface Controlled Zones. In SPE Middle East Intelligent Energy Conference and Exhibition. Society of Petroleum Engineers.

Cenovus Energy Inc. (2011). Infrastructure and well integrity assessment of SW 30-5-13w2. Retrieved from http://www.cenovus.com/operations/docs/Cenovus-infrastructure.pdf

Climate-data (2016). Historical weather data: Weyburn. Retrieved from http://en.climate-data.org/location/11916/

Cook, P. (2014). Geologically storing carbon: Learning from the Otway Project experience. CSIRO PUBLISHING.

Costello, C., Sordyl, P., Hughes, C. T., Figueroa, M. R., Balster, E. P., & Brown, G. (2012, January). Permanent distributed temperature sensing (DTS) technology applied in mature fields - a Forties field case study. Society of Petroleum Engineers. doi:10.2118/150197-MS.

Da Silva, M. F., Muradov, K. M., & Davies, D. R. (2012, January). Review, analysis and comparison of intelligent well monitoring systems. In SPE Intelligent Energy International. Society of Petroleum Engineers.

Duguid, A., & Tombari, J. (2007, May). Technologies for measuring well integrity in a CO2 field. In Sixth Annual Conference on Carbon Capture and Sequestration—DOE/NETL, May (pp. 7-10).

Edlmann, K., Bensabat, J., Niemi, A., Haszeldine, R. S., & McDermott, C. I. (2016). Lessons learned from using expert elicitation to identify, assess and rank the potential leakage scenarios at the Heletz pilot CO 2 injection site. *International Journal of Greenhouse Gas Control*, 49, 473-487.

European Commission. (2013, May). State of art report on monitoring technology (Report No. D-No: 2.2.2). Retrieved October 20, 2013 from http://www.modern-fp7.eu/fileadmin/modern/docs/Deliverables/MoDeRn_D2.2.2_State_of_art_report.pdf

Freifeld, B. M. (2009, January). Integrated well-based monitoring for CO2 sequestration. Society of Petroleum Engineers. doi:10.2118/127752-MS.

Freifeld, B. M., Daley, T. M., Hovorka, S. D., Henninges, J., Underschultz, J., & Sharma, S. (2009). Recent advances in well-based monitoring of CO2 sequestration. Energy Procedia, 1(1), 2277-2284.

Gomez, S. (2015). Wellbore *Microannulus Characterization and Seal Repair: Computational and Lab Scale Modeling* (Doctoral dissertation). Retrieved from http://repository.unm.edu/handle/1928/30336

Harvey, O. R., Cantrell, K. J., Qafoku, N. P., & Brown, C. F. (2012). Geochemical Implications of CO2 Leakage Associated with Geologic Storage: A Review. Report prepared for the US Department of Energy under Contract DE-AC05-76RL01830.

Holley, E. H., Jones, T. A., Dodson, J., & Salazar, J. (2014, February). Using distributed optical sensing to constrain fracture models and confirm reservoir coverage in the Permian Basin. In SPE Hydraulic Fracturing Technology Conference. Society of Petroleum Engineers.

Holley, E. H., Zimmer, U., Mayerhofer, M. J., & Samson, E. (2010, January). Integrated analysis combining microseismic mapping and fiber-optic distributed temperature sensing (DTS). In Canadian Unconventional Resources and International Petroleum Conference. Society of Petroleum Engineers.

Hovorka, S. D., Benson, S. M., Doughty, C., Freifeld, B. M., Sakurai, S., Daley, T. M., ... & Knauss, K. G. (2006). Measuring permanence of CO2 storage in saline formations: the Frio experiment. Environmental Geosciences, 13(2), 105-121.

Huang, J., Wang, T., Hua, L., Fan, J., Xiao, H., & Luo, M. (2013). A Coaxial Cable Fabry-Perot Interferometer for Sensing Applications. Sensors, 13(11), 15252-15260.

Huang, J., Wei, T., Lan, X., Fan, J., & Xiao, H. (2012, April). Coaxial cable Bragg grating sensors for large strain measurement with high accuracy. In SPIE Smart Structures and Materials+ Nondestructive Evaluation and Health Monitoring (pp. 83452Z-83452Z). International Society for Optics and Photonics.

Jacobs, T. (2014). Downhole Fiber-Optic Monitoring: An Evolving Technology. SPE Journal of Petroleum Technology, 66(8), 44-53.

James, J. S., & Alex, V. S. (2003). Distributed temperature sensing-A DTS primer for oil and gas production.

Jenkins, C., Chadwick, A., & Hovorka, S. D. (2015). The state of the art in monitoring and verification—ten years on. *International Journal of Greenhouse Gas Control*, 40, 312-349.

Jimenez, J. (2006). *Geomechanical performance assessment of CO2-EOR Geological Storage Project* (Doctoral dissertation, Ph. D. thesis, University of Alberta).

Kaura, J. D., & Sierra, J. (2008, January). Successful Field Application in Continuous DTS Monitoring Under Harsh Environment of SAGD Wells Using Improvised Optical-Fiber Technology: Case Study From Canada. In SPE Annual Technical Conference and Exhibition. Society of Petroleum Engineers.

Koelman, J. V. V., Lopez, J. L., & Potters, H. (2011, January). Fiber optic technology for reservoir surveillance. International Petroleum Technology Conference. doi:10.2523/14629-MS.

Lee, B. (2003). Review of the present status of optical fiber sensors. Optical Fiber Technology, 9(2), 57-79.

Little, M. G., & Jackson, R. B. (2010). Potential impacts of leakage from deep CO2 geosequestration on overlying freshwater aquifers. Environmental science & technology, 44(23), 9225-9232.

Mago, N., Hicks, S., & Simms, W. (2016). Sequentially coupled thermal-stress analysis of a new steel concrete composite slab under fire. *SESOC Journal*, 29(1), 37.

Martens, S., Kempka, T., Liebscher, A., Lüth, S., Möller, F., Myrttinen, A., ... & Kühn, M. (2012). Europe’s longest-operating on-shore CO2 storage site at Ketzin, Germany: a progress report after three years of injection. Environmental Earth Sciences, 67(2), 323-334.

May, F., & Waldmann, S. (2014). Tasks and challenges of geochemical monitoring. Greenhouse Gases: Science and Technology, 4(2), 176-190.

Medina, M., Torres, C. E., Sanchez, J., Boida, L., Leon, A. J., Jones, J. A., & Yicon, C. (2012, January). Real-Time downhole monitoring of electrical submersible pumps rated to 250 degree C using fiber optic sensors: case study and data value in the Leismer SAGD project. Society of Petroleum Engineers. doi:10.2118/153984-MS.

Metz, B. (Ed.). (2005). *Carbon dioxide capture and storage: special report of the intergovernmental panel on climate change*. Cambridge University Press.

Molenaar, M. M., Fidan, E., & Hill, D. J. (2012, March). Real-time downhole monitoring of hydraulic fracturing treatments using fibre optic distributed temperature and acoustic sensing. In SPE/EAGE European Unconventional Resources Conference & Exhibition-From Potential to Production.

Möller, F., Liebscher, A., Martens, S., Schmidt-Hattenberger, C., & Streibel, M. (2014). Injection of CO2 at Ambient Temperature Conditions–Pressure and Temperature Results of the “cold injection” Experiment at the Ketzin Pilot Site. *Energy Procedia*, 63, 6289-6297.

Moreno, F. J., Chalaturnyk, R., & Jimenez, J. (2005). Methodology for assessing integrity of bounding seals (Wells and Caprock) for geological storage of CO_2. In Proceedings of the 7th international conference on greenhouse gas control technologies.

Nabih, A., & Chalaturnyk, R. J. (2014, June). Stochastic Life Cycle Approach to Assess Wellbore Integrity for CO2 Geological Storage. In SPE Heavy Oil Conference-Canada. Society of Petroleum Engineers.

Nordbotten, J. M., Celia, M. A., & Bachu, S. (2004). Analytical solutions for leakage rates through abandoned wells. Water Resources Research, 40(4), W04204.

Nuñez-Lopez, V., Muñoz-Torres, J., & Zeidouni, M. (2014). Temperature monitoring using Distributed Temperature Sensing (DTS) technology. Energy Procedia, 63, 3984-3991.

Nygaard, R., Bai, B., & Eckert, A. (2013, February). Geomechanical simulation of CO2 leakage and cap rock remediation. Rolla, MO: Missouri University of Science and Technology.

Nygaard, R., & Lavoie, R. (2009). *Project cost estimate-Wabamun area CO2 sequestration project (WASP)*. University of Calgary.

Nygaard, R., Salehi, S., Weideman, B., & Lavoie, R. G. (2014, January 1). Effect of Dynamic Loading on Wellbore Leakage for the Wabamun Area CO2-Sequestration Project. Society of Petroleum Engineers. doi:10.2118/146640-PA

Pan, Y., Chen, Z., Xiao, L., Zhang, Y., & Fu, J. (2010, July). Application of fiber Bragg grating sensor networks in oil wells. In Nigeria Annual International Conference and Exhibition.

Pearce, J. M., & West, J. M. (2007). Study of potential impacts of leaks from onshore CO2 storage projects on terrestrial ecosystems. IEA Greenhouse Gas R&D Programme Technical Study, 3.

Pearce, J., Legrand, P., Dominique, T., Childers, B., Rambow, F., & Dria, D. (2009, January). Real-time compaction monitoring with fiber-optic distributed strain sensing (DSS). In SPWLA 50th Annual Logging Symposium. Society of Petrophysicists and Well-Log Analysts.

Pearce, J., Rambow, F., de Jongh, H., Dria, D., Hall, T., Stoesz, C., ... & Dominique, T. (2010, June). Applications And Deployments Of The Real-Time Compaction Monitoring System. In SPWLA 51st Annual Logging Symposium. Society of Petrophysicists and Well-Log Analysts.

Rambow, F. H., Dria, D. E., Childers, B. A., Appel, M., Freeman, J. J., Shuck, M., ... & Dominique, T. (2010). Real-Time Fiber-Optic Casing Imager.SPE Journal, 15(04), 1-089.

Rubin, E. S., Davison J. E., & Herzog, H. J. (2015). The cost of CO2 capture and storage. International Journal of Greenhouse Gas Control. 40, 378-400.

Rusch, D. W., Sabins, F., & Aslakson, J. (2004, January). Microannulus leaks repaired with pressure-activated sealant. In SPE Eastern Regional Meeting. Society of Petroleum Engineers.

Schmidt-Hattenberger, C., Otto, P., Toepfer, M., Borm, G., & Baumann, I. (2004, June). Development of fiber Bragg grating (FBG) permanent sensor technology for borehole applications. In Second European Workshop on Optical Fibre Sensors (pp. 124-127). International Society for Optics and Photonics.

Smith, K. L., Steven, M. D., Jones, D. G., West, J. M., Coombs, P., Green, K. A., ... & Beaubien, S. E. (2013). Environmental impacts of CO 2 leakage: recent results from the ASGARD facility, UK. Energy Procedia, 37, 791-799.

Tardy, P., Chang, F., & Qiu, X. (2011, November). Determining Matrix Treatment Performance From Downhole Pressure And Temperature Distribution: A Model. In International Petroleum Technology Conference.

Tepnarong, P. (2012, January). Bond strength of cement sealing in Maha Sarakham salt. In ISRM Regional Symposium-7th Asian Rock Mechanics Symposium. International Society for Rock Mechanics.

The National Energy Technology Laboratory. (2009). Project solicitation: innovative and advanced technologies and protocol for monitoring/verification/accounting (MVA), simulation, and risk assessment of carbon dioxide (CO2) sequestration in geologic formations. United States Department of Energy.

The National Energy Technology Laboratory. (2012). Project solicitation: national energy technology laboratory, technologies to ensure permanent geologic carbon storage. United States Department of Energy.

Thermocoax Incorporated (2012). Mineral insulated signal transmission cable [Internet]. Available from http://www.thermocoax-nuclear.com/nuclear---transmission-cable-application.html

Thodi, P., Paulin, M., Forster, L., Burke, J., & Lanan, G. (2014, February). Arctic Pipeline Leak Detection using Fiber Optic Cable Distributed Sensing Systems. In OTC Arctic Technology Conference. Offshore Technology Conference.

United States Environmental Protection Agency. (2010, November). Geologic CO2 sequestration technology and cost analysis (Report No. 816-B-08-009). Retrieved from http://water.epa.gov/type/groundwater/uic/class6/upload/geologicco2sequestrationtechnologyandcostanalysisnov2010.pdf

Watson, T. L., & Bachu, S. (2007, January). Evaluation of the potential for gas and CO2 leakage along wellbores. In E&P Environmental and Safety Conference. Society of Petroleum Engineers.

Wei, T., Wu, S., Huang, J., Xiao, H., & Fan, J. (2011). Coaxial cable Bragg grating. Applied Physics Letters, 99(11), 113517-113517.

Weideman, B. L. (2014). *Investigation of cased wellbore integrity in the Wabamun area sequestration project* (Master's Thesis). Retrieved from http://scholarsmine.mst.edu/masters_theses/7284/

Weideman, B., & Nygaard, R. (2014). How cement operations affect your cement sheath short and long term integrity. In American Association of Drilling Engineers Fluids Technical Conference and Exhibition.

Williams, G. R., Brown, G., Hawthorne, W., Hartog, A. H., & Waite, P. C. (2000, December). Distributed temperature sensing (DTS) to characterize the performance of producing oil wells. In Environmental and Industrial Sensing (pp. 39-54). International Society for Optics and Photonics.

Yang, C., Hovorka, S. D., Young, M. H., & Trevino, R. (2014). Geochemical sensitivity to CO2 leakage: detection in potable aquifers at carbon sequestration sites. *Greenhouse Gases: Science and Technology*, 4(3), 384-399.

Zimmer, M., Pilz, P., & Erzinger, J. (2011). Long-term surface carbon dioxide flux monitoring at the Ketzin carbon dioxide storage test site. Environmental Geosciences, 18(2), 119-130.

VITA

Yurong Li was born in 1990 in Qingdao, China. She entered China University of Petroleum (Huadong) in 2008 and completed her Bachelor's degree in Petroleum Engineering in July, 2012 with Outstanding Graduate Award. After finishing her Bachelor's education, she was admitted to the Petroleum Engineering Master's program in Missouri University of Science and Technology in 2012, and she completed the Master's program in May, 2014. She then continued her education to receive her Ph.D. degree in Petroleum Engineering from Missouri University of Science and Technology in December, 2016.

She was actively involved in academic, social, and professional activities in both undergraduate and graduate school. She volunteered as the English Teaching Assistant at Tone Education Inc., a local language institute in Qingdao, China in 2009 and 2010. She co-founded the Students' Communication Association and served as the Vice President in 2012. She participated in the Schlumberger Ocean Academic Competition in North America in 2015, and her team won the First Prize out of the 26 participating teams. She worked as a Graduate Research Assistant on a US Department of Energy Project under Award Number DE-FE0009843. And she is affiliated with multiple professional organizations, including Society of Petroleum Engineers, American Association of Drilling Engineers, Toastmasters International Inc., etc.

She has published and presented work on development, evaluation, and application of distributed coaxial cable sensing system for CO_2 sequestration wellbore integrity monitoring and wellbore stability numerical simulation.